TÉCNICO LISBOA

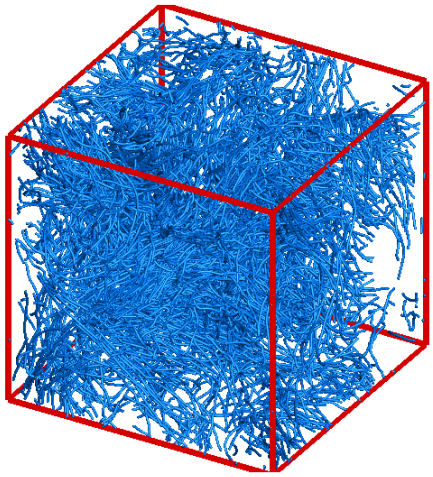

Lagrangian Statistics in Homogeneous Isotropic Turbulence: Newtonian and Hyper-Viscous Fluids

Manuel Araújo Barjona Henriques

Thesis to obtain the Master of Science Degree in

Aerospace Engineering

Supervisor: Prof. Carlos Frederico Neves Bettencourt da Silva

Examination Committee

Chairperson: Prof. Filipe Szolnoky Ramos Pinto Cunha
Supervisor: Prof. Carlos Frederico Neves Bettencourt da Silva
Member of the Committee: Dr. Duarte Manuel Salvador Freire Silva de Albuquerque

October 2016

Agradecimentos

Várias pessoas contribuíram, de forma directa ou indirecta, para que este trabalho chegasse a bom termo. A todas elas, deixo registado o meu sincero agradecimento.

Não sendo possível nomeá-las a todas, algumas há a quem não posso deixar de expressar o meu apreço e reconhecimento.

Ao coordenador da Tese de Mestrado, Carlos Bettencourt da Silva, pela orientação e total disponibilidade e pelo saber, experiência, incentivo e paciência com que me guiou no desenvolvimento deste trabalho.

Ao LASEF, pelos recursos que me disponibilizaram para eu poder realizar o trabalho.

Ao Laboratório de Computação Avançada da Universidade de Coimbra por me facultarem acesso ao cluster Milipeia, onde foram executadas as simulações presentes nesta tese.

Às Professoras Paula Campos e Ana Costa, pelo importante contributo no meu crescimento académico.

Aos meus amigos César, Rafaela, Rita, Telmo, João, Tomás, Ricardo e Diogo, pelo companheirismo e amizade, e em particular ao Tiago por toda a ajuda disponibilizada.

Aos meus Tios Nuno e Sofia por toda a amizade e disponibilidade.

À minha Tia Any, por me ter incutido o interesse pela matemática.

Aos meus Avós e Tios Vasco e Tininha (in memoriam) pelo acolhimento, apoio e afecto que sempre me dedicaram.

À Ana Rita, um agradecimento especial por estar sempre presente e me apoiar em todos os momentos.

Aos meus Irmãos Gonçalo e Vasco, pela amizade, apoio e presença.

Aos meus Pais por terem tornado isto possível e pelo grande contributo que tiveram na minha formação pessoal.

A Todos, Obrigado.

Resumo

A presente tese é dedicada ao estudo fundamental de turbulência numa perspectiva Lagrangiana, que é uma abordagem natural ao estudo do transporte de escalares em escoamentos turbulentos em diferentes contextos como formação de nuvens, combustão turbulenta ou até dispersão de poluentes [1, 2, 3, 4].

Nesse sentido é implementado um código de DNS, com uso de métodos espectrais e capaz de fazer o seguimento de partículas. O código é implementado para funcionar em computação paralela, este é altamente escalável devido ao uso de uma política de minimazação de comunicações.

Pela primeira vez, é avaliado o efeito da hyper-viscosidade em estatísticas Lagrangianas. Mostra-se que estas são somente afectadas nas escalas dissipativas. Por isso, conclui-se que a hyper-viscosidade pode ser usada no cálculo de estatísticas da zona inercial, permitindo que esse cálculo seja feito para números de Reynolds 150% maiores do que os observados actualmente.

Usando o modelo de Hyper-viscosidade conseguiu-se realizar duas simulações com os números de Reynolds mais altos de sempre. As estatísticas dessas simulações apresentam, pela primeira vez em 75 anos, evidências que corroboram a existência de uma correlação linear com o tempo da LVSF-2. Com estes resultados prevê-se que a constante universal dessa relação seja $C_0 = 6.7$.

É feita uma análise às estatísticas de dispersão usando a definição matemática de variância de uma variável estatística. É observado que os resultados para elevados Reynolds são absolutamente consistentes com o previsto pela terceira Lei de dispersão de Richardson. A constante universal de Richardson é também medida pela primeira vez, obtendo-se que $g = 0.165$.

Palavras-Chave: Turbulência Isotrópica, Hyper-viscosidade, Computação de alto desempenho, Estatísticas de Lagrange, Funções de estrutura de Lagrange, Disperção de partículas.

Abstract

The present thesis work, is dedicated to the fundamental study of turbulence in a Lagrangian frame which is a natural approach to understand the turbulent transport in contexts as industrial mixing, cloud formation, turbulent combustion or even pollutant dispersion [1, 2, 3, 4].

For this purpose a numerical code for DNS with pseudo-spectral schemes with particle tracking in a parallel architecture is develop. Using as policy the minimization of synchronous communications, results a highly scalable.

For the first time, the effect of Hyper-viscosity in Lagrangian statistics is evaluated and it is shown that the Hyper-viscosity model can be used to study Lagrangian statistics, except for dissipative time lags. Also is shown that using Hyper-viscosity can decrease the computational effort, such as memory usage, up to 1000 times. Also the use of Hyper-viscosity will allow an increase of the maximum achievable Reynolds number in 150% (comparing with the highest at the present time).

With Hyper-viscosity two simulations with the highest Reynolds numbers ever achieved are carried out. With these results, for the first time in 75 years, it is presented clear evidence that corroborate the existence a linear scaling law for the LVSF-2. Also it is predicted that the universal constant of that relation is $C_0 = 6.7$.

The results of relative dispersion using the exact mathematical definition of the second order moment of a PDF shows, for the first time in 90 years, excellent agreement with the Richardson T3 law. The Richardson universal constant is measured and has the value $g = 0.165$.

Keywords: Isotropic turbulence, Hyper-viscosity, High-performance computing, Lagrangian structure functions, Particle dispersion.

Contents

List of Tables

List of Figures

Nomenclature

Acronyms

DNS	Direct Numerical Simulation
FFT	Fast Fourier Transform
LES	Large Eddy Simulation
LVSF-n	Lagrangian Velocity Structure Function of order n
HIT	Homogeneous Isotropic Turbulence
PDF	Probability Density Function
RANS	Reynolds-Averaged Navier-Stokes
TS13	Taylor-Series 13-point scheme

Greek symbols

ν	Kinematic viscosity
μ	Dynamic viscosity
η	Kolmogorov scale
λ	Taylor scale
ϵ	Dissipation
τ	Time lag
τ_η	Kolmogorov time scale
τ_{ij}	Stress tensor
ρ	Volumetric mass
$\rho(\tau)$	Lagrangian correlation function
ψ	General function
$\hat{\psi}$	Fourier transform of a general function
δ_{ij}	Kronecker delta
$\vec{\Omega}$	Vorticity vector
ξ_n	Eulerian scaling coefficient of the inertial range
ζ_n	Lagrangian scaling coefficient of the inertial range

Roman Symbols

$D_L^n(\tau)$	Lagrangian Velocity Structure Function of order n
$E(k)$	Energy spectra
K	Kinematic energy
k	Wave-number
k_f	Forcing wave-number peak
L	Characteristic flow dimension
$L_{x,y,z}$	Dimension of the domain in x, y and z

l_0	Characteristic dimension of the larger eddies
N	Number of grid points in each direction
p	Pressure
Re	Reynolds number based on the characteristic dimensions
Re_0	Reynolds number based on the larger eddies characteristic dimensions
Re_λ	Reynolds number based on the Taylor scale
S_{ij}	Strain rate tensor
T_L	Lagrangian integral time
U	Characteristic flow velocity
u	Instantaneous velocity
$\overline{u}$	Mean velocity
u'	Instantaneous velocity fluctuation
u_0	Characteristic velocity of the larger eddies

Chapter 1

General Introduction

1.1 Motivation

Fluid flows are present in environmental phenomena, chemical reactions and processes essential to life, thus, fluid mechanics is a fundamental matter to the study of natural sciences such as physics, chemistry and biology.

There are two types of flows, **Laminar flows** which are characterize by smooth fluid motions and where the disturbances are damped by the action of viscosity and **Turbulent flows** where the fluid velocity field varies significantly and irregularly in both position and time [5].

Almost every flow observed in nature and of engineering interest is turbulent. Turbulence strongly increases the rates of the transport and mixing of matter, momentum, and heat in a flow (in comparison with laminar flow) [5] and is crucial in engineering applications, therefore, turbulence is a subject of great interest, synthesized by Nobel-prize-winner Richard Feynman who stated: *"turbulence is the most important unsolved problem of classical physics."*

Regarding aerospace engineering, the study of turbulent flows in a Lagrangian point of view it's fundamental for matters such as, turbulent combustion and pollutant dispersion.

1.2 Turbulence - Historical overview and Fundamental ideas

The first dated recognition of turbulence as a distinct fluid behaviour was at least 500 years ago by Leonardo da Vinci. However, only in 1883 it was discovered, by Osborne Reynolds [6], that the adimensional coefficient of $\frac{UL}{\nu}$ (where U and L are the flow characteristic velocity and length scales and ν is the kinematic viscosity of the fluid), has a major role in transition from laminar to turbulent flow. Due to the importance of this discover, the latter coefficient was named after him as Reynolds number, which physically represents the ratio of characteristic values of inertial forces and viscous forces.

Beside from that Osborne Reynolds made also another big contribution in the study of turbulence in 1894, when he suggested that, when analysing a turbulent flow, the velocity field should be decomposed into the time-averaged component ($\overline{u}$) and the fluctuating component (u'). This decomposition is relevant

because, even though the velocity field $u(x,t)$ is a random function if, for a certain flow, one measures, over a significant period of time, $u(x,t)$ and then calculates the time-average, for the first, second and n-th time, the results will be identical. In the same work he deduced the Reynolds-averaged Navier–Stokes equations (RANS), a tool to compute the mean velocity field in a turbulent flow [7].

The time-averaged velocity ($\overline{u}$) of a flow measured over a large period of time is time independent, this result also holds for $\overline{u^2}$ or $\overline{u^n}$, when n is a natural number. Thus, one can conclude that the statistical properties of a turbulent flow are uniquely determined by the boundary conditions and the initial conditions [8].

Therefore, turbulence is statistically stable, i.e., although the velocity is complex and unpredictable its statistics are not. Hence, the theory of turbulence must be statistical, since an individual description of the velocity fields is in principle impossible [5].

Later, in 1922, Lewis Fry Richardson wrote a verse that summarizes turbulence behaviour [9]:

"Big whirls have little whirls that feed on their velocity,
and little whirls have lesser whirls and so on to viscosity."

This verse beside of alluding to the existence of coherent structures, eddies, and the ample range of (length, time and velocity) scales characteristic of turbulent flows, also suggest the existence of an energy "cascade", which is represented in figure 1.1, where the flow energy is largely concentrated on large length scales eddies, that, due to inertial instabilities break-up into small vortices passing energy into smaller structures, consequently this smaller vortices are also unstable and break-up into even smaller vortices and so on, until the eddies size becomes so small that viscous forces become of the order of the inertial forces and dissipate mechanical energy by converting it into internal energy [8].

It is important to emphasize that the whole process is mainly driven by inertial forces and the figure 1.1, is not a representation of real turbulent flow, because, in a real flow, small eddies are embodied in large ones [10].

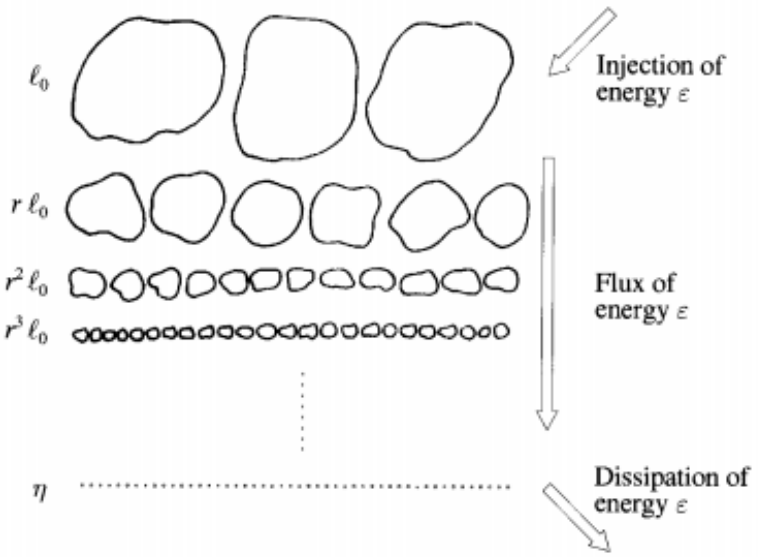

Figure 1.1: Sketch of the energy cascade, Source: [10].

Also, it is really interesting to notice that in a situation where turbulence is in equilibrium the transferred energy from the larger scales is dissipated by the small scales, which means that the rate of viscous dissipation is independent of the kinematic viscosity. Thus, the larger eddies impose the dissipation rate and any changes in the kinematic viscosity only effect the small eddies size. For example, a decrease in kinematic viscosity will make the small eddies smaller so that the velocity gradients are more intense and thus the dissipation rate will remain constant.

In the year of 1935 Geoffrey Ingram Taylor wrote that *" ... there is a strong tendency to isotropy in turbulent motion..."* [11]. However, his hypothesis of turbulence isotropy is merely valid for a few cases and in the majority of the flows with practical relevance it is merely a far approximation from reality [12].

Taken into account these ideas, Andrey Kolmogorov, proposed three fundamental hypothesis regarding the physical nature of turbulence [12]:

- **Local isotropy of the small scales**: At sufficiently high Reynolds numbers, for a small domain far away from the boundaries and singularities, the motions are statistically isotropic.

  Note: One can conclude whether if a domain is small or not by comparing its linear dimensions with the characteristic length of the flow (L).

- **First similarity hypothesis**: At sufficiently high Reynolds numbers, for locally isotropic turbulence, the statistics of motion have a universal form that is only function of the kinematic viscosity, ν , and the dissipation rate, ϵ.

- **Second similarity hypothesis**: At sufficiently high Reynolds numbers, for locally isotropic turbulence the statistics of motion for scales larger than the scales where dissipation forces dominate, have a universal form that is only function of the mean dissipation rate, $\bar{\epsilon}$.

  The range of scales that this hypothesis concern is named the **Inertial sub-range**

In this hypothesis it was specified that there are different ranges of scales with specific characteristics in a turbulent flow. According to [1], there are three regions: The *Energy-containing range*, the *Inertial-subrange* and the *Dissipation range*.

Three different ranges are defined, with 4 distinct scales:

- Characteristic scale: Regarding the domain geometry (L).

- Length scale of the largest eddies: Regarding the larger eddies in the flow (l_0).

- Taylor Microscale: A scale within the inertial subrange (λ). Even though this scale is important in the characterization of a turbulent flow, it does not have a clear physical interpretation [1].

- Kolmogorov scale: the dissipative scale (η).

To finalize this section some relations regarding these distinct scales are given.

Using the first similarity hypothesis it is straightforward to show that η can only be function of ν and ϵ, using dimensional analysis:

$$\eta = (\frac{\nu^3}{\epsilon})^{\frac{1}{4}}. \tag{1.1}$$

The Taylor microscale, is defined with the use of the second derivative at the origin of the correlation function between two points. It can be also computed using the following formula:

$$\lambda = \sqrt{15 \cdot \frac{\nu}{\epsilon} \cdot \overline{u'^2}}. \tag{1.2}$$

It is well known that the kinetic energy of the larger eddies is proportional to their squared velocity ($\sim u_0^2$), also the fragmentation time, by dimensional analysis, must be $\tau_0 \sim \frac{l_0}{u_0}$. Thus, the rate of energy transferred is $T_0 \sim \frac{u_0^3}{l_0}$. As stated before in a turbulent flow in equilibrium the dissipation rate is equal to the rate of energy transferred from the larger eddies, which implies that: $\epsilon \sim \frac{u_0^3}{l_0}$. Knowing this, it is possible to relate l_0 and η: (Re_0 is the Reynolds number of the larger eddies.)

$$\frac{\eta}{l_0} \sim Re_0^{-3/4}. \tag{1.3}$$

1.3 Eulerian and Lagrangian view

There are two different perspectives to analyse a flow. One is the Eulerian view in which the evaluation of the flow properties in a certain moment is made using all the flow points, at fixed locations, and the another one, the Lagrangian view, in which the flow properties are evaluated over time in a reference frame that follows the motion of infinitesimal fluid elements [13].

The study of turbulence using a Lagrangian view was used by Taylor [14] and Richardson [9] in 1922, however, in the past seventy years the majority of research in turbulence is made considering an Eulerian view due to practical reasons since in experimental works it is easier to evaluate the velocity or a scalar quantity at fixed points. The same happens in numerical simulations where the calculations are performed in a fixed grid.

Recently a growing interest has been attracted to the Lagrangian view due to some facts:

- It is a natural approach to study turbulent transport, which is of extreme importance in the development of stochastic models used for contexts as industrial mixing, cloud formation, turbulent combustion or even pollutant dispersion [1, 2, 3, 4].
- It is now possible to experimentally perform high precision particle tracking in turbulent flows [15] [16].
- Multi-particle statistics are an important tool to understand the evolution in time of the shape of structures within the turbulent flow and thus a better understanding of the physical mechanisms present in the energy cascade [4] [17].

However, unlike the Eulerian statistics, for the Lagrangian ones it is not yet confirmed the existence of an exact relation, equivalent to the four fifths law [18] (Eulerian statistics exact rule under some assumptions). The allegedly universal law, for Lagrangian statistics, states that the second order moments of

Lagrangian velocity increments scale linearly with time. The demonstration or refutation of this relation is thus of extreme importance such for stochastic modelling and also in a fundamental level. The reason why it is so important in a fundamental level is because *"... this relation is intimately connected with the picture of the Richardson cascade, built in terms of a superposition of eddies at different scales and with different characteristic times (eddy turn over times)."* [19].

1.4 Numerical simulations

The equations that describe the motion of a Newtonian fluid flow (either laminar or turbulent) are the Navier-Stokes equations. This set of equations are derived considering the conservation of mass and momentum and using the assumption that the locally stress tensor is proportional to the strain rate tensor (Newtonian fluid). However this set of equations is non-linear with co-dependent variables, therefore extremely difficult to solve, so difficult that is not yet been proven the existence of a unique smooth solution. The demonstration of existence and uniqueness is so relevant that the Clay Mathematics Institute has called it one of the seven most important open problems in mathematics and offers 1,000,000 American dollar prize for a solution or a counter-example.

Even though, it is possible for few, oversimplified, cases to compute an exact solution, in practical terms the study of realistic events can only be made using either experimental or numerical simulations. In contrast with numerical simulations, the experimental via can be very expensive and also the measurement of some properties can be difficult or even impossible. Adding this to the growing computer power and its facility of measuring flow properties, results that numerical simulations are now an essential tool for engineering applications and fundamental research.

There are three main approaches for numerical simulations of turbulent flows: solving the Reynolds-Averaged Navier-Stokes (RANS), Direct Numerical Simulation (DNS) and Large-Eddy Simulation (LES). The main inherent principles, upsides and downsides of each approach are now summarized:

- **RANS:** Consists in solving the mean averaged Navier-Stokes equations. However, this set of equations are not mathematically closed due to the existence of terms regarding the fluctuating components. To overcome this problem a mathematical model that correlates the unknowns terms with time-averaged components is required. In the specific case of incompressible Newtonian fluid, the most common approach is the use of the Boussinesq hypothesis, according to this the term regarding the fluctuating components is assumed to be linear with the velocity gradients and consequently, it can be seen as a modified kinematic viscosity.

  The great advantage of this method is that it is possible to compute flows over complex geometries at high Reynolds numbers.

  A disadvantage is the fact that the unsteadiness nature of turbulence is not modelled due to the use of mean-averaged quantities. Also, the constants used in these models are valid only for a specific set of conditions, thus, a simple change in the boundary conditions makes the results unreliable. Due to this two facts is obvious that this approach is not a tool for fundamental research

in turbulence.

- **DNS:** Consists in solving directly the Navier–Stokes equations resolving all the scales of motion.

  It has the advantage of computing with high precision the quantities involved in the flow such as velocity or scalar fields. This approach is an extremely important tool for investigation purposes because it allows the study of physical processes. Due to this fact this approach is used in the development of mathematical models that try to represent turbulent flows.

  As a disadvantage, it requires a grid space of the order of Kolmogorov's length scale, η, otherwise, the flow energy is not dissipated and the solution diverges. This is a disadvantage because the number of grid points, N, must be of the order of $\sim (\frac{l_0}{\eta})^3$, recalling equation (1.3) results in $N \sim Re_0^{9/4}$, which means that DNS, with the current computing power, is not capable of computing high Reynolds number flows.

- **LES:** In this approach the large scales motions are computed and the small scales motions are modelled. However, since the small scales of motion are modelled, all information regarding small scale effect, for example small scale mixing, is not available.

  With LES it is possible to compute flows with higher Reynolds numbers than DNS. Also, is more reliable than RANS for flows with large scale unsteadiness [1]. In terms of computational cost and precision measurement, this approach is between RANS and DNS.

1.5 Objectives

The goals of this thesis work are:

- Develop a numerical code for DNS, based on pseudo-spectral schemes, with particle tracking in a parallel architecture that is scalable.

  Since particles roam across all the domain, fully parallelization of the code is very hard, besides, during a simulation all the processors have to write in the same file the position and velocity of each particle thus, the scalability can be difficult to achieve.

- Develop a Post-processing code to handle the output data originated by the DNS code, to compute Lagrangian statistics.

- Analyse the effect of hyper-viscosity in the Lagrangian statistics such as the second order structure function and the relative dispersion in particle pairs.

  This is the main originality of this thesis, and it is predicted that this new approach will not have any influence in the inertial sub-range since, the only difference from Newtonian simulations is the way energy is dissipated and not the physical mechanisms responsible for the energy transfer in the inertial range (see section 1.2 to read about the different regions of scale).

- Based on the results from both Newtonian and Hyper-viscous simulations, try to contribute into the resolution of four open problems of extreme importance:

- Is the T3 Richardson law for particle dispersion valid? (1926)
- If so, what is the universal constant in the relation.
- Does the second order Lagrangian structure function scales linearly with time? (1941)
- If so, what is the universal constant in the relation.

1.6 Thesis Outline

This thesis is organized in six chapters:

- **General Introduction**
- **Background**: It will be devoted to the most relevant progress in the analysis of Lagrangian statistics. It will also explain what is an hyper-viscous flow simulation, and why will it be used in the study of Lagrangian statistics.
- **Numerical Methods and Code Implementation**: The governing equations of fluid motion and the numerical methods applied in the code implementation will be presented. In addition, some crucial aspects of the code implementation will be outlined.
- **Verification and Validation**: A required step to ensure that the implementation of the code was correctly made and that the results are meaningful.
- **Results**: In this chapter the results of the simulations, such as the second order moment structure function and the dispersion of particle pairs for different initial distances will be presented.
- **Conclusions**: Conclusions and proposals for future work will be presented presented.

Chapter 2

Background

2.1 The Kolmogorov-Obukhov turbulence theory

Section 1.2 briefly explained the fundamental Kolmogorov hypothesis, however, no direct results where deduced from it. Therefore, in this section, the Kolmogorov theory (K41) will be explained in more detail.

First, remember that the theory of turbulence must be statistic [5], therefore, the variables of interest must be defined. A simple choice could be the velocity at a given point, however this choice is not interesting because, using this variable it is impossible to understand how the different length scales are correlated and therefore the complete description of the flow field would be impossible. Also, the probability density function of the velocity at a point, in homogeneous isotropic turbulence, is independent of the time instant and position, meaning that it does not depend on any other flow parameter. It is clear that if the study of a function that does not depend on any parameter and it cannot be used to understand the turbulence physical mechanisms it is not useful.

Since the study of turbulence, as previously explained, was preferentially carried out in an Eulerian frame, the obvious choice for the variable of interest is the velocity variation in space, i.e.:

$$\delta\vec{u}(\vec{x},\vec{r},t) = \vec{u}(\vec{x}+\vec{r},t) - \vec{u}(\vec{x},t). \tag{2.1}$$

Due to isotropy, only two components of $\delta\vec{u}(\vec{x},\vec{r},t)$ can have different PDFs, the longitudinal velocity variation, $\delta u_{\parallel}(\vec{x},\vec{r},t) = (\vec{u}(\vec{x}+\vec{r},t)-\vec{u}(\vec{x},t))\cdot(\frac{\vec{r}}{|\vec{r}|})$, and the normal component, $\delta u_{\perp}(\vec{x},\vec{r},t) = |\delta\vec{u}(\vec{x},\vec{r},t)-\delta u_{\parallel}(\vec{x},\vec{r},t)(\frac{\vec{r}}{|\vec{r}|})|$.

Since the statistics in statistically stationary turbulence are time independent, the probability density functions of both variables must be also time independent. Due to local isotropy of the small scales (first Kolmogorov hypothesis), the probability density functions cannot depend on the direction of $\vec{r}$ and must only depend on the distance $|\vec{r}|$. Also, in the presence of homogeneity, the statistics must be independent of the position $\vec{x}$. Finally, using the first similarity hypothesis, one conclude that the PDFs will only depend on the distance between two points $|\vec{r}|$, the kinematic viscosity ν and on the mean

dissipation rate $\bar{\epsilon}$. The dissipation rate is given by:

$$\epsilon = 2\nu S_{ij} S_{ij}, \tag{2.2}$$

where S_{ij} is the strain rate tensor $S_{ij} = \frac{1}{2}(\frac{\partial u_i}{\partial x_j} + \frac{\partial u_j}{\partial x_i})$.

For inertial sub-range scales, the PDFs will only depend on $|\vec{r}|$ and ϵ (second similarity hypothesis) thus, the moment of order n, of the longitudinal velocity variation PDF, can be written as:

$$\overline{(\delta u_{\parallel}(\vec{r}))^n} = C_n \ \bar{\epsilon}^{\tau_n} \ |r|^{\zeta_n}, \tag{2.3}$$

and the normal velocity variation PDF as:

$$\overline{(\delta u_{\perp}(\vec{r}))^n} = B_n \ \bar{\epsilon}^{\tau_n} \ |r|^{\zeta_n}, \tag{2.4}$$

where C_n and B_n, according to the K41 theory, are universal constants. Through dimensional analysis it is possible to conclude that $\zeta_n = \tau_n = \frac{n}{3}$. Also, since the PDF of $\delta u_{\perp}$ is symmetric, $B_n = 0$ for odd n.

An exact result deduced in [18], that corroborates this theory, is the four-fifths law which states that:

$$\overline{(\delta u_{\parallel}(\vec{r}))^3} = -\frac{4}{5} \ \bar{\epsilon} \ |r|. \tag{2.5}$$

Note that this equation is a special case of equation (2.3) for n=3, with $C_3 = -\frac{4}{5}$.

To deduce equation (2.5), A. Kolmogorov used the Kármán-Howarth relation, an exact relation that can be deduced from the Navier-Stokes equations [20]. This is one of the most important results in fully develop turbulence because it is an exact relation that must be always verified unless the underlying hypothesis are violated.

Using the same arguments as the ones used to deduce equation (2.3), i.e., dimensional analysis and the Kolmogorov second similarity hypothesis, it is possible to deduce a relation regarding the inertial range of the energy spectra ($E(k)$) as function of the wavenumber (k), which is supported by experimental data, given by (this result will be used for validation purposes):

$$E(k) = C_0 \bar{\epsilon}^{\frac{2}{3}} k^{-\frac{5}{3}}, \tag{2.6}$$

where C_0 is the Kolmogorov constant.

Even though, this result and the relation (2.5) are experimentally corroborated, the scaling coefficients predicted for $n > 3$ present considerable discrepancies when comparing to experimental data. These discrepancies result from the fact that the dissipation is intermittent, which means that the mean dissipation in a sub-domain of the flow is not equal in all sub-domains, i.e., the dissipation rate is also a statistical variable. To better explain this situation, suppose we have a turbulent flow in which all Kolmogorov hypothesis hold, dividing the entire domain into N sub-domains with the same dimensions, it is still possible to apply the K41 theory for each sub-domain, i.e., assume the validity of equation (2.3).

Then, for each sub-domain one can write (the superscript i refers to the i-th sub-domain of the total N):

$$\overline{(\delta u_{\parallel}^{i}(\vec{r}))^{n}} = C_n \, (\bar{\epsilon}^{i})^{\frac{n}{3}} \, |r|^{\frac{n}{3}}. \tag{2.7}$$

On the other hand for the entire domain, one can write (the superscript 'total' refers to the entire domain):

$$\overline{(\delta u_{\parallel}^{total}(\vec{r}))^{n}} = C_n \, (\bar{\epsilon}^{total})^{\frac{n}{3}} \, |r|^{\frac{n}{3}}. \tag{2.8}$$

A mean value of a property ψ regarding the entire domain can be computed, by knowing the mean values of each sub-domain, using the expression $\bar{\psi}^{total} = \frac{1}{N} \sum_{i=1}^{N} \bar{\psi}^{i}$, therefore, $\overline{(\delta u_{\parallel}^{total})^{n}}$ can be computed as:

$$\overline{(\delta u_{\parallel}^{total}(\vec{r}))^{n}} = \frac{1}{N} \sum_{i=1}^{N} \overline{(\delta (u_{\parallel}^{i}(\vec{r}))^{n}}. \tag{2.9}$$

Using the same argument the mean dissipation of the entire domain is given by: $\bar{\epsilon}^{total} = \frac{1}{N} \sum_{i=1}^{N} \bar{\epsilon}^{i}$, substituting this in equation (2.8), and comparing the result with (2.9) (where the right side of the equations is substituted by equation (2.7)), results that:

$$C_n \, |r|^{\frac{n}{3}} \, (\frac{1}{N} \sum_{i=1}^{N} \bar{\epsilon}^{i})^{\frac{n}{3}} = C_n \, |r|^{\frac{n}{3}} \frac{1}{N} \sum_{i=1}^{N} (\bar{\epsilon}^{i})^{\frac{n}{3}}. \tag{2.10}$$

If C_n is universal, then for a given $|r|$, one would conclude that $(\frac{1}{N} \sum_{i=1}^{N} \bar{\epsilon}^{i})^{\frac{n}{3}} = \frac{1}{N} \sum_{i=1}^{N} (\bar{\epsilon}^{i})^{\frac{n}{3}}$, this is only correct if for any n the dissipation is equal in every sub-domain, which as stated before is not true. Therefore, only for n=3 C_n can be universal, which is proven to be an exact result.

Twenty years after publishing this theory, Kolmogorov and Obukhov, refined it using corrections that take into account the random nature of ϵ. It was assumed that equations (2.3) and (2.4) are still valid, however, the constants C_n and B_n are not universal, except for n=3, and depend on the macroestructures of the flow [21]. Hence, a scaling behaviour is still observable, i.e., $\overline{(\delta u)^{n}} \sim r^{\zeta_n}$ and $\overline{\epsilon^{n}} \sim r^{\tau_n}$ however, ζ_n and τ_n are related by: $\zeta_n = \frac{n}{3} + \tau_{\frac{n}{3}}$, where the term $\tau_{\frac{n}{3}}$ is an intermmitency correction.

The intermittency of a signal is a property that is characterized by activity that occurs only during a fraction of the total time. This is observed in the velocity differences between two points at a distance $|r|$, therefore, the similarity hypothesis, which is the base of the K41 theory, cannot be applied.

To try to predict the universal coefficients ζ_p, many models have been proposed, the most used ones are the β-model [22], the multifractal model based on the velocity increments [23] and also the multifractal model based on dissipation structures [24].

Note that, the scaling laws are only valid for flows with high Reynolds numbers based on the Taylor micro-scale Re_{λ}. For now on, in this work, when no other information is given, Reynolds number of the flow is supposed to be interpreted as Re_{λ}. Unfortunately the higher the Reynolds number, the higher the computationally cost, and as a consequence, the study of turbulence, using DNS, is limited to Reynolds numbers of approximately 10^3.

However, it is still possible to measure experimentally the coefficients ζ_n using an important property of turbulence, the extended self-similarity [25]. This property holds for high and low Reynolds numbers and basically states that one can write the n-th moment of the velocity as $\overline{|\delta u(\vec{r})|^n} = A_n \overline{|\delta u(\vec{r})|^3}^{\zeta_n}$. This relation is very important because it allows the measurement of ζ_n for low Reynolds numbers.

2.2 Homogeneous Isotropic Turbulence

The specific case that will be studied in this thesis work is the Homogeneous Isotropic Turbulence (HIT). The principal characteristic of HIT is that the statistics regarding the random motions of the fluid are independent of the position. This flow is idealized and rigorously it does not exist in nature because there is always some space dependence of the statistics. This dependence can be reduced using grid generated turbulence, which is the type of turbulence more close to the idealized HIT, and the one used in experimental investigation [26].

The reason to study HIT is because it is the simplest type of turbulence that can be studied and, if one desires to completely understand any kind of turbulent flow, even the more complex with strong non-homogeneity and high anisotropic fluctuations, first one must understand the simplest case.

Finally, if the scaling laws, described in the previous section, and the physical mechanisms of turbulence are universal, then, they can be studied in this idealized flow.

To give an idea of what type of flow is this one, an example is presented in figure 2.1. The figure was obtained by plotting the trajectories of 200 particles in a HIT simulation carried out in this work. The domain is a cube with linear dimension equal to 2π, with edges represented in figure 2.1 as red lines. Observing figure 2.1 it is undeniable the existence the chaotic nature of the flow.

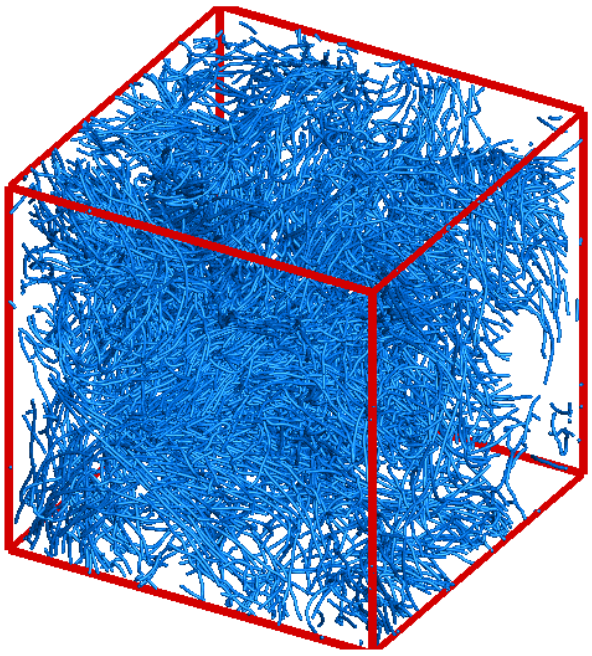

Figure 2.1: Trajectories of 200 particles in an HIT simulation carried out in this work.

2.3 Hyper-viscosity

As explained before, the inertial range is characterized by energy transfer flux from larger scales to smaller scales, where it is dissipated. The intermediate scales, where the energy is transfer only by means of inertial forces is called inertial-range region. The understanding of the physical mechanisms in this range is of extreme importance because it is believed that the scaling laws, regarding this region, are universal (as discussed in section 2.1). Therefore, it is natural to suppose that the way energy is extracted from the the flow does not influence the properties of the inertial range [27].

In an attempt to test if the previous supposition is valid, Vadim Borue, replaced the normal Laplacian component of the Navier-Stokes equations by a higher power of the Laplacian. The Laplacian term, in a mathematical point of view, is the one responsible for the dissipation of energy in the flow, thus, a flow in which the dissipation is proportional to a higher order power of Laplacian is denominated as hyper-viscous flow [27].

Using Hyper-viscosity in DNS as been proven to have no affect in the inertial range scaling laws while it effectively increases, by an order of magnitude, the extent of the inertial range and thus the equivalent Reynolds number of the flow [28] [27] [29] [30].

The major problem in the study of the Lagrangian statistics is that the Reynolds number achievable using DNS of Newtonian fluids is not high enough to observe an inertial scaling zone. Therefore, one may wonder, whether or not, the use of Hyper-viscosity will affect the Lagrangian statistics. This is one of the fundamental question that this thesis pretends to answer.

2.4 Eulerian and Lagrangian frame

Every Lagrangian quantity of the flow will be denoted with a '+' superscript.

Unlike in the Eulerian frame, in which the statistical variable of interest is the velocity variations in space, in an Lagrangian frame, the variable of interest is the velocity variations along a particle trajectory. Thus, for the Lagrangian frame the variable of interest is:

$$\delta\vec{u}^{+}(\vec{x_0}^{+}, t, \tau) = \vec{u}^{+}(\vec{x_0}^{+}, t+\tau) - \vec{u}^{+}(\vec{x_0}^{+}, t), \tag{2.11}$$

where, $\vec{x_0}^{+}$ is the initial position, t is a certain instant of time and τ an interval of elapsed time. Due to the statistically time independence (from the initial time t) and the space homogeneity (interdependency of the initial position), the PDF of the variable will only depend on the lag time (τ). Also, due to the isotropy the PDF of each component of the velocity must be equal.

According to the K41 theory in the inertial time range, based on the three hypothesis and using dimensional analysis, one concludes that the scaling laws regarding the n-th moment of the PDF of the velocity variations of a particle along time are:

$$\overline{(\delta u_i^{+}(\tau))^n} = C_n \; \bar{\epsilon}^{\chi_n} \; \tau^{\xi_n}, \tag{2.12}$$

with $\chi_n = \frac{n}{2}$ and $\xi_n = \frac{n}{2}$ ($D_L^n = \overline{(\delta u_i^+(\tau))^n}$ is also used to denote the n-th moment of the Lagrangian velocity increments). However, as explained in section 2.1, intermittency corrections must be applied and therefore C_n is not a universal constant and χ_n and ξ_n cannot be equal to $\frac{n}{2}$. Except for n=2, because the scaling law is proportional to ϵ. Whether or not the scaling law:

$$\overline{(\delta u_i^+(\tau))^2} = C_2\, \bar{\epsilon}\, \tau, \tag{2.13}$$

is valid, has been an open problem since 1941. **Note, that this law is the equivalent, in the Lagrangian frame, to the four-fifths law, and thus the answer to this question is of extreme importance both at a fundamental level, to understand if the Kolmogorov similarity theory is valid in a Lagrangian framework, and at a practical level, because knowledge of constant C_2 is crucial to the construction of stochastic models used for contexts as industrial mixing, cloud formation, turbulent combustion or even pollutant dispersion** [1] [2] [3] [4].

To explain the difficulties of the observation, first one must defined the inertial range in a Lagrangian frame of work. In the Eulerian frame, the characteristic length scale regarding the dissipation rate is η, and the characteristic length scale regarding the largest eddies is l_0, therefore the inertial range is such that $\eta \ll |\vec{r}| \ll l_0$. In the Lagrangian frame, the characteristic dissipation time-scale τ_η, considering the Kolmogorov first similarity hypothesis, can only depend of ν and ϵ, therefore using dimensional analysis it must be:

$$\tau_\eta = (\frac{\nu}{\epsilon})^{\frac{1}{2}}, \tag{2.14}$$

using equation (2.2), results in:

$$\tau_\eta = (2S_{ij}S_{ij})^{-\frac{1}{2}}. \tag{2.15}$$

Equation (2.15) is more general because it can also be applied in the case of Hyper-viscosity therefore, it will be the one used here, also, using equations (1.1) and (2.2) it is possible to obtain $\eta = \epsilon^{\frac{1}{2}}(2S_{ij}S_{ij})^{-\frac{3}{4}}$, which will be the formula used to compute η in Hyper-viscous flows. The time-scale regarding the turn-over of the largest eddies is similar to the decorrelation time. The correlation function is defined as:

$$\rho(\tau) = \frac{\overline{u_i^+(t+\tau)u_i^+(t)}}{\overline{u_i^+(t)u_j^+(t)}}\frac{\delta_{ij}}{3}. \tag{2.16}$$

Note that when the correlation is zero, the statistics in an instant $t+\tau$ are independent of the occurrences of the instant t, thus, the decorrelation time is a parameter that measure the memory of the particle trajectory. However, $\rho(\tau)$ has an exponential decay thus, is monotonic and is only 0 when $\tau \to \infty$, therefore, the decorrelation time cannot be computed at the time where the correlation is exactly zero and it is approximated as the Lagrangian integral time (T_L), given by:

$$T_L = \int_0^\infty \rho(\tau) d\tau. \tag{2.17}$$

Finally, notice that $\overline{(\delta u_i^+(\tau))^2} = \overline{(u_i^+(t))^2 + (u_i^+(t+\tau))^2} - 2\overline{(u_i^+(t))^2}\rho(\tau)$ and since the statistics are time independent $\overline{(u_i^+(t))^2} = \overline{(u_i^+(t+\tau))^2} = \frac{2}{3}K$ (where K is the kinetic energy of the flow). Thereby, for $\tau \gg T_L$, $\rho(\tau) \approx 0$ the second order structure function is a constant given by $\overline{(\delta u_i^+(\tau))^2} \approx \frac{4}{3}K$. The behaviour of the second order structure function for $\tau \gg T_L$ is completely different to the expected for the inertial-range, therefore, $\tau \gg T_L$ is a specific range of time-scale called the integral time scale range. Thereby, the inertial-range scale must be such that $\tau_\eta \ll \tau \ll T_L$.

As already stated, the predicted scaling law for the Lagrangian velocity structure functions of second order (LVSF-2), have never been observed. It can be seen in figure 2.2 that, there is an absence of a plateau and the increase of Reynolds number simply leads to the increase of the peak value.

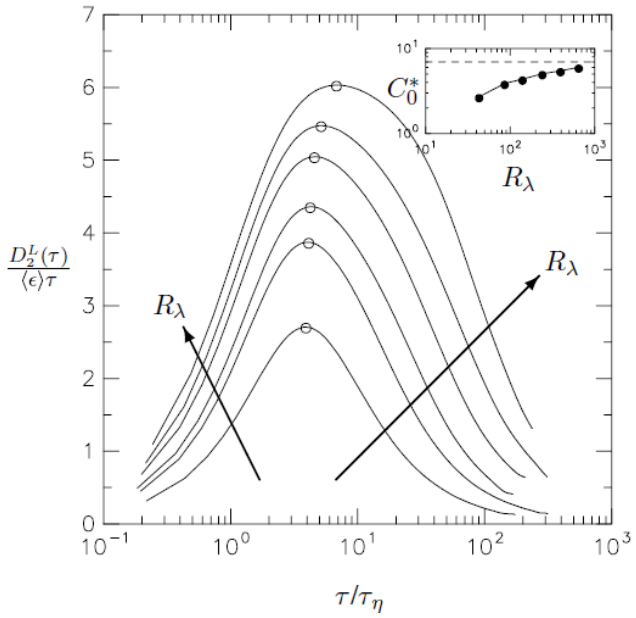

Figure 2.2: Lagrangian second order structure as function of Reynolds number. Six different curves are presented for Re_λ: 43; 86; 140; 235; 393; 648. Source: [31].

Some authors interpret the increase of this peak as an approach to the plateau [31] [32] . However, one may wonder why the inertial scale is completely visible in the Eulerian frame (see for instance [27]) while it is not in the Lagrangian frame. This situation is believed to result from the fact that $\frac{T_L}{\tau_\eta} \sim Re_\lambda$, while, $\frac{l_0}{\eta} \sim Re_\lambda^{\frac{3}{2}}$, and thereby, the same increase of the Reynolds number cause an higher extension of the inertial range in the Eulerian frame than in the Lagrangian frame. In such way that has been predicted that a clear plateau will only be observed for Reynolds numbers higher than 30000, while until now the highest Reynolds achieved was ≈ 1000 [32] [33].

Other authors raise doubts about the scaling law (2.13), using as arguments the lack of consistency with actual experimental data, that does not show any trace of a plateau, and the fact that the scaling law

as never been analytically demonstrated, unlike the four fifths law. Gregory Falkovich [34] even purposes that the scaling law is instead $\overline{\delta u_i^2(\tau)} \sim \tau^{1-\mu}$, with $\mu = 0.13 \pm 0.01$. His additional argument to support the invalidity of equation (2.13), is that, if that scaling law is valid then, in the inertial range, the acceleration autocorrelation should be zero. Moreover, for t' in the inertial range, the integral $\int_0^{t'} \overline{a_i^+(t)a_i^+(t+\tau)}\frac{\delta_{ii}}{3}d\tau$ should be equal to $0.5\ \bar{\epsilon}\ C_2$ and at the same time the integral $\int_0^{\infty} \overline{a_i^+(t)a_i^+(t+\tau)}\frac{1}{3}d\tau$ should be equal to zero. The experimental data shows that the autocorrelation of the acceleration decreases monotonically, crosses the time axis with a slope different than zero (corresponding to the time where peak is observe in the LVSF-2) and then relaxes back to zero, in a behaviour which is inconsistent with those two suppositions.

Regarding the Lagrangian velocity structure function of order n (LVSF-n), for $n \neq 2$, it is also of extreme importance to evaluate the scaling coefficients (ξ_n). However, if the inertial range width for the experimental data is not sufficient to observe a scaling law for LVSF-2, it definitely will not be sufficient to capture scaling laws for moments of higher order. To attempt computing the coefficients ξ_n, in a similar way as the procedure used in the Eulerian frame, one can use the extended self-similarity, according to which the following relation holds: $\overline{(\delta u_i^+(\tau))^n} = A_n \overline{(\delta u_i^+(\tau))^m}^{\frac{\xi_n}{\xi_m}}$. Therefore, the slope in a log-log plot of $\overline{(\delta u_i^+(\tau))^n}$ as function of $\overline{(\delta u_i^+(\tau))^m}$ is $\frac{\xi_n}{\xi_m}$. Using this approach, in order to compute the coefficient ξ_n, one must know the coefficient ξ_m. This is another reason why the verification of the scaling law (2.13) **is absolutely crucial, because it can also be used as the comparison coefficient. Presently the computation of ξ_n is made using $\xi_2 = 1$ (m=2), however as explained no experimental evidence of this law has yet been found thus, the existing predictions of ξ_n, using this method, can be completely wrong.**

Due to all of these difficulties in measuring the coefficients ξ_n, one may wonder if there is not any analytical relation between Lagrangian and Eulerian statistical quantities that allow the computation of ξ_n by knowing the coefficients ζ_n (of equations (2.3) and (2.4)). First, the relation between a time derivative in a fixed point ($\frac{\partial}{\partial t}$), and the material derivative ($\frac{D}{Dt}$) taken along a trajectory of a particle is:

$$\frac{D}{Dt} = \frac{\partial}{\partial t} + u_i \frac{\partial}{\partial x_i}. \tag{2.18}$$

The difference between the two time-derivatives is simply the convective term. However, using equation (2.18) no result regarding the relation between velocity increments in space and in a particle trajectory is extracted.

The first attempt to relate the Lagrangian and Eulerian statistics using the multifractal formalism was made by M.S. Borgas [35]. Regarding the Eulerian frame, the multifractal formalism [10] [23], assumes that a turbulent flow possess a range of scaling exponents $I = [h_{min}; h_{max}]$, i.e., a variable, say $\delta \frac{u_\parallel(\vec{r})}{u_0} \sim (\frac{|\vec{r}|}{l_0})^h$, has different scaling exponents when $|\vec{r}| \to 0$. For each set, with local exponent h, the fractal dimension associated is $D(h)$ (this can be interpreted as the size of the domain in which the scaling law has a given $h \in [h_{min}; h_{max}]$). Therefore, to compute a scaling properties of the Eulerian structure function, all contributions of the exponents must be taken into account, thus an integration over all possible h must be made, resulting in [10]:

$$\frac{\overline{(\delta\vec{u}(\vec{r}))^n}}{u_0^n} \sim \int_{h_{min}}^{h_{max}} (\frac{|\vec{r}|}{l_0})^{nh+3-D(h)} dh. \tag{2.19}$$

When $|\vec{r}| \to 0$, the power law with the smallest exponent dominates, thus, the scaling coefficient ζ_n of equation (2.3) is:

$$\zeta_n = min(nh + 3 - D(h)). \tag{2.20}$$

Notice that, it is assumed that the fractal dimension $D(h)$ and the range of scaling exponents is universal for every turbulent flows, and thereby all ζ_n are universal. If one knows all of the experimental coefficients ζ_n it is possible to obtain the function $D(h)$ by using the inverse of the Legendre transformation [36].

M.S. Borgas, using the spectral dimension regarding the energy dissipation rate and assuming the ergodic hypothesis, which states that the mean dissipation rate is the same when computed using space or time average, obtained a relation between the scaling coefficients regarding the Euler and Lagrangian frames (ζ_n and ξ_n) [35]. Even though the results does not represent correctly what is experimentally observed, this method is highly innovative and also predict the same scaling exponent for the LVSF-2 as the one predicted by the K41 theory. Finally, in this paper it was also proven that the Lagrangian statistics are much more intermittent then the corresponding Eulerian statistics, that was later verified in [15].

In the spirit of the work develop by Borgas, G. Boffeta besides using multifractal theory and the ergodic hypothesis, also stated that the velocity increments in the lagrangian frame are similar to the velocity increments in the Eulerian frame, thus [37]:

$$\delta(u_i^+(\tau)) \sim \delta(u_i(\vec{r}^+)) \quad \implies \frac{|\vec{r}^+|}{\tau} \sim \delta(u_i(\vec{r}^+)) \quad \implies \tau \sim |\vec{r}^+|^{1-h}, \tag{2.21}$$

substituting this equation in equation (2.19), and applying the same criteria used to obtain equation (2.20), one concludes that the scaling coefficient in the Lagrangian frame is such that [37]:

$$\xi_n = min(\frac{nh + 3 - D^E(h)}{1-h}), \tag{2.22}$$

where $D^E(h)$, is the fractal dimension regarding the velocity increments in the Eulerian frame (the function $D^E(h)$ has been extensively studied). Unfortunately, the use of this equations still predict scaling exponents higher than the experimental ones. R. Benzi notice that, the scaling coefficients are different for the longitudinal velocity and the transverse velocity, i.e., the fractal dimension $D^E(h)$ is not equal for both velocity increments, therefore, he suggest that the coefficient ξ_n should be in the interval with the extremes computed with equation (2.22), using the two different fractal dimensions ($D_{\parallel}^E(h)$ and $D_{\perp}^E(h)$) [38]. With this procedure, the experimental results became more consistent for higher order moments (up to n=8).

The multifractal formalism described previously had been only applied considering the inertial-range

scales. However, since all scales are dynamically related [39], L. Chevilard presented a model, obtained using the multi-fractal formalism, that describes both the inertial and dissipation time-scales [40]. This approach correctly predict the shape evolution of the probability density function, from stretched exponentials to Gaussian (this effect is shown latter in figure 4.23), with the time lag increase. Also, in this paper a more consistent relation between the Lagrangian fractal dimension and the Eulerian one was found: $D(h) = -h + (1+h)D^E(\frac{h}{1+h})$.

All the models based on the multifractal formalism, here discussed, predict that $\xi_2 = 1$, therefore, even to conclude whether or not the multifractal formalism correctly connects Eulerian and Lagrangian frames it is important to observe experimentally the scaling law given by equation (2.13).

Even though the multifractal formalism is an important tool in the prediction of the Lagrangian scaling coefficients, there is still no model that predicts correctly the Lagrangian coefficients for high order moments. Therefore, development of new models that relate Eulerian and Lagrangian frame is needed. In this direction, O. Kamps, deduced an exact relation between the two PDFs of the velocity increments [41]. However, the bridge relation requires the knowledge of a PDF of a new statistical variable, the mixed Eulerian-Lagrangian velocity increment that is the velocity variation in time in a fixed point. However the statistics of this variable are also intermittent and therefore the PDF is not known exactly. Some studies regarding this statistical variable were made [42], however, the exact PDF could not be obtained thus, using this method is still not possible to bridge, exactly the Eulerian and the Lagrangian statistics. Finally, the exact relation demonstrated that for a given time lag, the PDF of the velocity increment in a trajectory has contributions from every scales of the Eulerian frame. Thereby, Lagrangian statistics are influenced also by the Eulerian dissipative and integral length scales. This justifies the fact that to observe the inertial range in the Lagrangian frame higher Reynolds are required than in the Eulerian frame.

2.5 Single particle statistics

Even though it is tempting to connect Eulerian and Lagrangian statistics, due to the fact that the Eulerian ones are extensively studied, there are physically meaningful results in a purely Lagrangian frame that can be obtained even for low Reynolds numbers (i.e., Reynolds number not sufficient so that a scaling law is observed).

Before continuing it is important to state that the experimental results present significant differences in comparison with DNS results. However Biferale [43], stated that the errors associated in each analysis may be responsible for this apparent disagreement between experimental and DNS simulations. Regarding the DNS, there are two main contributions that can produce errors first, the interpolation of the Eulerian velocity and second the large scale anisotropy induced by the forcing scheme. Regarding the experimental simulation there are also three major sources of error, the first one is due the use of passive particle tracers in the fluid (note that the particles do not follow exactly the trajectory of fluid particles), second the presence of anisotropy fluctuations, in such way that the three velocity components do not average the same way and finally the Lagrangian velocities are computed by smoothing (with a

filter) the measured positions and then differentiating. After analysing the possible contributions of all this errors, he proved that in fact the results are consistent and that the local scaling properties of the velocity increments are in agreement.

Since, the LVSF-n for all the experimental and DNS simulations collapse, within the error intervals, it is natural to assume that, in fact, a universal behaviour exists. With this in mind A. Arnèodo and other authors (twenty six), demonstrated that multifractal description can capture the intermittency effect at all scales, which means that in fact the Lagrangian scaling laws are universal [44].

Particles can be trapped in a vortex filament, thereby, the tracers are an important tool to study the physical mechanism in these structures, this is one of the major advantages of the Lagrangian approach. When a particle is trapped in one of these structures, it experiences high velocity fluctuations, therefore, this extreme events must have some influence in the LVSF-n functions. In order to analyse these effects, first there must be applied a criterion to differentiate whether or not a particle experience these effects. In [45] it was used as criterion that a particle experienced a trapping event if the mean absolute value of the acceleration, during a time lag $2\tau_\eta$, was at least seven times superior than the root mean square of the acceleration of all particles. Filtering the statistics in order to exclude the particles that were trapped, it was possible to conclude that, the saturation of the scaling exponents ξ_n over the constant 2, for $\tau_\eta < \tau < 10\tau_\eta$ is the signature of this trapping events. By saturation of the coefficient is meant that $\lim_{n\to\infty} \xi_n = 2$, also, it is important to outline that the duration of these extreme events is also in the interval $[\tau_\eta; 10\tau_\eta]$. An example of a particle trajectory that experience this events is shown in figure 2.3. Notice that it was stated that this events are characterized by high velocity fluctuations, therefore high acceleration, thus, the next section will be dedicated to the statistics of the acceleration.

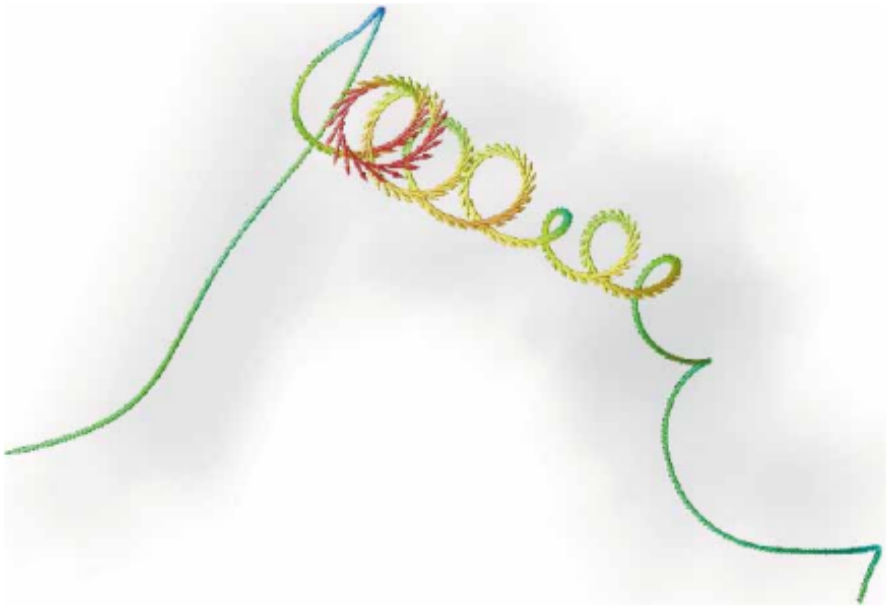

Figure 2.3: Example of a trajectory of a particle that experienced a trapping event. Source: [46].

2.5.1 Acceleration statistics

Another statistical variable that can be studied is the instantaneous acceleration of a particle:

$$a_i^+(t) = \frac{D}{Dt} u_i^+(t) \tag{2.23}$$

The PDF of this quantity has been measured experimentally in [47] and [48], and it has been proven to have an universal *behaviour* because the standardized functions, for flow with different Reynolds numbers, coincide. Regarding this variable, stochastic models have been developed in an attempt to correctly predict this PDF. In [49], accumulated evidence consistly shown that the corresponding PDF is well approximated by a Tsallis distribution, however, for extremely large accelerations there are significant deviations. In an attempt to obtain a PDF that has a better fitting, since the statistics are not completely stationary (there are oscillations in the mean dissipation rate for example), C. Beck propose the use of the concept of superstatistics [50]. In this method it is assumed that, for example, the mean value and the variance of the variable are also a statistical variables with their own PDFs. To obtain the prediction of the PDF using this method he used the stochastic Langevin equation:

$$\dot{a_i}^+ = -\gamma \frac{\partial V(a_i^+)}{\partial a_i^+} + \sigma L(t), \tag{2.24}$$

where $V(a_i^+)$ is a potential of a drift force (considering a linear force implies that $V(a_i^+) = 0.5(a^+)^2$), $\gamma > 0$ is a friction coefficient, $L(t)$ is Gaussian white noise and σ a parameter related to the strength of the noise, and then since parameters γ and σ vary along the time, it is assumed that they fluctuate in such way that $\beta = \frac{\gamma}{\sigma^2}$ has a log-normal probability density given by:

$$f(\beta) = \frac{1}{\beta s 2\pi} exp(-\frac{(log\frac{\beta}{m})^2}{2s^2}), \tag{2.25}$$

where s is a fitting coefficient. Considering this, results that the standardized probability function $\tilde{p}(\tilde{a}^+)$ obtained by solving equation (2.24) (where $\tilde{a}^+$ is equal to a^+ adimensionalized by it's root mean square) is equal to:

$$\tilde{p}(\tilde{a}^+) = \frac{1}{2\pi s} \int_0^\infty \beta^{-\frac{1}{2}} exp(-\frac{(log\frac{\beta}{m})^2}{2s^2}) e^{-\frac{1}{2}\beta\tilde{a}^+} d\beta \ . \tag{2.26}$$

Choosing the free parameter s that makes the better fit to the experimental curve, it is possible to obtain a prediction of $\tilde{p}(\tilde{a}^+)$ that agrees with the experimental results up to $|\tilde{a}^+| < 60$, in which $\tilde{p}(\tilde{a}^+) \sim 10^{-9}$. Also, by increasing the Reynold number it seems that $s^2 \to 3$, if this hypothesis holds no free parameters would be left and thereby these statistics would be universal.

One may wonder why the superstatistical method is not also applied to the velocity fluctuations. Notice that in the case of the the velocity increments the main question is the understanding of how the LVSF-n scales with time, not to describe the shape of the PDF. Also, due to intermittency the PDF varies along the time and therefore log-normal density function could only be used in certain time intervals. However, for small time lags, where the relation $a_i^+ \approx \frac{\delta u_i^+}{\tau}$ is valid, it is possible to obtain good prediction

of the standardized PDF of the velocity increments using this method [51].

L. Biferale [52] also attempt to compute the PDF of the acceleration using the multifractal formalism. It has the advantage of not having any free parameters (which is non-physical) , however, the superstatistical model still presents results more coherent with both experimental and numerical data.

2.6 Multi-particle statistics

Another statistical variable of interest is a particle displacement between its position and the center of mass of a cluster of particles (in which the particle is embodied) in a turbulent flow. The study of this subject, the turbulent relative dispersion, has innumerable applications. Cloud formation is one of the most interesting ones [9] [53]. Also, it is possible to relate the Lagrangian statistics of particle dispersion with the statistics of passive scalars, therefore, particle dispersion is important in the study of turbulent mixing, combustion and pollution [54].

This variable can be defined as:

$$\delta\vec{r}^{+}(t,\tau) = \vec{r}^{+}(t+\tau) - \vec{r}^{+}(t), \tag{2.27}$$

where $\vec{r}^{+}(t)$ is the distance between the particle position and the center of mass (this distance, for the initial time, is also denoted by $\vec{r}_0^{+}$). Once more, the statistics are independent of the initial time (they do not depend on t), and due to isotropy, the statistics of this variable are independent of the direction therefore, the variable of interest is simply:

$$\delta|\vec{r}^{+}(\tau)| = |\vec{r}^{+}(t+\tau)| - |\vec{r}^{+}(t)|. \tag{2.28}$$

In 1926, L.F. Richardson [53], using experimental results, obtained by releasing balloons and measuring the position where they land and the time travelled, notice that the root mean square of the variable (2.28) was proportional to the cubic power of time. However, only in 1950, using the Kolmogorov similarity theory, G. Batchelor [55], stated that in the inertial time sub-range the variance, for initial separation in the inertial subrange, is given by:

$$\overline{(\delta|\vec{r}^{+}(\tau)|)^2} = g\epsilon t^3, \tag{2.29}$$

where g is a universal constant. **This law is known as the T3 Richardson law, which is assumed to be universal. However, this relation has never been experimentally observed, and like the scaling law of the LVSF-2 it is assumed that the reason why this scaling law has not yet been seen is due to the limitations of the Reynolds number. Some estimations were made for the constant g which is supposed to be $g \approx 0.6$, however, only for a very small range of initial separations it is possible to observe, poorly, the scaling law [56]. Thus, whether or not the scaling law** (2.29) **is valid is a fundamental problem in turbulence.**

In an attempt to close this problem L. Biferale [57] consider a different variable, which is, the time

required for a particle to exit the sphere, with centre coincident to the center of mass, with radius r. The statistics of this variable show a clear scaling range, however, to relate them with the statistics of the displacement a model must be used, therefore, it still is not an absolute proof of the existence of the scaling law.

This statistic can be evaluated using only two particles. The major advantage is that it is not required to compute the position of the center of mass, since the distance between the two particles is twice the distance of each particle to the mass center.

Another research field of interest is the analysis of the shape evolution of tetrads. The evolution of the shape of this structures is intimately connected to the dynamics of the eddies with a size similar to its linear dimension [17] [58]. The geometrical shape of a tetrad, can be defined using 4 parameters (because a tetrad is a structure with 4 points), however, in homogeneous turbulence the position of the center of mass is irrelevant therefore only three parameters are required. The parameters used to characterized the shape are the three eigenvalues of the moment of inertia tensor. A scaling law proportional to t^3, with different coefficients for each parameter can be obtained on theoretical grounds. However, this scaling law has never been observed and thus if whether it is valid or not is another open problem in turbulence.

Chapter 3

Numerical Methods and Code Implementation

3.1 Governing Equations

Considering a fluid as a continuum, and using the fundamental laws of physics, i.e., the conservation of mass (equation (3.1)), momentum (equation (3.2)) and energy (equation (3.3)) it is possible to obtain a set of equations that govern the velocity field of fluid motion, which are (using Einstein notation) [59]:

$$\frac{\partial \rho}{\partial t} + \frac{\partial (\rho u_i)}{\partial x_i} = 0, \tag{3.1}$$

$$\frac{\partial (\rho u_i)}{\partial t} + \frac{\partial (\rho u_i u_j)}{\partial x_j} = -\frac{\partial p}{\partial x_i} + \frac{\partial (\tau_{ji})}{\partial x_j} + \rho f_i, \tag{3.2}$$

$$\frac{D(e + \frac{u_i u_i}{2})}{Dt} = \rho \dot{q} + \frac{\partial}{\partial x_i}(k \frac{\partial T}{\partial x_i}) - \frac{\partial (u_i p)}{\partial x_i} + \frac{\partial (u_i \tau_{ji})}{\partial x_j} + \rho f_i u_i, \tag{3.3}$$

where ρ is the volumetric mass, p is the pressure, τ_{ij} is the stress tensor, f is a momentum source term, e is the internal energy, $\dot{q}$ is an energy source term and T is the temperature.

It is important to state that the continuum hypothesis is based on the assumption that all space is *filled* with material, even though, this is not true in a molecular level, since there are empty spaces between atoms, the results obtained using this approximation are highly accurate. It is important to notice that this approximation in only valid when the distance between atoms is much smaller than the characteristic length of the body. Also, in a continuum all quantities, such as velocity or displacement, vary continuously thus, their spatial derivatives exist and are continuous which means that Calculus theory can be applied [60].

The set of five differential equations as presented in (3.1), (3.2) and (3.3) are not closed, which means that there are more unknowns than equations. To close the set of equations it is required a new one, it important to notice that the previous equations are completely general and applicable to all fluids,

however, not all fluids behave in the same manner, therefore, the new one must be related to the nature of the fluid, i.e, its physical properties.

In the seventeenth century Newton stated that the shear stresses are proportional to the strain rate. The fluids that have this property are called Newtonian fluids. The most common fluids (water and air) are well modelled with this approximation. However, there are cases in which this model is not valid, for example in blood, because the viscosity decreases with a stress increase.

For Newtonian fluids, Stokes deduced the constitutive equations:

$$\tau_{ij} = 2\mu(\frac{\partial u_i}{\partial x_j} + \frac{\partial u_j}{\partial x_i}) - \frac{2}{3}\mu\frac{\partial u_k}{\partial x_k}\delta_{ij}, \tag{3.4}$$

in which δ_{ij} is the Kronecker delta, that is 1 if i=j and 0 otherwise, and μ is the dynamic viscosity.

Using the Stokes constitutive relation and considering incompressibility (ρ is constant), one obtain the Navier-Stokes equations ((3.5) and (3.6)) for Newtonian incompressible fluids. These are the equations that will be solved in all the Direct Numerical Simulations carried out in this work.

$$\frac{\partial u_i}{\partial x_i} = 0, \tag{3.5}$$

$$\frac{\partial u_i}{\partial t} + u_j\frac{\partial u_i}{\partial x_j} = -\frac{1}{\rho}\frac{\partial p}{\partial x_i} + \nu\frac{\partial^2 u_i}{\partial x_j \partial x_j} + f_i. \tag{3.6}$$

It is important to notice that in the previous set of 4 equations, there are only 4 independent variables which are the pressure (p) and the three velocity components (u_1, u_2 and u_3). Thus this set of equations are closed.

Finally, the kinematic viscosity ν is the ratio of the dynamic viscosity μ to the volumetric mass density ρ, thus: $\nu = \frac{\mu}{\rho}$

3.2 Direct Numerical Simulations

As stated in section 1.4, DNS consists in, given an initial state and boundary conditions, solve directly the Navier–Stokes equations by resolving all the scales of motion.

The first simulation of turbulent flow using DNS was made in 1972 by Orszag [61], and even though it was a simulation with low Reynolds Number ($Re_\lambda = 35$ low comparing to Reynolds number achievable with current computational power), it was a demonstration that three-dimensional turbulent flows could be simulated with pseudo-spectral methods. An important result because, as also stated in section 1.4, with these numerical simulations it is possible to compute with high precision the quantities involved in the flow such as velocity or scalar fields.

As explained in the previous chapter, the higher the Reynolds number, the larger the inertial sub-range scale, which is believed to have universal scaling laws. Therefore, for a fundamental study of turbulence it is important to analyse simulations with the highest Reynolds number possible. Due to this fact, many turbulence research in a fundamental level is made with the use of Homogeneous Isotropic

Turbulence, because, by avoiding complex geometries, non-homogeneous effects and using spectral discretization, these simulations allows the achievement of the highest Reynolds number for a given computational resource.

3.3 Simulation Description

The numerical work developed and implemented in this work concerns the Hyper-viscosity (section 3.3.8) and the particle tracking (section 3.4). Also, some relevant aspects in the code developed during the this work are highlighted in section 3.5.

3.3.1 Computational Domain and Boundary Conditions

The computational domain of the simulations consists in a cube with dimension $(2\pi)^3$.

In an Homogeneous Isotropic Turbulent simulation periodicity is imposed as the boundary condition, which means:

$$u_i(0,0,0,t) = u_i(2\pi,0,0,t), \tag{3.7}$$

$$u_i(0,0,0,t) = u_i(0,2\pi,0,t), \tag{3.8}$$

$$u_i(0,0,0,t) = u_i(0,0,2\pi,t). \tag{3.9}$$

Since spectral methods are used for spatial discretization these three conditions are immediately verified.

Besides that, in Homogeneous Isotropic Turbulence all mean (averaged in space) velocity components must be zero. This condition in the Fourier Space can be simply stated as:

$$\hat{u_i}(0,0,0,t) = 0. \tag{3.10}$$

The definitions of the velocity components in the Fourier space, $\hat{u_i}(0,0,0,t)$, will be made in the following section.

3.3.2 Spatial Discretization

The numerical code used here uses pseudo-spectral schemes. This type of scheme is chosen because it has important advantages, such as, high accuracy of the spatial derivatives in physical space since they are computederror close to the machine accuracy. Spectral methods became computationally more appealing when the Fast Fourier Transform (FFT) algorithm was invented. With this new algorithm, the time required for a Fourier transform became proportional to $N \cdot log(N)$, instead of N^2, where N is the number of points used.

The underlying principle of spectral methods is that it is possible to represent a function with temporal and spatial dependence in terms of frequencies or wavenumbers, respectively. Specifically, a general

function (ψ), periodic in x,y and z coordinates with wavelength L_x,L_y,L_z respectively, can be written as:

$$\psi(x,y,z,t) = \sum_{l=-\infty}^{\infty} \sum_{m=-\infty}^{\infty} \sum_{n=-\infty}^{\infty} \hat{\psi}(k_l,k_m,k_n,t) e^{i(k_l x + k_m y + k_n z)}, \tag{3.11}$$

where $i = \sqrt{-1}$ and the wavenumbers k_l,k_m and k_n are defined as:

$$k_l = l\frac{L_x}{2\pi} \qquad k_m = m\frac{L_y}{2\pi} \qquad k_n = n\frac{L_z}{2\pi}. \tag{3.12}$$

Note that since the computational domain is a cube with linear dimension equal to 2π then, k_l, k_m and k_n will be integers which decreases the computational effort. Also, in equation (3.11) $\hat{\psi}(k_l,k_m,k_n,t)$ is a complex function, however, since $\psi(x,y,z,t)$ is real, $\hat{\psi}(k_l,k_m,k_n,t)$ possesses the Hermitian property therefore, $\hat{\psi}(-k_l,k_m,k_n,t) = \hat{\psi}^*(k_l,k_m,k_n,t)$, this results from the fact that the real part of $\hat{\psi}(k_l,k_m,k_n,t)$ is an even function and the imaginary part is an odd function. Due to this property, one can reduce the amount of stored values of $\hat{\psi}(k_l,k_m,k_n,t)$ to half (storing only the values for positive wavelengths) in each direction and thus eight times in total. Note that, ψ^* is the complex conjugate of ψ

Due to the ortogonality of the basis used in the Fourier series the computation of $\hat{\psi}(k_l,k_m,k_n,t)$ is made using the following operation:

$$\hat{\psi}(k_l,k_m,k_n,t) = \frac{1}{L_x L_y L_z} \int_{-L_z/2}^{L_z/2} \int_{-L_y/2}^{L_y/2} \int_{-L_x/2}^{L_x/2} \psi(x,y,z,t) e^{-i(k_l x + k_m y + k_n z)} dx dy dz. \tag{3.13}$$

Taking the limit to infinity of L_x,L_y and L_z then, if the function ψ is absolute integrable, one obtain the Fourier Transform:

$$\mathcal{F}(\psi(x,y,z,t)) = \hat{\psi}(k_l,k_m,k_n,t) = \int_{-\infty}^{\infty} \int_{-\infty}^{\infty} \int_{-\infty}^{\infty} \psi(x,y,z,t) e^{-i(k_l x + k_m y + k_n z)} dx dy dz. \tag{3.14}$$

The inverse operation, i.e., the computation of the function in the real space knowing the analogous function in the Fourier space, is made using the inverse Fourier Transform:

$$\mathcal{F}^{-1}(\hat{\psi}(k_l,k_m,k_n,t)) = \psi(x,y,z,t) = \int_{-\infty}^{\infty} \int_{-\infty}^{\infty} \int_{-\infty}^{\infty} \hat{\psi}(k_l,k_m,k_n,t) e^{i(k_l x + k_m y + k_n z)} dk_l dk_m dk_n. \tag{3.15}$$

It is important to notice that the function obtained using equation (3.13) is discrete, unlike the one obtained using the Fourier transform which is continuous. However, our domain is finite therefore, the function $\hat{\psi}(k_l,k_m,k_n,t)$ will be discrete in the Fourier space. Also, since the domain in the computations will be discretized then the function $\hat{\psi}(k_l,k_m,k_n,t)$ besides of being discrete will also have non-zero values for a finite number of wavelengths. The maximum wavenumber in each direction, k_l, k_m and k_n, for which the function $\hat{\psi}(k_l,k_m,k_n,t)$ can be correctly measured, is according to the Nyquist–Shannon sampling theorem equal to $\frac{N_x}{2}-1$, $\frac{N_y}{2}-1$ and $\frac{N_z}{2}-1$, where, N_x, N_y and N_z are the number of grid points of the discretization in x,y, and z direction, respectively.

Considering the previous paragraph, it is clear that any function of interest in the turbulent simulation in the Fourier space will be written as (instead of the version shown in (3.11)):

$$\psi(x,y,z,t) = \sum_{l=-N_x/2+1}^{N_x/2-1} \sum_{m=-N_y/2+1}^{N_y/2-1} \sum_{n=-N_z/2+1}^{N_z/2-1} \hat{\psi}(k_l,k_m,k_n,t) e^{i(k_l x + k_m y + k_n z)} \tag{3.16}$$

The equation (3.16), allows the computation of the function $\psi(x,y,z,t)$ if one knows its analogous in the Fourier space ($\hat{\psi}(k_l,k_m,k_n,t)$). To compute the function $\hat{\psi}(k_l,k_m,k_n,t)$, when it is known $\psi(x,y,z,t)$, one should use the relation:

$$\hat{\psi}(k_l,k_m,k_n,t) = \sum_{a=1}^{N_x} \sum_{b=1}^{N_y} \sum_{c=1}^{N_z} \psi(x_a,y_b,z_c,t) e^{-i(k_l x_a + k_m y_b + k_n z_c)}, \tag{3.17}$$

where x_a, y_b and z_c are the grid points that can be computed as:

$$x_a = L_x \frac{a-1}{N_x} \qquad y_b = L_y \frac{b-1}{N_y} \qquad z_c = L_z \frac{c-1}{N_z}. \tag{3.18}$$

As stated in the beginning of this section, the major advantage of the use of spectral methods is that a derivative in the real space can be computed using a single algebraic operation in the Fourier space. This property can be deduced by simply making a spatial derivative in equation (3.11), resulting in:

$$\widehat{\frac{\partial \psi}{\partial x_j}} = i k_j \hat{\psi} \tag{3.19}$$

De-aliasing

Aliasing errors, in the case of a time dependent signal, occur due the fact that the sample rate is not sufficient to capture all frequencies originating a false lower frequency component. Therefore, the predicted signal becomes different from the real one.

Theoretically, aliasing errors should be removed when the spatial sample verifies the requirements imposed by the Nyquist–Shannon sampling theorem, however, in practical matters this effect is still observed and thus a more restrictive condition must be imposed.

The one adopted was applying a spectral cut-off filter, meaning that, all Fourier coefficients for all wavenumbers with an absolute value greater than a wavenumber, k_{cut}, are set to zero. The cut-off used in this code is $k_{cut} = \frac{2}{3} k_{max}$, where $k_{max} = \frac{min(N_x,N_y,N_z)}{2} - 1$ [62].

3.3.3 Navier-Stokes equations in Fourier Space

The evolution of the Fourier modes in a turbulent flow is govern by the Navier-Stokes equations in Fourier Space. The deduction of those equations will be presented in this section. Starting by applying the Fourier transform to both sides of equation (3.5), and recalling the property (3.19), one obtains the continuity equation in the Fourier space:

$$i k_j \hat{u_j} = 0 \quad \Leftrightarrow \quad \vec{k} \cdot \vec{\hat{u}} = 0 \tag{3.20}$$

Equation (3.20) implies that the velocity in the Fourier space must be in a plane normal to the wavenumber vector.

Regarding the momentum equations another important property can be deduced. To derive this property the Navier-Stokes momentum equations in the rotational form will be used.

$$\frac{\partial \vec{u}}{\partial t} = \vec{u} \text{ x } \vec{\Omega} - \vec{\nabla}(\frac{p}{\rho} + \frac{\vec{u} \cdot \vec{u}}{2}) + \nu \nabla^2 \vec{u} + \vec{f}. \tag{3.21}$$

In equation (3.21) $\vec{u}$ is the velocity vector, $\vec{\Omega}$ is the vorticity vector (the rotational of the velocity field $\vec{\nabla}$x$\vec{u}$), the operation x denotes the cross product between two vectors, $\vec{\nabla}$ is the gradient of a scalar field and finally, ∇^2 is the Laplace operator and $\vec{f}$ is the forcing vector.

Applying the Fourier transform to both sides of equation (3.21), results in:

$$\frac{\partial \hat{\vec{u}}}{\partial t} = \widehat{\vec{u} \text{ x } \vec{\Omega}} - i\vec{k}(\widehat{\frac{p}{\rho} + \frac{\vec{u} \cdot \vec{u}}{2}}) - \nu(\vec{k} \cdot \vec{k})\hat{\vec{u}} + \hat{\vec{f}}. \tag{3.22}$$

Applying the the inner product with $\vec{k}$ in both sides of equation (3.22), taking into account property (3.20) and performing some basic algebraic operations, one obtains:

$$\widehat{(\frac{p}{\rho} + \frac{\vec{u} \cdot \vec{u}}{2})} = -i\frac{\vec{k} \cdot \widehat{\vec{u} \text{ x } \vec{\Omega}}}{\vec{k} \cdot \vec{k}}. \tag{3.23}$$

Note that the forcing term disappears because the forcing is divergence free, i.e, $\vec{k} \cdot \hat{\vec{f}} = 0$. (See section 3.3.6)

Substituting $\widehat{(\frac{p}{\rho} + \frac{\vec{u} \cdot \vec{u}}{2})}$ obtained in equation (3.23) into equation (3.22) yields:

$$\frac{\partial \hat{\vec{u}}}{\partial t} = \widehat{\vec{u} \text{ x } \vec{\Omega}} - \vec{k}\frac{\vec{k} \cdot \widehat{\vec{u} \text{ x } \vec{\Omega}}}{\vec{k} \cdot \vec{k}} - \nu(\vec{k} \cdot \vec{k})\hat{\vec{u}} + \hat{\vec{f}}. \tag{3.24}$$

In equation (3.24), $\widehat{\vec{u} \text{ x } \vec{\Omega}} - \vec{k}\frac{\vec{k} \cdot \widehat{\vec{u} \text{ x } \vec{\Omega}}}{\vec{k} \cdot \vec{k}}$ is the projection of the non-linear term $\widehat{\vec{u} \text{ x } \vec{\Omega}}$ into the the plane normal to the wave number vector $\vec{k}$. An important property of the equations in the Fourier space is that, the term $\vec{\nabla}(\frac{p}{\rho} + \frac{\vec{u} \cdot \vec{u}}{2})$ is the component of the non-linear term parallel to wavenumber vector and thus, using equation (3.24) makes the knowledge of the pressure unnecessary during the simulation.

Finally, it is important to state that to compute the Fourier transform of the non-linear terms it is necessary to have both terms $\vec{u}$ and $\vec{\Omega}$ in the real space, compute the cross product operation, also in the real space, and only then make the Fourier transform. It is also possible to compute the non-linear term using only $\hat{\vec{u}}$ and $\hat{\vec{\Omega}}$, however the operation required to do this is a convolution integral that is computational more expensive than the approach implemented.

3.3.4 Temporal Discretization

The temporal discretization adopted is an explicit third order low storage Runge-Kutta scheme [63].

The advantage of this method is that the implementation requires less memory space than a regular Runge-Kutta scheme. To explain this method the Navier-Stokes equation in Fourier space will be used

in the form:

$$\frac{\partial \hat{\vec{u}}}{\partial t} = N(\hat{\vec{u}}) + L(\hat{\vec{u}}) + \hat{\vec{f}}, \tag{3.25}$$

Or in an integral form (where τ is an arbitrary instant of time and Δt is a time interval):

$$\hat{\vec{u}}(k_l, k_m, k_n, \tau + \Delta t) = \hat{\vec{u}}(k_l, k_m, k_n, \tau) + \int_{\tau}^{\tau+\Delta t} (N(\hat{\vec{u}}) + L(\hat{\vec{u}}) + \hat{\vec{f}})dt, \tag{3.26}$$

where,

$$N(\hat{\vec{u}}) = \widehat{\vec{u} \times \vec{\Omega}} - \vec{k}\frac{\vec{k} \cdot \widehat{\vec{u} \times \vec{\Omega}}}{\vec{k} \cdot \vec{k}}, \tag{3.27}$$

and,

$$L(\hat{\vec{u}}) = -\nu(\vec{k} \cdot \vec{k})\hat{\vec{u}}. \tag{3.28}$$

The reason why this two terms are presented separately is due to the fact that in the code implementation there are two routines to compute each term and also because the implementation of the Hyper viscosity, as it will be seen in section 3.3.8, will be made simply using a different viscous term ($L(\hat{\vec{u}})$).

The scheme used to integrate in order of time requires the application of three sub-steps. In each step the following equations are used:

$$\begin{cases} h_{j+1} = \alpha_j h_j + N(\hat{\vec{u}}_j) + L(\hat{\vec{u}}_j) + \hat{\vec{f}}(\tau_j) \\ \hat{\vec{u}}_{j+1} = \hat{\vec{u}}_j + \beta_j \Delta t \cdot h_{j+1} \\ \tau_{j+1} = \tau_1 + \gamma_j \Delta t \end{cases} \tag{3.29}$$

Note that in the set of equations (3.29) h is an auxiliary variable initially valued with 0 and the subscript j is such that if is equal to 1 refers to the values in the beginning of the time step while if it is 4 is the final value obtained after the time integration (each sub-step causes an increment of j).

The coefficients α_j, β_j and γ_j have the values pointed out in equations (3.30), (3.31) and (3.32)

$$\alpha_1 = 0 \qquad \alpha_2 = -\frac{5}{9} \qquad \alpha_3 = -\frac{153}{128}, \tag{3.30}$$

$$\beta_1 = \frac{1}{3} \qquad \beta_2 = \frac{15}{16} \qquad \beta_3 = \frac{8}{15}, \tag{3.31}$$

$$\gamma_1 = \frac{1}{3} \qquad \gamma_2 = \frac{3}{4} \qquad \gamma_3 = 1. \tag{3.32}$$

Also, even though it is not specified in the set of equations (3.29), the continuity equation in the Fourier space ((3.20)) is also solved in every sub-step.

3.3.5 Numerical stability

The time step Δt, due to stability issues, must be restricted in size during a numerical resolution of a system of partial differential equations [64]. The parameter governing the numerical stability, depends on the type of partial differential equation. For dispersion the adimensional parameter is $\nu\frac{\Delta t}{(\Delta x)^2}$, for convection problems, the adimensional parameter is the Courant number which is $\frac{\Delta t}{\Delta x}|u|_{max}$.

Notice that the main goal here is to have the highest Reynolds number, which can be obtain by decreasing ν, when $\nu \to 0$, then $\nu\frac{\Delta t}{(\Delta x)^2} \to 0$ meaning that the stability requirements regarding dissipation, when $\nu \to 0$, will be respected independently of the choice of Δt. Navier stokes equations have both convective terms and dissipative, however, using the previous argument, one realizes that convection effects dominate, thus the more restrictive stability condition is the one imposed by the Courant number.

The condition used to ensure the stability of the third order low-storage Runge-Kutta method is the following:

$$C_{fl} \leq 0.6, \tag{3.33}$$

in which C_{fl}=$\frac{\Delta t}{\Delta x}|u|_{max}$, consequently the time-step used in each iteration is given by:

$$\Delta t = 0.6\frac{\Delta x}{|u|_{max}}. \tag{3.34}$$

Condition (3.34) is only used until the flow is statistically stationary, after that, tracers are embedded in the flow and the time-step in each iteration is made constant, for statistical purposes. The used Δt during the particle tracing is chosen in such way to ensure that the stability condition (3.33) is always verified.

For Hyper viscous simulations, the stability condition is more restrictive, and the Courant number must verify the condition [28]:

$$C_{fl} \leq 0.2 \ . \tag{3.35}$$

3.3.6 Forcing method

It is obvious that, without injecting energy in Homogeneous Isotropic flow, due to dissipation effects, energy will tend to 0. To have a statistically stationary flow a forcing method is required.

In the presentation of the Navier-Stokes momentum equations (3.6), in the right side of the equation there is a forcing term, this term will now be detailed. The forcing method used is fully descripted in [65].

The forcing method is not a natural feature and therefore, one may question about how the results are physically meaningful when non-physical features are included (forcing). Thus, to make sure that the forcing does not affect the results it must have several specific properties.

First, it must be completely random to make sure that it is uncorrelated with the velocity field so that it does not particularly enhance a certain time scale in an unknown way. Also it needs to be completely independent of $\hat{u}_i(k_l, k_m, k_n, t)$, to ensure that the statistically stationary state is completely independent

of the initial conditions [65]. If it is independent of $\hat{u}_i(k_l, k_m, k_n, t)$, consequently, it can only depends on the wavenumbers and time ($\hat{f}_i(k_l, k_m, k_n, t)$).

Second, during the deduction of equation (3.24) it was required that the forcing was divergent free, i.e., $\vec{k} \cdot \hat{\vec{f}} = 0$. This means that the forcing must be in a plane normal to $\vec{k}$, thus, $\hat{\vec{f}}$ can only have two independent components. If the forcing can only have two components and only depend on the wavenumber it can be written as:

$$\hat{\vec{f}} = A_{rand}(\vec{k}, t).\vec{e_1'} + B_{rand}(\vec{k}, t).\vec{e_2'} \ , \tag{3.36}$$

where $\vec{e_1'}$ and $\vec{e_2'}$ are unit vectors perpendicular to $\vec{k}$ given by:

$$\vec{e_1'} = (\frac{k_m}{\sqrt{k_l^2 + k_m^2}}, -\frac{k_l}{\sqrt{k_l^2 + k_m^2}}, 0), \tag{3.37}$$

$$\vec{e_2'} = (\frac{k_l k_n}{\sqrt{k_l^2 + k_m^2} \cdot |k|}, \frac{k_m k_n}{\sqrt{k_l^2 + k_m^2} \cdot |k|}, \frac{\sqrt{k_l^2 + k_m^2}}{|k|}). \tag{3.38}$$

where $A_{rand}(\vec{k}, t)$ and $B_{rand}(\vec{k}, t)$ are functions given by:

$$A_{rand}(\vec{k}, t) = (\frac{F(\vec{k})}{2\pi |k|^2}) e^{i\theta_1} g_A(\phi), \tag{3.39}$$

$$B_{rand}(\vec{k}, t) = (\frac{F(\vec{k})}{2\pi |k|^2}) e^{i\theta_2} g_B(\phi), \tag{3.40}$$

where $F(\vec{k})$ is the force spectrum that is imposed by the specifications regarding the intensity, wavenumber peak and wavenumber width of the forcing. g_A and g_B are two real functions that must verifiy the equality $g_A^2 + g_B^2 = 1$, the ones used in the code implementation are $g_A = sin(2\phi)$ and $g_B = cos(2\phi)$, where ϕ is a uniformly distributed random parameter in the range $[0; \pi]$.

To ensure that each Fourier mode of the force has no correlation with the velocity field, θ_1 and θ_2 must be such that:

$$Re\{A^*_{rand}(\hat{\vec{u}} \cdot \vec{e_1'}) + B^*_{rand}(\hat{\vec{u}} \cdot \vec{e_2'})\} = 0 \ . \tag{3.41}$$

Besides equation (3.41), θ_1 and θ_2 must be such that ψ given by $\psi = \theta_1 - \theta_2$, is also random variable uniformly distributed in the interval $[0; 2\pi]$.

Finally the spectrum force is given by:

$$F(\vec{k}) = A e^{(-\frac{(|\vec{k}| - k_f)^2}{c})}, \tag{3.42}$$

where k_f is the peak forcing wavenumber and c determines its degree of concentration. The width of the wavenumber forcing can be different for different simulations therefore, the forcing will be active in an interval, say, $|\vec{k}| \in [k_a; k_b]$. To make sure that the energy injection rate has a specific value P (that in a statistically stationary simulation is $\approx \epsilon$), the value of A is such that:

$$A = \frac{P}{\Delta t} \frac{1}{\int_{|\vec{k_a}|}^{|\vec{k_b}|} (Ae^{(-\frac{(|\vec{k}|-k_f)^2}{c})}) d|\vec{k}|}. \tag{3.43}$$

3.3.7 Parallel computational approach

To handle parallel computation the code implemented uses *2DECOMP&FFT* library [66]. It is a software framework designed for large-scale parallel applications using three-dimensional structured mesh. Using this library, the whole domain is decomposed in 2D pencils as shown in figure 3.1, and each processor deals with the data regarding its sub-domain. To deal with communications between cores, it relies on Message Passing Interface (MPI).

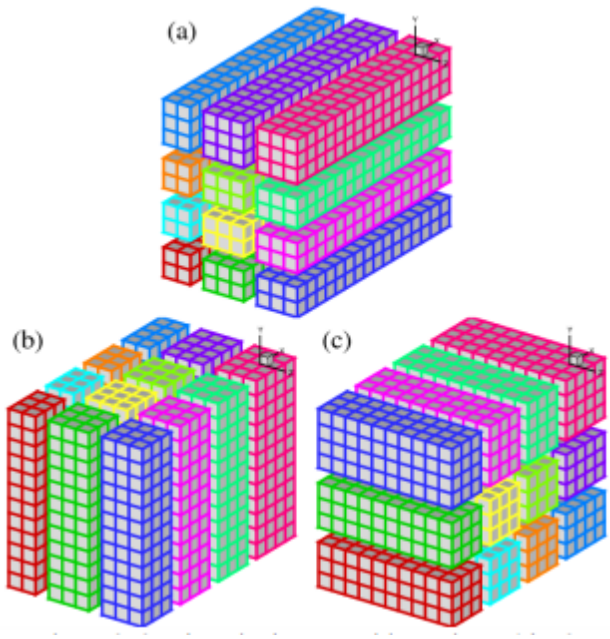

Figure 3.1: 2D domain decomposition using a 4 by 3 processor grid. Source: [66].

A very important feature is that it also provides a highly scalable and efficient interface to perform three-dimensional FFTs. The one that will be used here is the Fast Fourier in the West (FFTW) [67].

By using this software it is possible to obtain scalability for a number of cores until the order of $\sim 10^5$.

3.3.8 Hyper-viscosity

The Hyper-viscosity modified Navier-Stokes momentum equations are [27]:

$$\frac{\partial u_i}{\partial t} + u_j \frac{\partial u_i}{\partial x_j} = -\frac{1}{\rho}\frac{\partial p}{\partial x_i} + (-1)^{h+1}\nu_h \Delta^h u_i + f_i, \tag{3.44}$$

in which, h is the hyper-viscosity coefficient. In all simulations performed here h was taken to be $h = 8$. Also, ν_h is the hyper-viscosity coefficient that is chosen to be such that [27]:

$$\nu_h(\frac{N}{2})^{2h}\Delta t = 0.5\ . \tag{3.45}$$

Note that to apply the third-order Runge-Kutta scheme in an hyper viscous flow, one must use $L(\hat{\vec{u}})$ in equation (3.26) as:

$$L(\hat{\vec{u}}) = (-1)^{h+1} \cdot i^h \nu_h |\vec{k}|^h \hat{\vec{u}}. \tag{3.46}$$

To compute the dissipation it is necessary to use the following formula:

$$\epsilon = \nu_h(\nabla^{\frac{h}{2}}\hat{\vec{u}} \cdot \nabla^{\frac{h}{2}}\hat{\vec{u}}). \tag{3.47}$$

To compute the equivalent Reynolds, the following formula will be used [27]:

$$Re_\lambda = C_h(\frac{k_d}{k_f})^{\frac{2}{3}}. \tag{3.48}$$

Where k_d is the wavenumber where the maximum of vorticity occurs (in the spectrum). k_f, as discussed before, is where the forcing peak is localized. Finally C_h is a constant that depends on the hyper-viscosity coefficient. For $h = 8$, $C_8 \approx 50$.

3.4 Particle Tracking

3.4.1 Governing equations

The cinematic equation of the velocity is simply:

$$\frac{dx_j^+(t)}{dt} = u_j^+(t) \tag{3.49}$$

The velocity of the particle (Lagrangian framework) is related to the velocity computed in the Eulerian framework. Since the particles are non inertial, the velocity of each one must be the velocity in the Eulerian frame in the position $\vec{x}^+(t)$. Thus, the ordinary differential equation that must be solved in order to know the particle trajectories is:

$$\frac{dx_j^+(t)}{dt} = u_j(\vec{x}^+, t). \tag{3.50}$$

Note that equation (3.50) is only valid for non inertial particles, for inertial ones, the Newton's second law of motion must be used instead of a cinematic relation.

Regarding the initial conditions, a defined number of particle tracers are spread randomly in all the domain, i.e., every particle initial position/coordinates is/are a uniformly distributed random variable. This is important to erase possible probabilistic dependence of initial position.

3.4.2 Temporal Discretization

To solve equation (3.50) one must known the velocity field in the Eulerian framework in every time-step, consequently, the temporal discretization must be the same as the one used to compute the Eulerian velocity field.

This means that the time interval Δt and the scheme used to integrate in time equation (3.50) is the one introduced in section 3.3.4.

To explain how the implementation is made first we need to put equation (3.50) in its integral form:

$$\vec{x}^{+}(\tau + \Delta t) = \vec{x}^{+}(\tau) + \int_{\tau}^{\tau+\Delta t} \vec{u}(\vec{x}^{+}(t), t)dt. \tag{3.51}$$

As stated in section 3.3.4 the scheme used to integrate in time requires the application of three sub-steps. In each step the following equations are used:

$$\begin{cases} h_{j+1} = \alpha_j h_j + \vec{u}(\vec{x_j}^{+}, \tau_j) \\ \vec{x}^{+}_{j+1} = \vec{x}^{+}_{j} + \beta_j \Delta t \cdot h_{j+1} \\ \tau_{j+1} = \tau_1 + \gamma_j \Delta t \end{cases} \tag{3.52}$$

As was also described in 3.3.4 in the set of equations (3.52) h is an auxiliary variable initially valued with 0 and the subscript j is such that if is equal to 1 refers to the values in the beginning of the time step if it is 4 is the final value obtained after the time integration (each sub-step causes an increment of j).

The coefficients α_j, β_j and γ_j have the values pointed out in equations (3.30), (3.31) and (3.32).

3.4.3 Interpolation Schemes

To solve numerically equation (3.50), it is imperative to be able to compute the velocity in any point of the box. To do so, 6 interpolation schemes were implemented: Spectral, Backward, Linear, Quadratic, Cubic and Taylor Series 13 Point (TS13).

It is important to notice that, even though there are 6 types of interpolation, they can be grouped in three different categories: The ones using Fourier series (Spectral), the ones that use Lagrangian polynomials (Backward, Linear, Quadratic and Cubic) and the ones using Taylor Series expansion (TS13).

It is important to state that due to chaotic nature of turbulence, a slightly difference in the interpolated velocity, comparing with the real velocity, results in a completely different trajectory. Even though, interestingly, Lagrangian structure function of second order is just lightly affected [68].

Even though, velocity interpolation errors must be minimized, this imposition has a computational cost. Thus, an evaluation of the pros and cons will be discussed in section 4.2, to then make the final choice of what interpolation scheme will be used in the simulations.

Before proceeding to the description of the interpolation schemes, it must be highlighted that these schemes can also be used to interpolate any other variable known in the grid nodes.

Spectral (Exact)

As explained in section, 3.3.2, any general quantity (ψ) of the fluid can be written as (using equations (3.16) and (3.12)):

$$\psi(x,y,z,t) = \sum_{l=-N_x/2+1}^{N_x/2-1} \sum_{m=-N_y/2+1}^{N_y/2-1} \sum_{n=-N_z/2+1}^{N_z/2-1} \hat{\psi}(k_l,k_m,k_n,t) e^{i(l\cdot\frac{L_x}{2\pi}x + m\cdot\frac{L_y}{2\pi}y + n\cdot\frac{L_Z}{2\pi}z)}. \tag{3.53}$$

Notice that if one does a inverse fast Fourier transform, one immediately obtains the exact values of the function in the grid points. Thus, to compute the exact value of the function ψ in a certain point, what is needed is to know the Fourier transform for the staggered grid that contains that point.

To relate the Fourier transform for different grids lets start by assuming a dislocation of x',y' and z', in a practical matter, this dislocations in absolute value will always be smaller than L_X/N_X, L_Y/N_Y and L_Z/N_Z, respectively, because a grid dislocated by x' or $x' + L_X/N_X$ will contain the same points (because the boundary conditions are periodic). Using equation (3.53), for the displacement assumed, the function ψ must be:

$$\begin{aligned} &\psi(x+x', y+y', z+z', t) = \\ &= \sum_{l=-N_x/2+1}^{N_x/2-1} \sum_{m=-N_y/2+1}^{N_y/2-1} \sum_{n=-N_z/2+1}^{N_z/2-1} \hat{\psi}(k_l,k_m,k_n,t) e^{i(l\cdot\frac{L_x}{2\pi}(x+x') + m\cdot\frac{L_y}{2\pi}(y+y') + n\cdot\frac{L_z}{2\pi}(z+z'))}. \end{aligned} \tag{3.54}$$

Doing some algebraic operation results in:

$$\begin{aligned} &\psi(x+x', y+y', z+z', t) = \\ &= \sum_{l=-N_x/2+1}^{N_x/2-1} \sum_{m=-N_y/2+1}^{N_y/2-1} \sum_{n=-N_z/2+1}^{N_z/2-1} \{\hat{\psi}(k_l,k_m,k_n,t) e^{i(l\cdot\frac{L_x}{2\pi}(x') + m\cdot\frac{L_y}{2\pi}(y') + n\cdot\frac{L_Z}{2\pi}(z'))}\} e^{i(l\cdot\frac{L_x}{2\pi}(x) + m\cdot\frac{L_y}{2\pi}(y) + n\cdot\frac{L_z}{2\pi}(z))}. \end{aligned} \tag{3.55}$$

Comparing equation (3.55), with the definition of Fourier series , (3.11), it is clear that the Fourier transform for a staggered grid is simply given by:

$$\hat{\psi}(k_l,k_m,k_n,t) e^{i(l\cdot\frac{L_x}{2\pi}(x') + m\cdot\frac{L_y}{2\pi}(y') + n\cdot\frac{L_z}{2\pi}(z'))}, \tag{3.56}$$

where $\hat{\psi}(k_l,k_m,k_n,t)$ is the Fourier transform in the unstaggered grid. Therefore, to compute the exact value of a certain quantity in a certain point, the following procedure is made:

- First, compute the displacement x',y' and z', to the closest point.
- Second, use equation (3.56) to compute the Fourier transform in the staggered grid.
- Finally use an Inverse FFT to obtain the exact value in the real space.

Even though this method is extremely accurate, it is also extremely expensive. As an example, in a simulation with one million particles for each time-step (considering three velocity components and three sub-steps) it would be required six million inverse FFTs, which is clearly unpractical. Due to this reason, this method will only be used for verification purposes.

Backward and Linear

First consider the interpolation cell used is represented in figure 3.2, where the nodal points are grid points (represented as spheres) and the point with coordinates (x,y,z) is inside the cell.

A general function $\psi(x, y, z)$, of a given fluid property, is known in each nodal points and it's value in the i-th node is ψ_i, in which i$\in$[1;8] (the distribution of the nodes by number is displayed in figure 3.2).

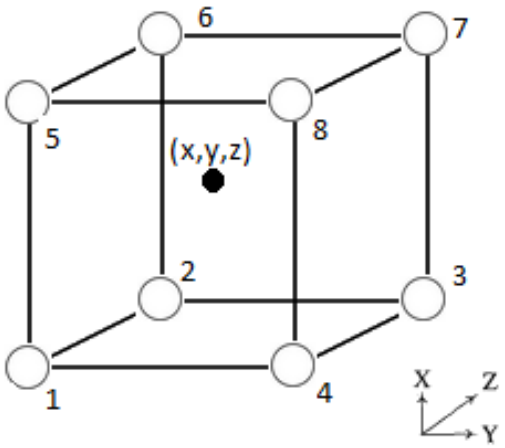

Figure 3.2: Sketch of a interpolation cell, and nodal points, used in backward and linear interpolation.

The backward interpolation is simply made by assuming that $\psi(x, y, z) = \psi_1$. This interpolation is, computationally, the cheapest that can be used, however it is a method with solely first order accuracy.

Regarding the linear interpolation, it lays on the approximation that the general function ψ varies linearly in each coordinate. Therefore, in terms of nodal values the function ψ can be approximated as:

$$\psi(x, y, z) = \sum_{i=1}^{8} a_i \psi_i \ . \tag{3.57}$$

Where the coefficients a_i are (considering a referential with its origin in node number 1 and using the adimensional coordinates $x' = \frac{x}{\Delta x}$,$y' = \frac{y}{\Delta y}$ and $z' = \frac{z}{\Delta z}$):

$$a_1 = (1 - x')(1 - y')(1 - z'),$$

$$a_2 = (1 - x')(1 - y')(z'),$$

$$a_3 = (1 - x')(y')(z'),$$

$$a_4 = (1 - x')(y')(1 - z'),$$

$$a_5 = (x')(1-y')(1-z'),$$

$$a_6 = (x')(1-y')(z'),$$

$$a_7 = (x')(y')(z'),$$

$$a_8 = (x')(y')(1-z').$$

This interpolation scheme is second order accurate, however it suppresses all non linear variations on scales smaller than the grid spacing. Considering the nature of turbulence with highly non linear spatial variations this method is expected to generate considerable interpolation errors. However, in many investigations, this is the interpolation used due to it's low computational cost (e.g. [46], [52], [57]).

Lagrangian polynomial interpolation

The major problem of the previous interpolation scheme is that due to the existence of few nodal points, the order of accuracy achieved is low. There are two possible solutions to increase the number of nodal points, first, create new ones using staggered grids (used in the TS13 interpolation) and the other one, using a larger interpolation cell that contains more grid points (the one used in these interpolation schemes).

First lets start by defining the size of the interpolation cell based on the order of the polynomial that is desired. Generally, in a function with three independent variables, to obtain a Lagrangian interpolative polynomial of n-th order in each direction it is required $(n+1)^3$ points, thus, in the present case, the interpolation cell will be a cube with linear dimension equal to $n\Delta x$. Also, the vertices of the cube will be nodal points. Finally, the last parameter to completely describes the interpolation cell in space, its centroid position, which obviously is chosen to have the smallest distance to the position $P(x,y,z)$ where the quantity ψ will be evaluated (note that the last statement does not mean that the centroid is coincident with the point P because the vertices of the cube must be nodal points).

Before presenting the equations of the interpolation polynomials it is important to state that the reference node, denoted by (i,j,k), satisfies the following conditions:

- When n is even, it is the closest nodal point to P (x,y,z), therefore the nodal point coincident with the interpolation cell centroid.

- When n is odd, it is the closest nodal point to P (x,y,z) of all the nodal points with smaller coordinates, i.e., the closest point that also verifies $x_{(i,j,k)} \leq x$, $y_{(i,j,k)} \leq y$ and $z_{(i,j,k)} \leq z$

To better understand the definition of the interpolation cell and its reference node, a 2D example is given in figure 3.3.

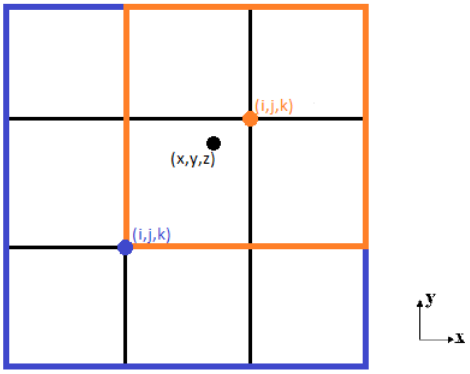

Figure 3.3: Example of an interpolation cell, for the same point considering quadratic (Orange cell) and cubic (Blue cell) Lagrangian polynomials. Even though the interpolation schemes are applied for 3D cells, the figure shows 2D cells for better visualization and understanding.

The subscript (i, j, k) is used to make reference to a quantity evaluated in the nodal point (i,j,k). The position of the nodal points are related by:

$$\begin{cases} x_{(i+i',j+j',k+k')} = x_{(i,j,k)} + i'\Delta x \\ y_{(i+i',j+j',k+k')} = y_{(i,j,k)} + j'\Delta y \\ z_{(i+i',j+j',k+k')} = z_{(i,j,k)} + k'\Delta z \end{cases} \tag{3.58}$$

Finally using the definition of Lagrangian polynomials results that, for n even (using $(i, j, k) = (0, 0, 0)$ in the reference node):

$$\psi(x,y,z) = \sum_{i=-\frac{n}{2}}^{\frac{n}{2}} \sum_{j=-\frac{n}{2}}^{\frac{n}{2}} \sum_{k=-\frac{n}{2}}^{\frac{n}{2}} \{ \psi_{(i,j,k)} \prod_{\substack{-\frac{n}{2}\leq i'\leq \frac{n}{2} \\ i'\neq i}} \frac{(x - x_{(i',j',k')})}{(x_{(i,j,k)} - x_{(i',j',k')})} \prod_{\substack{-\frac{n}{2}\leq j'\leq \frac{n}{2} \\ j'\neq j}} \frac{(y - y_{(i',j',k')})}{(y_{(i,j,k)} - y_{(i',j',k')})} \prod_{\substack{-\frac{n}{2}\leq k'\leq \frac{n}{2} \\ k'\neq k}} \frac{(z - z_{(i',j',k')})}{(z_{(i,j,k)} - z_{(i',j',k')})} \}. \tag{3.59}$$

For n odd the function is given as:

$$\psi(x,y,z) = \sum_{i=-\frac{n-1}{2}}^{\frac{n+1}{2}} \sum_{j=-\frac{n-1}{2}}^{\frac{n+1}{2}} \sum_{k=-\frac{n-1}{2}}^{\frac{n+1}{2}} \{ \psi_{(i,j,k)} \prod_{\substack{-\frac{n}{2}< i'\leq \frac{n+1}{2} \\ i'\neq i}} \frac{(x - x_{(i',j',k')})}{(x_{(i,j,k)} - x_{(i',j',k')})} \prod_{\substack{-\frac{n}{2}< j'\leq \frac{n+1}{2} \\ j'\neq j}} \frac{(y - y_{(i',j',k')})}{(y_{(i,j,k)} - y_{(i',j',k')})} \prod_{\substack{-\frac{n}{2}< k'\leq \frac{n+1}{2} \\ k'\neq k}} \frac{(z - z_{(i',j',k')})}{(z_{(i,j,k)} - z_{(i',j',k')})} \}. \tag{3.60}$$

The Lagrangian interpolation polynomials implemented were the quadratic one ($n = 2$) and the Cubic one ($n = 3$). The major advantage of this two interpolation schemes is that they need few computational

resources and have third and fourth order of accuracy, respectively. Note that the linear interpolation is also a specific case for n=2.

TS13

An important aspect to achieve lower interpolation errors is the use of better resolution, i.e., the use of more nodes per cell. Based on this, Yeung and Pope [69], designed a method based on Taylor expansion series, in which, to improve spatial resolution were added nodes in centre cells. The sketch of the interpolation cell is presented in figure 3.4.

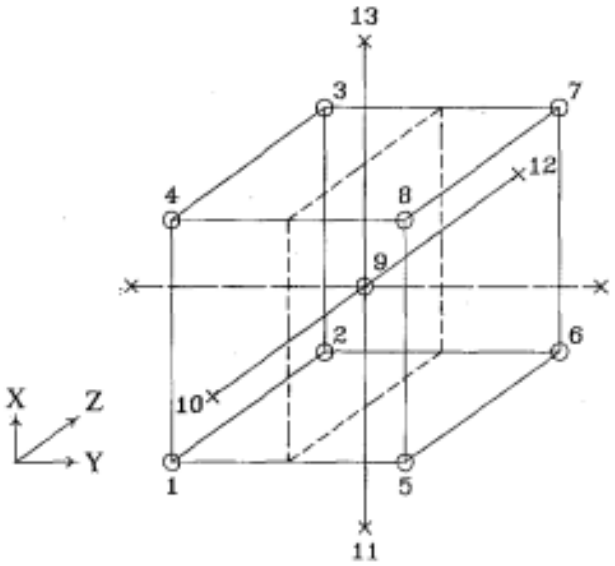

Figure 3.4: Sketch of a interpolation cell and the nodal points used in the TS13 interpolation. Source [69].

Notice that to compute the node values of the centre cells the spectral interpolation method, described previously, is used.

This method is design to achieve a fourth-order accuracy, therefore, the Taylor expansion must contain all terms with derivatives equal or lower than three. Considering the centre of the interpolation cell the origin of the referential and doing the expansion in Taylor series, of a general function ψ, results in (Einstein notation):

$$\psi(x,y,z) \approx \psi(0,0,0) + x_i \frac{\partial \psi}{\partial x_i}(0,0,0) + \frac{1}{2!} x_i x_j \frac{\partial^2 \psi}{\partial x_i \partial x_j}(0,0,0) + \frac{1}{3!} x_i x_j x_k \frac{\partial^3 \psi}{\partial x_i \partial x_j \partial x_k}(0,0,0). \quad (3.61)$$

All derivatives must be computed using numerical methods. To ensure third order of accuracy of the interpolation scheme, all finite derivatives used are second order. However, notice that in the y direction the centre cell nodes are not available, therefore to compute the first derivative of the function in the direction y, one uses:

$$\frac{\partial \psi}{\partial y}(0,0,0) \approx \frac{(\psi_5+\psi_6+\psi_7+\psi_8)-(\psi_1+\psi_2+\psi_3+\psi_4)}{4\Delta y}. \tag{3.62}$$

The previous formula uses linear interpolation to compute the value of the function ψ in the mid faces of the interpolation cell perpendicular to the y direction. This term adds an error of second order to the interpolation scheme and thus, a degradation of the interpolation scheme quality occurs, resulting that the final scheme is only third order accurate.

After replacing the finite differences in equation 3.61, the final result can be written in terms of the node values, hence:

$$\psi(x,y,z) = \sum_{i=1}^{13} a_i \psi_i \tag{3.63}$$

Where the interpolation weights are (using the adimensional coordinates $x' = \frac{x}{\Delta x}$,$y' = \frac{y}{\Delta y}$ and $z' = \frac{z}{\Delta z}$):

$$a_1 = \frac{-x'-y'-z'+2y'^2+2x'y'+2x'z'+2y'z'-4x'y'z'}{4}$$

$$a_2 = \frac{-x'-y'+z'+2y'^2+2x'y'-2x'z'-2y'z'+4x'y'z'}{4}$$

$$a_3 = \frac{x'-y'+z'+2y'^2-2x'y'+2x'z'-2y'z'-4x'y'z'}{4}$$

$$a_4 = \frac{x'-y'-z'+2y'^2-2x'y'-2x'z'+2y'z'+4x'y'z'}{4}$$

$$a_5 = \frac{-x'+y'-z'+2y'^2-2x'y'+2x'z'-2y'z'+4x'y'z'}{4}$$

$$a_6 = \frac{-x'+y'+z'+2y'^2-2x'y'-2x'z'+2y'z'-4x'y'z'}{4}$$

$$a_7 = \frac{x'+y'+z'+2y'^2+2x'y'+2x'z'+2y'z'+4x'y'z'}{4}$$

$$a_8 = \frac{x'+y'-z'+2y'^2+2x'y'-2x'z'-2y'z'-4x'y'z'}{4}$$

$$a_9 = 1-x'^2-2y'^2-z'^2$$

$$a_{10} = \frac{z'^2-y'^2}{2}$$

$$a_{11} = \frac{x'^2-y'^2}{2}$$

$$a_{12} = a_{10}$$

$$a_{13} = a_{11}$$

3.5 Code Development

This section briefly describes some code implementation aspects, developed in the present work, which have key importance in the code performance.

3.5.1 Particle transfer

As stated in section 3.3.7, the domain is decomposed into sub-domains and each core processor handles the computations regarding its specific 2D pencil. However, particles move freely in the box and thus, in any sub-step a particle can exit a processor domain to enter into another one. As explained in section 3.3.7, **the communications are very expensive and should be avoided to ensure the scalability of the code.**

Therefore, in the present work, the particle transfers between processors are only made at the end of each time step, thus the communication time is reduced by a third. Even though particles change domain (i.e. processor and 2D-pencil) during a sub-step, there is no need to do particle data transfers among processors in each sub-step, the way this property is achieved will be detailed in section 3.5.2.

Also, in a synchronous communication the processors will stop until all of them are ready for the data transfer. Therefore, sending particles one by one is computationally extremely expensive so, the particle transfer routine must have the lowest communication requests as possible. Keeping this in mind, the solution found in the present work consists in creating an auxiliary matrix (M_{aux}) with dimensions $5\text{x}T_N$ and fill it with info of the particles that must be transferred. The number of columns of the matrix, T_N, is such that will be always grater than the number of all transfers between domains in a time step (to prevent data leakage). The number of lines is 5 so that each column has the information about the particle coordinates (3), the particle ID (1) (a variable that greatly simplifies the post-processing tools making it possible to reconstruct the particle trajectory and properties variations along each one) and the ID of the processor that contains the domain/2D-pencil in which the particle currently is (1) (The processor that emanate the particle, computes the ID of the processor in which the tracer should be, if it is equal to his own ID, there is no need for transfer otherwise there is. Since the new processor ID has already been computed it saves computational time sending this information instead of making all processors recompute it to know whether or not the particle is in its domain). The additional memory cost of this approach is, using an overestimation, over 10 MegaBytes consequently, in a processor with 4 GibaBytes of memory RAM the increase in RAM is negligible.

Before filling matrix M_{aux} and make the particle transfer all processors must compute how many particles exited its domain. After that, all of them fill an auxiliary array, A_{aux} (that has a dimension equal to the number of processors), with zeros except at the entry number equal to their own processor ID, in which they stored the number of particles exiting their domain.

Then, the first synchronous communication is made to assemble all A_{aux} of all processors into a new B_{aux} array . Notice that B_{aux} is an array that for each entry have the number of particles exiting the processor with the ID equal to the entry number. If T_N is smaller than the sum of all entries of the array (total number of transfers), it must be updated, but, this rarely occurred in the present simulations.

After knowing B_{aux} it is possible to fill the matrix M_{aux}. To do so, each processor sums the number of particles that have exited the processors with an ID number lower than its own and fills that number of columns with zeros. After that it fills the next columns with the info of the particles that are exiting his domain. The remaining columns are also set to zero.

To illustrate this procedure a simple example is here given. Consider a simulation with 2 processors, with $N_T = 6$ and in a certain time-step $B_{aux} = [2 \quad 3]$ the M_{aux} matrix will be filled in the following way: (Since each processor has its own M_{aux} a superscript will be used to indicate to which one it is concerning. Also, an entry with x means that, that entry has some information/number different than 0)

$$[M^1_{aux}] = \begin{bmatrix} x & x & 0 & 0 & 0 & 0 \\ x & x & 0 & 0 & 0 & 0 \\ x & x & 0 & 0 & 0 & 0 \\ x & x & 0 & 0 & 0 & 0 \\ x & x & 0 & 0 & 0 & 0 \end{bmatrix} \qquad [M^2_{aux}] = \begin{bmatrix} 0 & 0 & x & x & x & 0 \\ 0 & 0 & x & x & x & 0 \\ 0 & 0 & x & x & x & 0 \\ 0 & 0 & x & x & x & 0 \\ 0 & 0 & x & x & x & 0 \end{bmatrix}$$

Following this step, a second synchronous communication is made to sum all M_{aux} of all processors. Notice that the final result (N_{aux}) is a matrix with all the particles that are changing domain. After that, each processor scroll along the fifth line of N_{aux} and whenever the value found is equal to his own ID, it stores the particle. **Notice that the choice of the matrix dimensions as 5xN_T instead of N_Tx5 was not random, actually it was made concerning this step because it is more efficient to scroll in a matrix line than in a matrix column.**

Finally, for writing the particle states it is also necessary that all processors know how many particles are in each processor. The way to do this is similar to the one described previously regarding the exit number particles. Meaning that another synchronous communication is added.

In conclusion, the method implemented has only 3 synchronous communications and an unimportant setback due to a small increment in memory usage. It is relevant to state that this routine was of crucial importance to ensure the scalability of the code. A diagram of this routine is shown in figure 3.5.

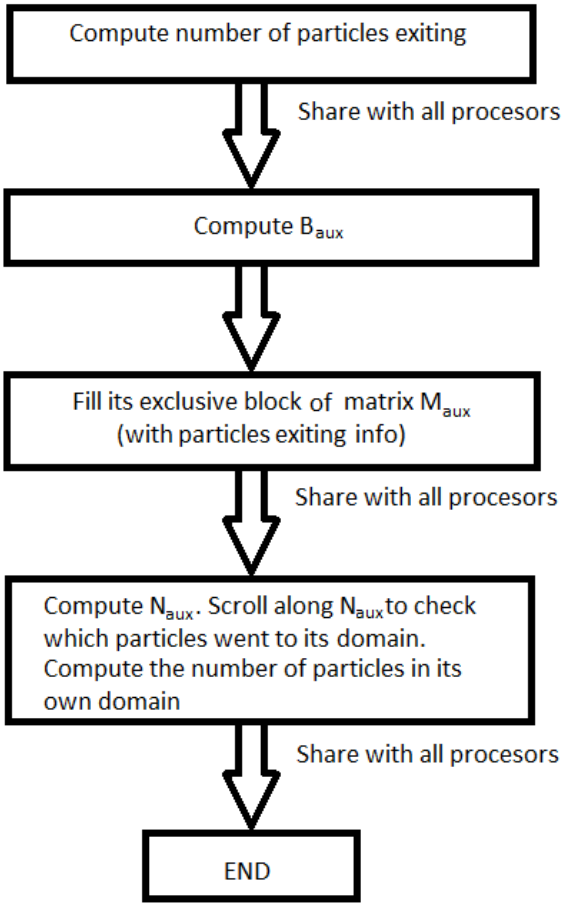

Figure 3.5: Diagram of the particle transfer routine.

3.5.2 Particle Velocity Interpolation

Regarding the velocity interpolation, the methods implemented have already been discussed in section 3.4.3 but, two very important complementing aspects will be presented here.

First, as explained before, the cubic interpolation requires the usage of 4 cell nodes in each direction (x,y and z), however, suppose that a particle is so close to the boundary of two domains that in order to complete the interpolation, it is required to use the velocity field from points that are out of the processor domain. This situation could be resolve by an information trading between two, or three or even four processors. However, as already explained, the number of communications must be the smallest possible, therefore the solution to this, rests in the use of Halo cells, i.e., each processors during the interpolation also has the information of its neighbour points. The halo can have different levels, the level one case, for a 2D domain decomposition using a 2x2 MPI processes, is illustrated in figure 3.6.

The 2DECOMP library has halo-cell support routines which are easy and efficient, and that have been used for this purpose.

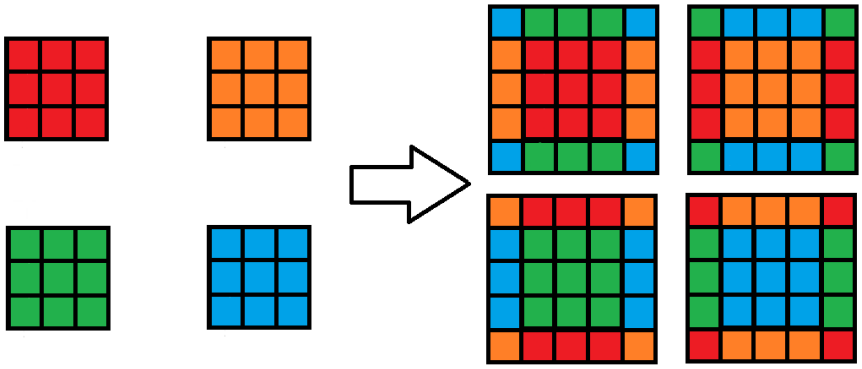

Figure 3.6: Illustration of level 1 halo cells for a 2D domain decomposition using a 2x2 MPI processes.

Finally it is important to state that, due to the stability conditions (3.33) **and** (3.35)**, a particle can never cross an entire cell. Knowing that the halo level can be chosen in such way that even if during a sub-step a particle change processor domain the interpolation will still be feasible. As a result, it is possible to transfer particles only in the end of time step instead of in every sub-step and consequently reduced the synchronous communication by a third.**

3.5.3 Particle states writing and Post-Processing

The particle states writing, in order to be time efficient, is made by blocks, i.e., each processor has an exclusive portion of the output file and writes the states of its particles. For this purpose, as discussed in section 3.5.1 every processor knows the number of particles that are in each processor (this is the reason why the third and last synchronous communication, in the particle transfer routine, is made). With that input, for a given number of particle fields to be stored (e.g. x, y, z, u, v, w), it is possible to compute the number of bytes that each processor will occupy in the file (number of particles times the number of bytes needed to store the number of fields given). To compute the specific location where a processor will start writing it is only required to sum the number of bytes that each processor, with an ID number lower than its own, will use.

Notice that the particles are not written always in the same sequence. This is why it is so important to have an extra field with the particle ID. Only that field enables the reproduction of the particle trajectories and analysis of property variations along the same ones, during the Post-Processing execution.

Finally, another important feature is that during the Post-Processing realization, every time-step is considered as the launch of another simulation. It is obvious that thus, each new simulation will have a running time smaller than the previous one. However, the number of samples used to compute statistics regarding property variations in a time interval, pertaining into the inertial range of time, will be the number of particles multiplied by a factor of the order of $\sim 10^4$. Therefore the number of particles required to have a converged statistical results is tremendously reduced. These reduction also results in a critical reduction of computational time spent and in a massively decrease in memory usage.

Chapter 4

Verification and Validation

4.1 Verification

For verification purposes comparison with analytical solutions regarding an helical velocity field were carried out. Even though the helical velocity field it is not a solution of the Navier-Stokes equations it will be used because:

- It can be integrated analytically over time, and thus, it is possible to obtain exactly the trajectory of any particle in the flow. With this it is possible to compute the error of the time integration scheme.
- It is periodic in space, meaning that the interpolations that require a large interpolation cell, in such way that the use of halo cell, as described in section 3.5.2, can also be applied.
- By knowing the exact velocity in all the domain it is possible to investigate the behaviour of the mean absolute interpolation error and check if the order of accuracy of each method is the expected.

The velocity field used for verification is also the one used for the same purposes in [69], is given by (with r defined as $r = \sqrt{(x-\pi)^2 + (y-\pi)^2}$):

$$\begin{cases} u = -(y-\pi)(1 - 3\frac{r}{\pi}^2 + 3\frac{r}{\pi}^4 - \frac{r}{\pi}^6) & \text{if } r \leq \pi \\ u = 0 & \text{if} r > \pi \\ v = (x-\pi)(1 - 3\frac{r}{\pi}^2 + 3\frac{r}{\pi}^4 - \frac{r}{\pi}^6) & \text{if } r \leq \pi \\ v = 0 & \text{if } r > \pi \\ w = 0.5 \end{cases} \quad (m/s) \tag{4.1}$$

To verify that the Runge-Kutta third order scheme was well implemented, one needs to know exactly the final particle position, given an initial one, so that the integration errors can be computed. Suppose we have a particle with initial conditions $x = x_0^+$, $y = y_0^+$ and $z = z_0^+$, changing the coordinate system to a cylindrical one with origin in the point $(\pi, \pi, 0)$, in the new coordinate system the velocity field is given by:

$$\begin{cases} u_r = 0 \\ u_\theta = r \cdot (1 - 3\frac{r}{\pi}^2 + 3\frac{r}{\pi}^4 - \frac{r}{\pi}^6) & \text{if } r \leq \pi \\ u_\theta = 0 & \text{if } r > \pi \\ u_z = 0.5 \end{cases} \quad (m/s) \tag{4.2}$$

and the initial conditions are:

$$\begin{cases} r_0^+ = \sqrt{(x_0^+ - \pi)^2 + (y_0^+ - \pi)^2} \\ \theta_0^+ : \{sin(\theta_0^+) = \frac{y_0^+}{r_0^+} \wedge \cos(\theta_0^+) = \frac{x_0^+}{r_0^+}\} \\ z_0^+ = z_0^+ \end{cases} \tag{4.3}$$

Integrating the velocity field over an interval of time T, one obtains the exact position that, in the cylindrical coordinate system and for the initial conditions specified in 4.3 is:

$$\begin{cases} r^+(T) = r_0^+ \quad (m) \\ \theta^+(T) = \theta_0^+ + (1 - 3\frac{r_0^+}{\pi}^2 + 3\frac{r_0^+}{\pi}^4 - \frac{r_0^+}{\pi}^6)T & \text{if } r_0^+ \leq \pi \\ \theta^+(T) = \theta_0^+ & \text{if } r_0^+ > \pi \\ z^+(T) = z_0^+ + 0.5T \quad (m) \end{cases} \tag{4.4}$$

4.1.1 Low storage Runge-Kutta third order verification

The Runge-Kutta third order scheme is third order accuracy, meaning that the absolute errors of time integration will decrease asymptotically with $(\Delta t)^3$. To evaluate if this condition is verified different simulations with different Δt were made. Different total integration times were also used (T=10 s and T=100 s).

In those simulations the velocity is computed exactly with equation 4.1, instead of using interpolation methods, to ensure that velocity interpolation errors do not contaminate the analysis.

To compute the mean absolute error of the displacement in each direction, a sample with one million particles, randomly distributed in the domain, was used. However, the particle distribution was identical for all simulations.

Note that the velocity field is symmetric, i.e., $\frac{\partial}{\partial\theta}$ of every velocity component is zero, then, the mean absolute error for x and y displacements should be equal. Due to fact that the sample is finite, the two mean absolute displacement errors are not exactly equal. To increase the sample size (decrease the uncertainty in the result), the quantity that will be used to analyse the error dependence with the timestep is: $\epsilon_X = \overline{|x_i^+ - x_i^{exact}|}\frac{\delta_{ii}}{2}$ (i: 1,2).

Also, the difference between the two expected errors (x and y direction) will be used to quantify the uncertainty of the result. The parameter that will be used for this purpose is: $e = \frac{|\overline{|x^+ - x^{exact}|} - \overline{|y^+ - y^{exact}|}|}{\overline{|x_i^+ - x_i^{exact}|}\delta_{ii}}$.

The error is expected to decrease with time, in a log-log scale, with a slope equal to 3. However, this behaviour is asymptotically, thereby, only the mean absolute errors regarding the two smallest Δt, will

be used to compute the observed slope.

The results obtained regarding these three quantities are listed in table 4.1. It can be seen that the relative uncertainty is really low, being smaller than 1%, therefore, the slopes obtained are not contaminated with errors due to the finite size of the sample. The slopes obtained are the expected ones for both curves thus, this scheme was well implemented. Also, this last observation could be realized by analysing figure 4.1, which was obtained using the data from table 4.1.

Finally, notice that w is constant, hence, the numerical integration of this quantity should be exact. However, due to precision limitations the mean absolute error regarding the z coordinate is, for every simulation of the order of $\sim 10^{-15}$.

Table 4.1: Absolute mean error values obtained using third order Runge-Kutta low-storage integration scheme for the helical field.

		$\overline{\lvert x_i^+ - x_i^{exact}\rvert}\frac{\delta_{ii}}{2}$	
		T=10 [s]	T=100 [s]
Δt [s]	0.1	1.701E-5	1.447E-3
	0.05	2.128E-6	1.832E-4
	0.025	2.652E-7	2.265E-5
	0.0125	3.324E-8	2.810E-6
	0.0625	4.118E-9	3.507E-7
Max(e) [%]		0.45	0.46
Slope		3.01	3.00

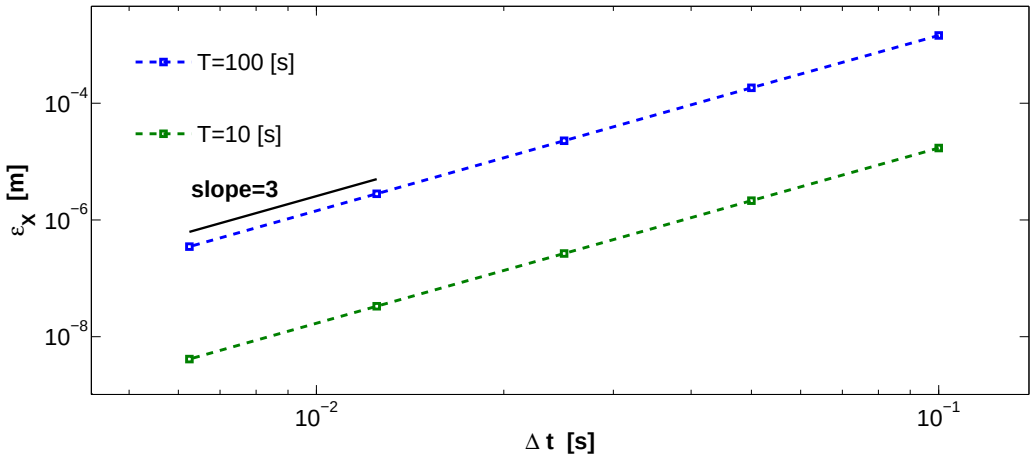

Figure 4.1: Absolute mean error values obtained using third order Runge-Kutta low-storage integration scheme as function of the time-step for an helical field.

4.1.2 Interpolation Schemes Verification

In section 3.4.3 it is mentioned that backward, linear, quadratic and cubic interpolations are first, second, third and fourth order accurate respectively. Also, the TS13 interpolation is expected to be third order accurate. To evaluate if each interpolation method were implemented correctly it will be checked if the slope of the mean absolute error as function of the mean grid size in a log-log plot is the expected one (slope=n-th order of accuracy).

To compute the mean absolute error of the velocity interpolation for each component (u, v, w), a sample with 20000 particles was used, randomly distributed in the domain. However, the particle distribution was identical for all simulations (each simulation has a different mean grid size).

As referred in the previous section, the velocity field is symmetric therefore, the mean absolute interpolation error for u and v should be equal. Due to fact that the sample size is finite, the two mean absolute interpolation errors are not exactly equal. To increase the sample size (decrease the uncertainty in the result), the quantity that will be used to analyse the error dependence with the time step is: $\epsilon_u = \overline{|u_i^+ - u_i^{exact}|}\frac{\delta_{ii}}{2}$ (i: 1,2).

Also, the difference between the two will be used to quantify the uncertainty of the result. The parameter that will be used for this purpose is: $e = \frac{|\overline{|u^+ - u^{exact}|} - \overline{|v^+ - v^{exact}|}|}{\overline{|u_i^+ - u_i^{exact}|}\delta_{ii}}$.

As explained, the slope behaviour is asymptotic thereby, only the mean absolute errors regarding the two grids with smallest $\sqrt{\Delta x \Delta y}$, will be used to compute the observed slope. Notice that the average linear grid size used is the geometric mean value of Δx and Δy. The grid size Δz is not used because the velocity field only depends on x and y.

The results obtained regarding these three quantities for each interpolation method are listed in table 4.2. It can be seen that, the relative uncertainty is really low, being smaller than 1% therefore, the slopes obtained are not contaminated with errors due to the finite size of the sample. The slopes obtained are the expected ones for every curve except for the cubic interpolation in which the relative error of the slope obtained is 1.5 %. However, this error is not meaningful because for the slope computed using the two grids with highest $\sqrt{\Delta x \Delta y}$ is just 3.89 thus, the slope is still increasing and it is possible that the asymptotic behaviour has not yet been reached. Therefore, one can conclude that all interpolation schemes were implemented correctly. A visual verification can be made by analysing figure 4.2, which was obtained using the data from table 4.2.

Finally w is constant hence, the numerical interpolation of this quantity should be exact for every interpolation methods. However, due to precision limitations the mean absolute interpolation error is for every simulations of the order of $\sim 10^{-17}$ except for backward interpolation in which, since there are no arithmetic operations, the values obtained for all simulations are identical to the exact value.

Table 4.2: Absolute mean error values obtained for different interpolation methods and different grid sizes for the helical field.

		$\overline{\lvert u_i - u_i^{exact} \rvert} \frac{\delta_{ii}}{2}$				
		Backward	Linear	Quadratic	Cubic	TS13
$\sqrt{\Delta x \Delta y}$ [m]	$\frac{2\pi}{16}$	5.045E-2	5.423E-3	1.711E-3	7.600E-4	6.930E-4
	$\frac{2\pi}{32}$	2.526E-2	1.370E-3	2.131E-4	5.112E-5	8.546E-5
	$\frac{2\pi}{64}$	1.277E-2	3.429E-4	2.687E-5	3.770E-6	1.062E-5
	$\frac{2\pi}{128}$	6.405E-3	8.603E-5	3.350E-6	2.555E-7	1.314E-6
	$\frac{2\pi}{256}$	3.184E-3	2.141E-5	4.190E-7	1.664E-8	1.633E-7
Max(e) [%]		0.11	0.46	0.39	0.48	0.40
Slope		1.01	2.01	3.00	3.94	3.01

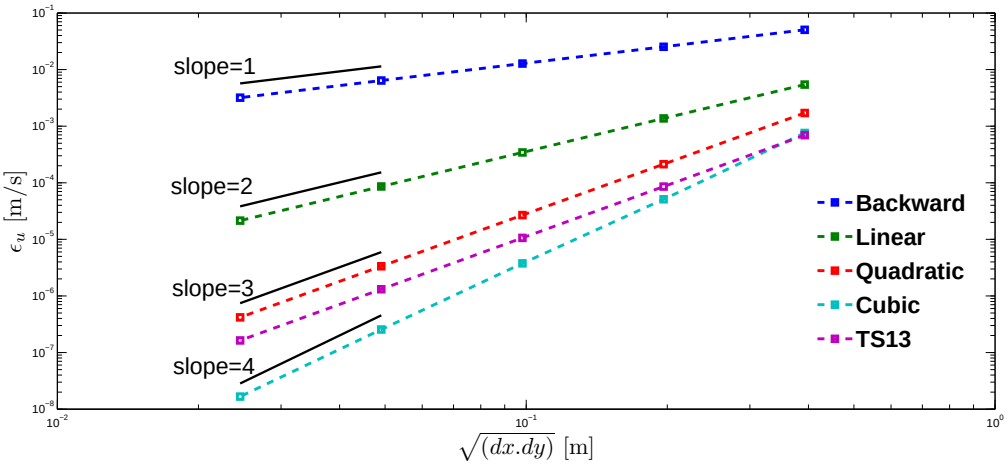

Figure 4.2: Absolute mean error values obtained using different interpolation methods as function of the grid size for the helical field.

4.1.3 Particle Transfer Verification

To ensure that the particle transfer, one of the most important feature in the code development, was implemented correctly and also to to give a graphical representation of the helical field, a simulation with a duration time of 12.5 seconds with time iterations of 0.0125 s was carried out. In this simulation 4 processors were used thus, the domain is divided in 4 sub-domains. In each processor 250 particles were randomly distributed and tracked, each position was recorded once in every four time iterations. The graphical result is shown in figure 4.3, where 1000 stream lines are represented to give an idea of the velocity field.

Notice that the radial velocity is 0, therefore, the projected trajectories in a plane perpendicular to z are simply points or concentric circles, this situation can be observed in figure 4.4.

Finally, the pencil decomposition is made in the x direction therefore, if each processor particles are

associated with a different color then when visualizing in a plane perpendicular to x four different regions must be distinguishable. Also, to ensure that the particle transfer is completed correctly only one color can be seen in each sub-domain. All of these conditions can be verified in figure 4.5, thereby, the particle transfer routine is checked to be working correctly.

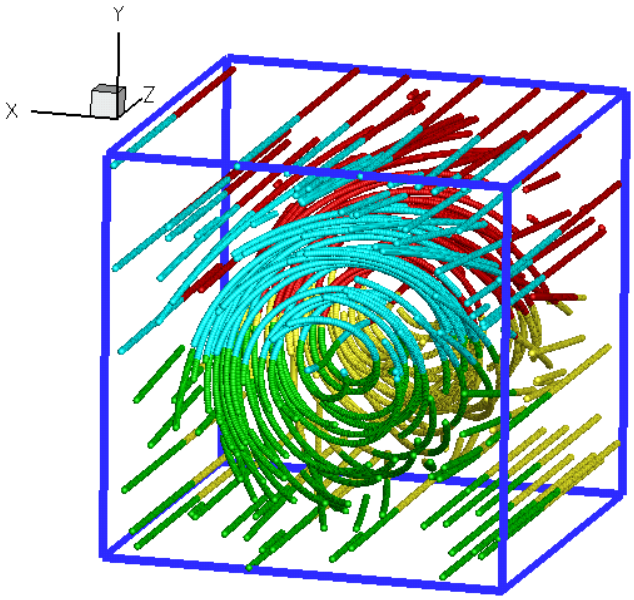

Figure 4.3: One thousand stream-lines in the helical flow. Each colour is associated with a different processor.

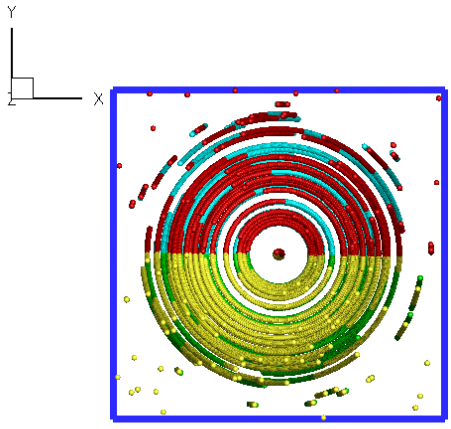

Figure 4.4: Helical flow projected in a plane perpendicular to z direction. Each colour is associated with a different processor.

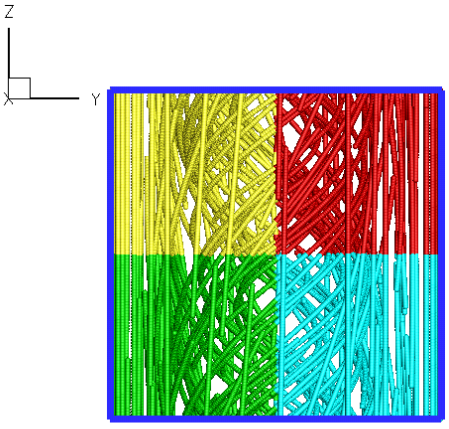

Figure 4.5: Helical flow projected in a plane perpendicular to x direction. Each colour is associated with a different processor.

4.2 Choice of Velocity Interpolation Scheme

In order to decide which interpolation scheme is going to be used in the DNS, two factors must be taken into account, first the time spent and second the mean absolute error.

Even though the spectral (exact) interpolation only has errors due to numerical truncation (i.e. floating point operations) limitations, it cannot be used due to its tremendous computational time cost. For example, the interpolation of the three velocity components for 20000 particles in a grid with 512^3 points using 32 processors, took approximately, 24 hours, thus an iteration time would required 72 hours of computational time. This is completely unusable for actual simulations.

Therefore, this interpolation scheme will just be used to evaluate the mean absolute error of each interpolation, that is considered be the absolute value of the difference between the velocity interpolated and the velocity computed with the spectral interpolation, since its the most precise.

To achieve the highest Reynolds number in a DNS simulation, without having aliasing problems and contemplating all flow scales, including the dissipative ones (to ensure that the solution is finely resolved), the parameter choice must be such that $k_{max} \cdot \eta \approx 1$, where $k_{max} = \frac{2}{3}(N/2 - 1)$.

Therefore, the first factor in choosing the interpolation scheme, the mean absolute error, will be evaluated for different simulations with different grid points but, always with $k_{max} \cdot \eta \approx 1$, since this condition will be imposed in every Newtonian simulation. In these simulations 20000 particles were used, also, since the flow is homogeneous and isotropic, to increase the samplesize, the mean absolute error is computed considering all three velocity components. The results are shown in figure 4.6.

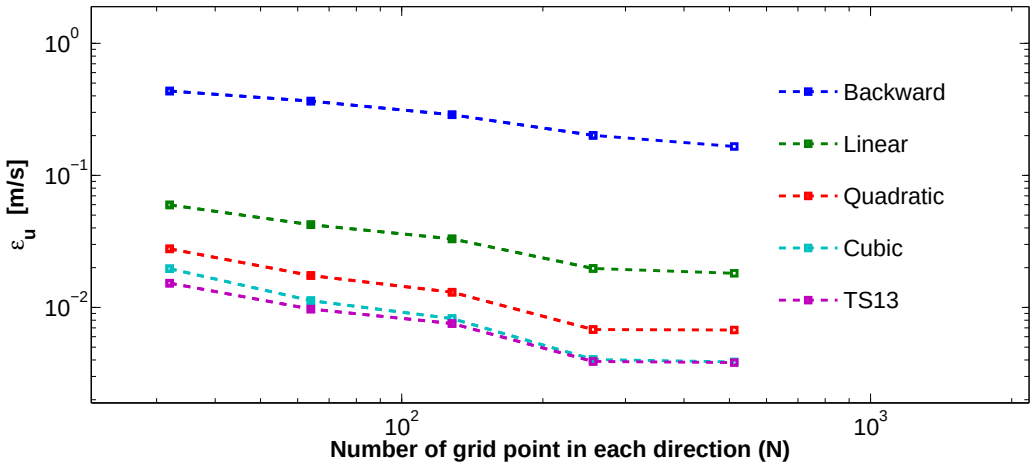

Figure 4.6: Mean absolute interpolation error in DNS simulations as function of number of grid points in each direction (N).

Analysing figure 4.6 it is possible to conclude that the backward interpolation is the one that presents the highest mean absolute error. This result was expected since, turbulence is characterized by high velocity fluctuations in space, therefore assuming that velocity is constant in a interpolation cell is a description without physical basis. Also, another important thing is observed: increasing the order of the interpolation polynomial decreases the mean absolute error, which was also expected. Finally, it is

possible to see that there is not a significant difference of the mean absolute error between TS13 and Cubic interpolations, thereby to choose which one is better the second factor must be considered.

To compute the computational time required to interpolate the three components of velocity per particle, it were performed simulations, using 32 processors, with 1000000 particles (a number of the same order that will be used in DNS simulations). Note that the number of processors will be different for different DNS simulations, however, the goal of the study of this quantity, for different interpolations, is to understand how the time required behaves with increasing the number of grid points, the exact value of time required per iteration is not significant. The results are shown in figure 4.7 and it is possible to perceive that the time required to interpolate the velocity increases with the order of the polynomial used (expected), also, the time required to do the TS13 interpolation increases more rapidly with the increase of number of grid points than any other interpolation, in such way that, for a grid with a number of points of 512^3, the time required is 10 times larger than the time required using the cubic interpolation, this occurrence is due the use of FFTs.

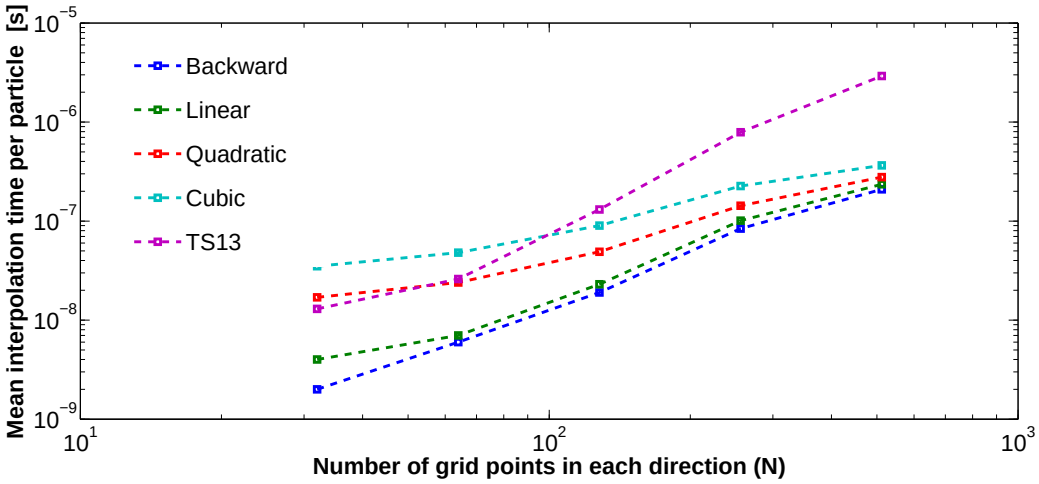

Figure 4.7: Mean interpolation time per particle in DNS simulations as function of number of grid points in each direction (N).

The two major factors have already been analysed, however, there is not an interpolation scheme that has the lowest mean absolute error and also the lowest required computational time, therefore, a compromise needs be made in order to choose the best interpolation for the DNS . Here, the criteria used is: The interpolation that will be used needs to be the one with smallest product between error and time spent ($\epsilon_u t$). Using this criteria it is given equal importance to both time and error. Note that if one wants to give more importance to having low error should use as criteria $\epsilon_u^a.t$, with a>1.

The value of $\epsilon_u t$ as function of number of grid points, for the different interpolation schemes is presented in figure 4.8. It can be seen that the interpolation that tendentiously have the lowest value of $\epsilon_u t$, for grids with high number of points, is the cubic interpolation. Therefore, it will be the one used in all DNS simulations.

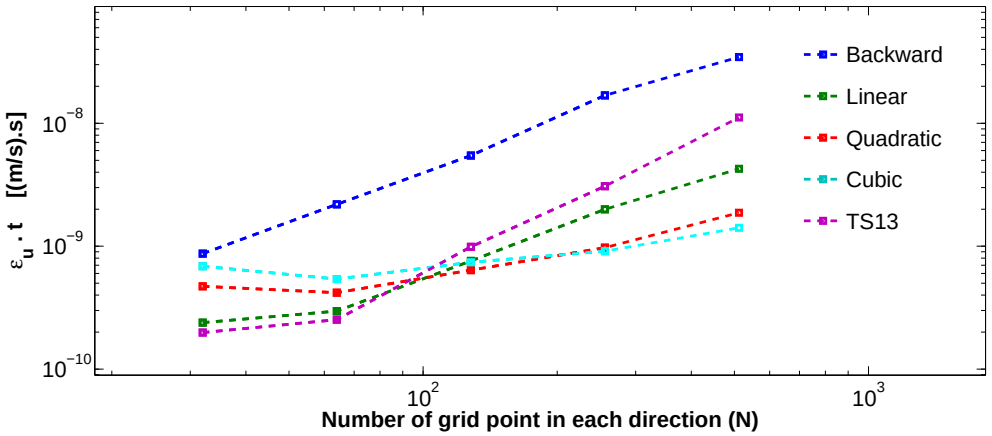

Figure 4.8: Product between mean absolute error and time spent per particle for each interpolation scheme.

4.3 Scalability Verification

One of the main objectives of the present thesis was to develop a scalable code, i.e., a code in which the computational time per time step is inversely proportional to the number of processors used. To verify if this property was achieved scaling tests were performed in four different supercomputers, which are described in table 4.3.

Table 4.3: Specifications of the supercomputers architecture, that were used in the scalabilty testing.

Supercomputer	Processor type	Memory per node	Cores per node	Peak Performance [Pflops]	Intercomunication technology
HAZELHEN	Intel Xeon CPU E5-2680 v3	128	24	7.42	Cray Aries
MARENOSTRUM III	SandyBridge-EP E5-2670	32	16	1.1	Infiniband FDR10
Supermuc (Phase 1)	SandyBridge-EP E5-2670	32	16	3.2	Infiniband FDR10
SUPERMUC (Phase 2)	Haswell Xeon E5-269 v3	64	28	3.58	Infiniband FDR14

For any graphical representation regarding the iteration time as function of number of processors, two different zones are expected to be observed. The first one, regarding a low number of processors, in which the time spent in communications is much smaller than the time spent on actual computation and thus, an increase of number of processors is followed by a decrease in the inverse proportion of the time spent per iteration (zone where scalability is observed). The second one, regarding a high number of processors, in which the communication time is similar, or higher, than the time spent on actual computations and an increase in the number of processors does not lead to a decrease in inverse proportion of the time spent per iteration and it can even increase the computational time. This is the

reason why it was stated, in section 3.5, that communications must be avoided at all cost to ensure a more wide scalable zone.

Before presenting the results obtained it is important to state that the code was developed over an already existing code, and the implementations made in the present work only added two new functionalities: the possibility of particle tracking and the possibility of simulating a flow with Hyper-viscosity. From the pre-existing version of the code, it was observed that it was scalable approximately until the number of processors was near the number of grid points in each direction. Thereby, since the scalability zone will certainly not be increased with the two new functionalities, the main objective is to keep it unaltered.

Since writing the particle status is not required in all iterations both situations, without and with writing, will be discussed. The results obtained for the first case are shown in figures 4.9, 4.10, 4.11 and 4.12.

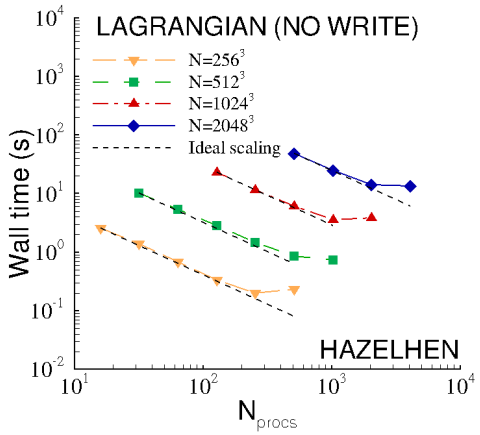

Figure 4.9: Hazelhen computational time of an iteration, without writing, as function of number of processors.

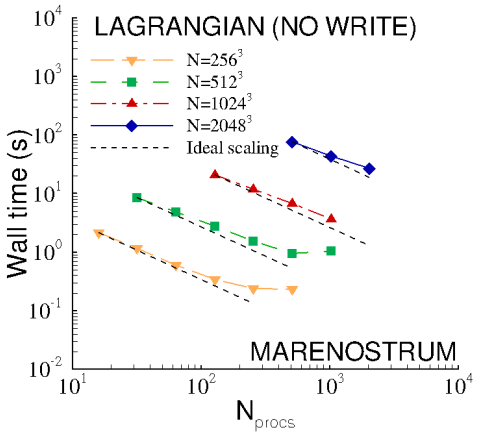

Figure 4.10: Marenostrum III computational time of an iteration, without writing, as function of number of processors.

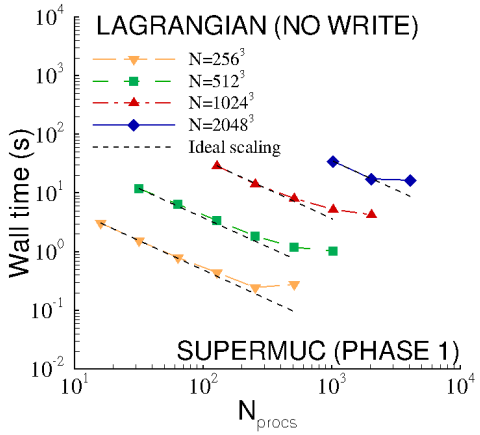

Figure 4.11: Supermuc (phase 1) computational time of an iteration, without writing, as function of number of processors.

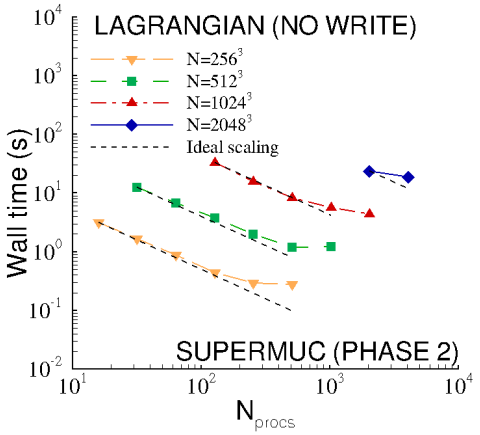

Figure 4.12: Supermuc (phase 2) computational time of an iteration, without writing, as function of number of processors.

Analysing figures 4.9 to 4.12 it is possible to see that the region where the code is scalable was unaltered, i.e., the code is scalable until the number of processors is similar to the number of grid points in each direction. Thus, the implementation of the particle tracking was excellent! Regarding the iterations with writing process, the results are presented in figures 4.13 to 4.16.

Unfortunately, even though many efforts were made, the scalable zone, for iterations with particle status writing, was reduced. The reason why this happened is obviously due to the input/output (IO) operations that require a considerable amount of time and also that time increases with number of cores used (more IO channels are required to send information with the same size). Even though MPI-IO interfaces were used to optimize the writing process however the scalable zone ended up shortened. However, the developed code with particle tracking remains higly scalable, i.e., the addition of particles did not significantly reduced the scalability of the code, as is often the case in other DNS codes.

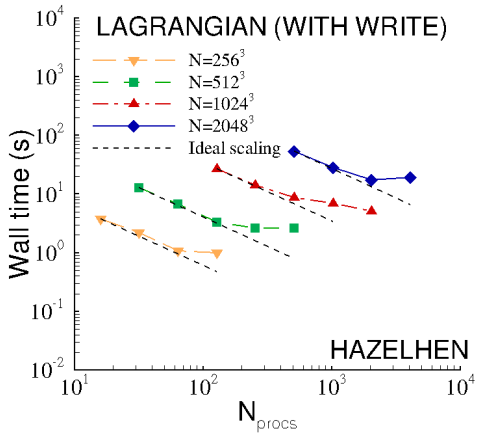

Figure 4.13: HazelHen computational time of an iteration, with writing, as function of number of processors.

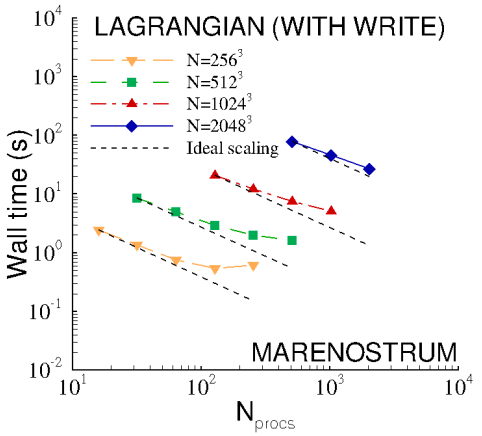

Figure 4.14: Marenostrum III computational time of an iteration, with writing, as function of number of processors.

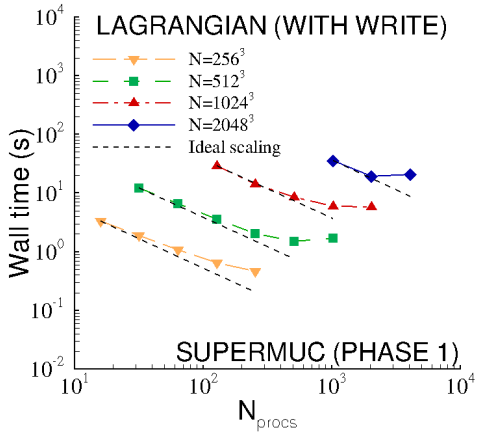

Figure 4.15: Supermuc (phase 1) computational time of an iteration, with writing, as function of number of processors.

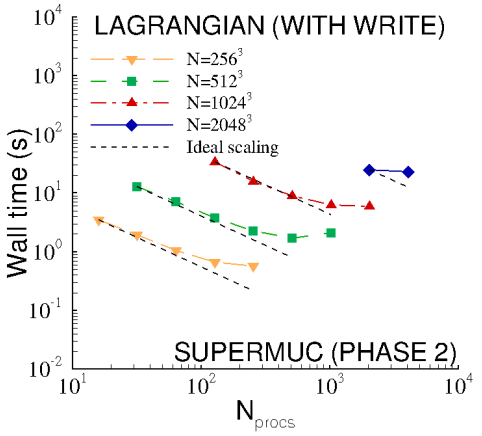

Figure 4.16: Supermuc (phase 2) computational time of an iteration, with writing, as function of number of processors.

4.4 Validation

4.4.1 Energy spectra

As explained before, only the particle tracking and the hyper-viscosity model were implemented in the course of this work, the rest of the code had already been implemented and validated. Therefore, the validation that will be made here, will only include the Lagrangian statistics and the Hyper-viscosity.

However, for comparison purposes, the energy spectra obtained from a simulation with N=1024, with the parameters listed in table 4.6, is shown in figure 4.17. First, notice that the predicted slope of -5/3, for the inertial range, is observed (discussed in chapter 2).

Second, comparing with the energy spectra obtained for a simulation with N=1024 and an hyper-viscosity coefficient equal to 8, plotted in figure 4.18, it is visible that the inertial range is more extended, as expected.

Regarding the energy spectra of the Hyper-viscous flow simulation, for the highest wavenumbers, unlike in the Newtonian spectra, visible a bottle neck effect is visible in the start of the dissipation range. However this behaviour is expected and it has already been discussed in the literature [27] [28] [29] [30].

Therefore, one concludes that the spectras obtained are, qualitatively, correct.

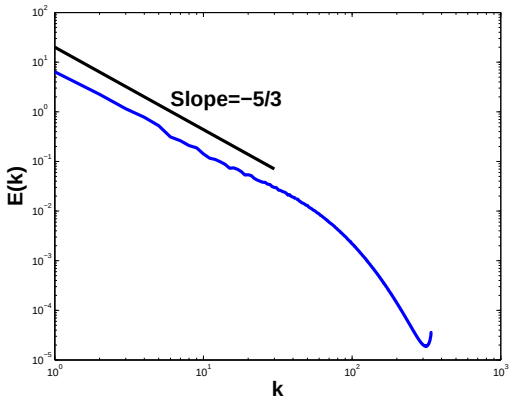

Figure 4.17: Energy spectra of Newtonian simulation with N=1024.

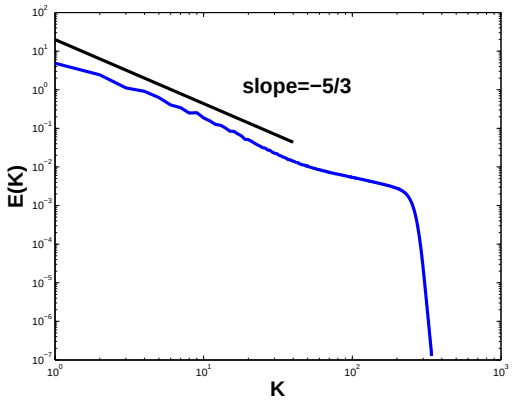

Figure 4.18: Energy spectra of Hyper-viscous simulation with N=1024.

4.4.2 Analysis of simulations non-physical parameters dependence

In this section the effect of some parameters in the Lagrangian second order structure function will be analysed. In theory, these function can only depend on the flow Reynolds number, therefore, one must evaluate if there exists any non-physical dependence that affects the final result.

Forcing

Let us start by analysing the forcing effect. It is obvious that the forcing is a non-physical feature, therefore, it must be evaluated if exists any result dependence with it.

It already had been analysed the differences between using a stochastic forcing and a deterministic one and the results shown that the differences are small, meaning that forcing has small effects in the statistics [70].

However a simple analysis was also made in the present work to understand the effect of the forcing. The analysis consisted in evaluating the effect of using different forcing peaks. For this purpose, three simulations were made, with approximately the same Reynolds (so that the peak force is the only difference). The simulations parameters are presented in table 4.4, and the second order structure function is, for the three simulations, shown in figure 4.19. It is important to state that in all simulations the width forcing was 2, and the number of particles used to compute the statistics was 500000.

Table 4.4: Simulations parameters of the three simulations used to evaluate the forcing effect

N	32	64	128
Peak force (k_f)	2	4	6
Re_λ	25.76	24.80	26.52
$k_{max}.\eta$	1.14	1.07	1.26
ν	0.11	0.04	0.0195
$\overline{\epsilon}$	10.49	6.076	4.502
$\frac{T_L}{\tau_\eta}$	3.97	3.46	3.80

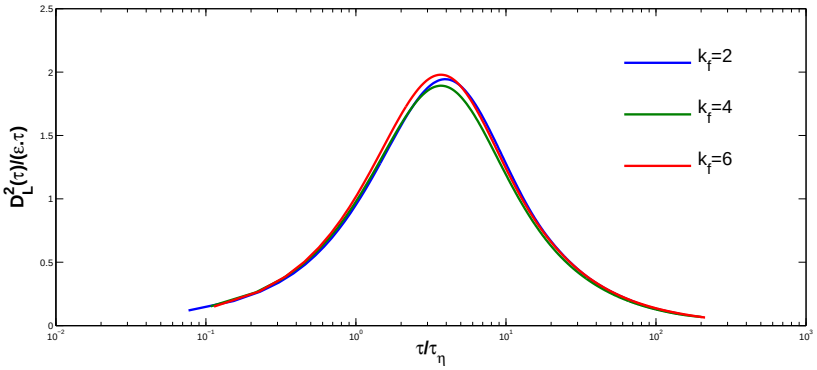

Figure 4.19: Lagrangian second order structure function as function of the forcing peak.

Based on the simulations results shown in figure 4.19 it is possible to observe some small differences, however this differences are justifiable with the fact that the Reynolds number is not equal for the three simulations and also, with the fact that the simulations are not completely statistically stationary, i.e., oscillations of the mean dissipation rate and also of other properties exist. **Therefore, one concludes that the forcing peak does not affect the second order structure function. Thereby in all the simulations that will be performed, the peak forcing will always be in the second wave number, to obtain higher Reynolds number possible.**

Time step

There is always numerical error associated with the time integration, that decrease with the usage of smaller Δt, as seen in section 4.1.1. To evaluate if this errors are affecting the statistics, three simulations with different time-steps but, with the rest of parameters and initial conditions equal, were performed. The common parameters are listed in table 4.5, the three Δt used are: $0.02\tau_\eta$, $0.01\tau_\eta$ and $0.005\tau_\eta$.

The Lagrangian second order structure function obtained for the three different time-steps (using a sample of 500000 particles) is show in figure 4.20. There are no visible differences between the three functions thus, one concludes that the characteristic time-steps used in the simulations have no effect on the results.

Table 4.5: Parameters of the simulations used to analyse the effect of Δt.

N	Re_λ	$k_{max}.\eta$	ν	$\overline{\epsilon}$	$\frac{T_L}{\tau_\eta}$
256	131.2	1.174	0.0071	9.98	12.23

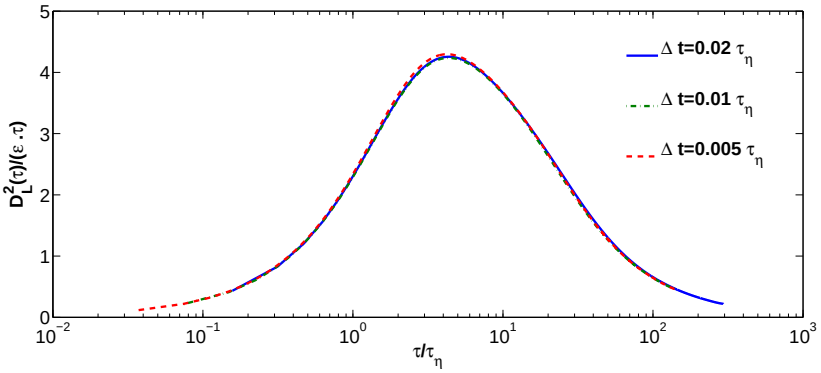

Figure 4.20: Lagrangian second order structure function for simulations with different time-steps.

Sample size

Another important parameter in the simulation that can have major influence on the results is the sample size used. A sample with low particles can cause results with high statistical error. Hence, an important question must be addressed: how many particles are required in order to have converged results? In order to be able to answer that question, with the simulation with the parameters listed in table 4.5, different samples sizes (125000, 250000 and 500000 particles) were used to compute the Lagrangian second order structure function. The results obtained are shown in figure 4.21.

Regarding the results shown in figure 4.21, no differences are observed therefore, it is possible to conclude that a sample size of 500000 particles is sufficient to obtain converged statistics (regarding second order functions).

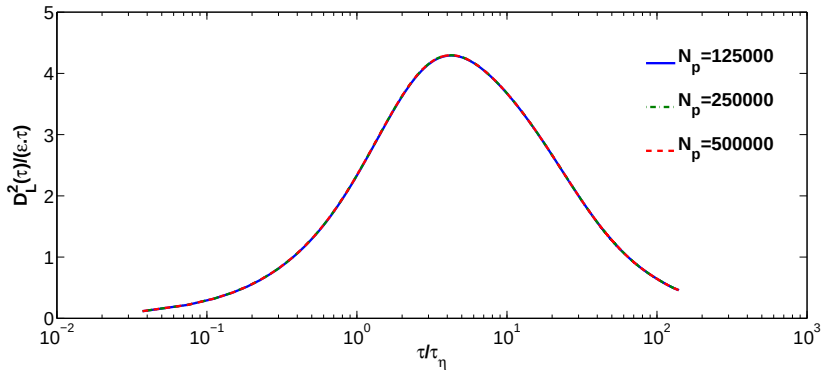

Figure 4.21: Lagrangian second order structure function for a single simulation computed with different sample sizes.

4.4.3 Comparison of the results with the literature

Probability density function of the velocity fluctuations

The probability density function of the velocity fluctuations is one of the most important functions regarding turbulence, as explained in chapter 2. For the simulation with the parameters listed in table 4.5, the curves obtained, for different time intervals, are presented in figure 4.22.

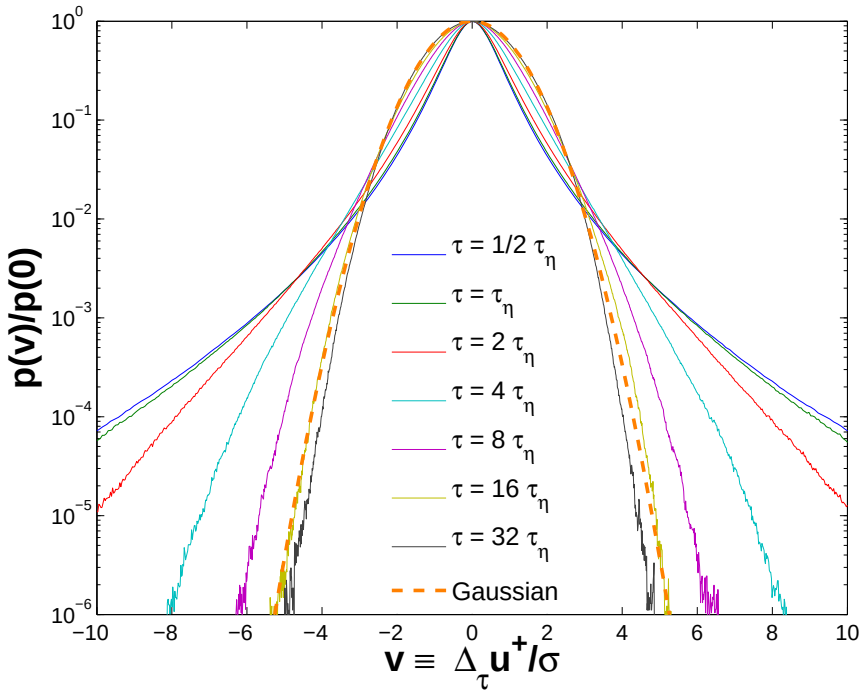

Figure 4.22: Normalized probability density function of the velocity fluctuations for different time lags for a simulation with the parameters listed in table 4.5.

For comparison figure 4.23 shows a PDF for a simulation with N=128 and $Re_\lambda = 93$ carried out by P.K Yeung [69]. Closely analysing both figures it is possible to conclude that the obtained

results are consistent.

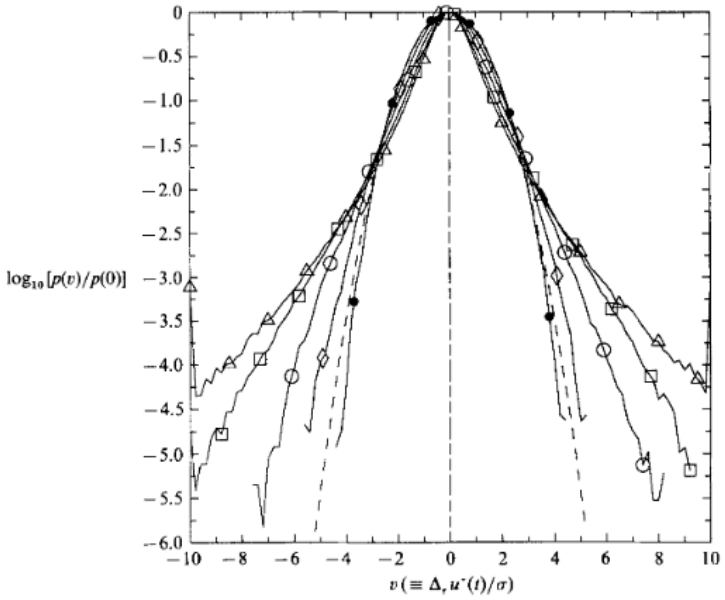

Figure 4.23: Normalized probability density function of the velocity fluctuations for several time lags: △, $\frac{\tau}{\tau_\eta} = 0.5$; □, $\frac{\tau}{\tau_\eta} = 2$; ○, $\frac{\tau}{\tau_\eta} = 4$; ♢, $\frac{\tau}{\tau_\eta} = 8$; ●, $\frac{\tau}{\tau_\eta} = 32$. Source: [69].

Lagrangian correlation function

As described in chapter 2 the Lagrangian correlation function is known to have a exponential decay [69]. Therefore, since the area below the curve is the Lagrangian integral time scale (T_L), then, in theory the correlation should be well approximated by $e^{-\frac{\tau}{T_L}}$. The correlation functions for each velocity component (u, v and w), obtained from the simulation with the parameters listed in table 4.5, are show in figure 4.24. **Analysing the figure it is evident that the exponential decay is observed, therefore, this is another proof of the accuracy and robustness of the code developed.**

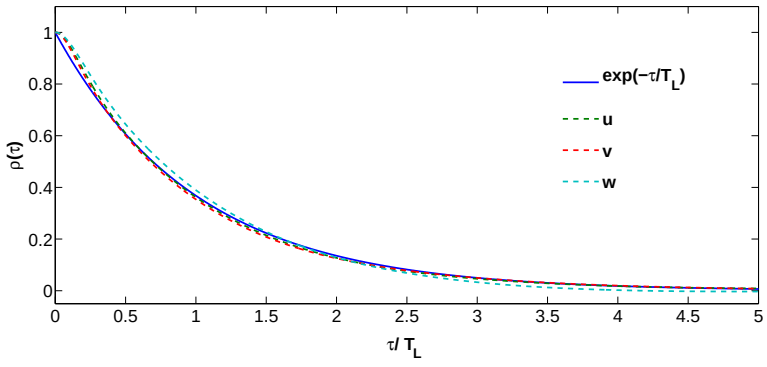

Figure 4.24: Lagrangian correlation function for each velocity component obtained from the simulation with the parameter listed in table 4.5. In addition, $e^{-\frac{\tau}{T_L}}$, for comparison, is also plotted.

Lagrangian second order structure function

It can be proven that the Lagrangian second order structure function in the dissipative scales ($\tau < \tau_\eta$) is given by $\frac{D_L^2(\tau)}{v_\eta^2} = a_0(\frac{\tau}{\tau_\eta})^2$, where $v_\eta = \frac{\eta}{\tau_\eta}$ (see for instance [69]). Thus, in a log-log plot the slope of the function must be 2, for small time-lags. Also, for time scales such that ($\tau \gg T_L$), as seen in chapter 2, the structure function is constant.

The Lagrangian second order structure function, computed using the simulation with the parameters listed in table 4.5, is plotted in figure 4.25. **Note that both zones described in the previous paragraph are visible, thus, this is another evidence of the reliability of the code implemented.**

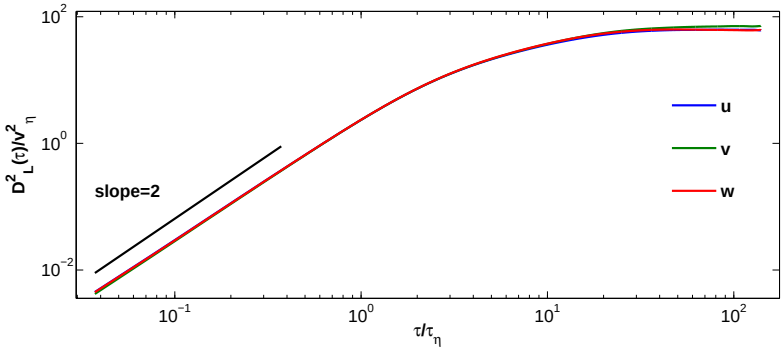

Figure 4.25: Lagrangian second order structure function for each velocity component obtained from the simulation with the parameter listed in table 4.5

Statistics dependence with Reynolds number (LVSF and Richardson)

Finally, in this section, it will demonstrated that the evolution of the statistics with the Reynolds number is the expected one. For that purpose, six simulations, using Newtonian fluid model, were performed. The simulation parameters are listed in table 4.6.

Table 4.6: List of Newtonian simulation parameters.

N	Re_λ	$k_{max}.\eta$	ν	$\bar{\epsilon}$	$\frac{T_L}{\tau_\eta}$	$N_{particles}$
32	24.35	1.07	0.1	9.97	3.35	500 000
64	49.71	1.08	0.04	9.90	5.20	500 000
128	87.74	1.03	0.015	9.87	7.69	614400
256	131.2	1.17	0.0071	9.98	12.23	614400
512	227.7	1.07	0.0025	10.04	17.74	614400
1024	380.6	1.09	0.001	9.85	30.81	1228800

The results regarding the Lagrangian second order structure function are shown in figure 4.26 and comparing to the results obtained by Yeung, presented in figure 2.2 ([3]), it is clear that the results are consistent.

The results regarding the dispersion statistics are shown in figure 4.28. Comparing with the results obtained by Sawford, presented in figure 4.27 ([56]) some differences are found. This differences are

justifiable with the fact that the simulations used in this work have different Reynolds numbers than the simulations in [56]. Notice that, in simulations from [56], the highest Reynolds number is almost 20 times higher than the lowest one, unlike the simulations carried out here in which the highest Reynolds number is only 4 times higher then the lowest one. Therefore the effects associated with the increasing Reynolds are much less pronounced in figure 4.28 than in figure 4.27. However, the same trend with increasing Reynolds is observed. First, the dislocation of the zone where all curves start two converge with a negative slope, has, in both figures, the same trend with the increasing Reynolds. Second, in both figures, the curve associated with the inital distance $r_0^+ = 4\eta$, tends to the horizontal line with the increasing Reynolds (the cyan one tha has the constant value of 0.6, which is the predicted value of the Richardson constant g) .

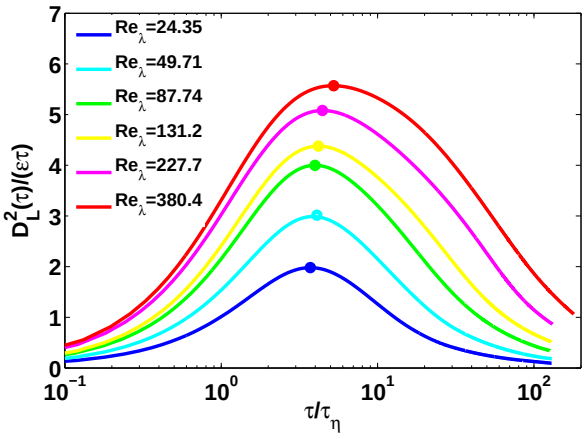

Figure 4.26: LVSF-2 as function of Reynolds number obtained in the present work, for the simulations with the parameters listed in table 4.6.

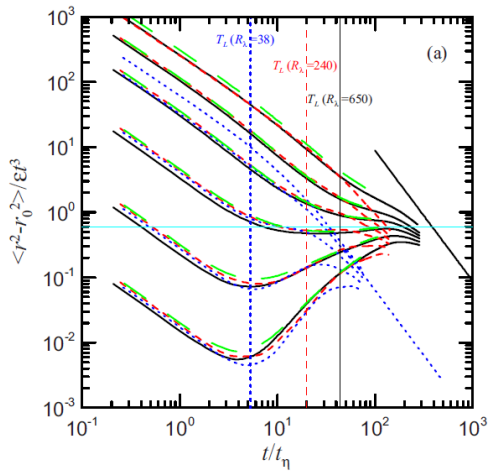

Figure 4.27: Relative dispersion plots for initial separations of, from bottom to top, $\frac{r_0^+}{\eta}$: 0.25; 1; 4; 16; 64; 256. As function of Reynolds number: Source: [56].

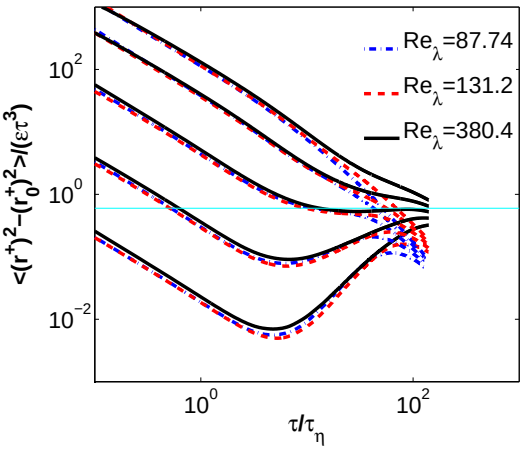

Figure 4.28: Relative dispersion plots, obtained in the present work, for initial separations of, from bottom to top, $\frac{r_0^+}{\eta}$: 0.25; 1; 4; 16; 64. The horizontal line (the cyan one), has a value of 0.6.

Chapter 5

Results

5.1 Effect of Hyper-Viscosity in Lagrangian statistics

The analysis of the effects of the Hyper-viscosity in the Lagrangian statistics will be made in two steps. First the classic Newtonian results, that were used to validate the code in section 4.4.3, will be analysed. Secondly the evolution of the LVSF-2 with the increase of the Reynolds number will be compared, qualitatively and quantitatively, between Newtonian an Hyper-viscosity flows. The dispersion statistics will only be discussed in section 5.3.

Even though the main objective is to study the LVSF-2, it will also be presented the scaling coefficient ζ_4 obtained using Hyper-viscosity.

5.1.1 Classic results

To analyse the classic results, .e.g, the exponential decay of the correlation function, an Hyper-viscous simulation with the parameters listed in table 5.1 will be used.

Table 5.1: Parameters of the simulations used for validation.

N	Re_λ	k_f	k_d	$\overline{\epsilon}$	$\frac{T_L}{\tau_\eta}$	$N_{particles}$
256	294	4	57	10.02	15.62	614400

Notice that unlike all the other simulations carried out in this work, the forcing peak is concentrated in the 4 wave number shell. The forcing scheme is a source of anisotropic motions [65], and, due to the boundary limits the higher the wave number of peak forcing, the higher the anisotropic effects. Thus, the choice of this value was made to guarantee that the anisotropic effects do not affect the statistics and therefore, ensures that the presence of discrepancies between the expected and obtained results using Hyper-viscosity, will not be originated from other sources then the model itself.

Lagrangian correlation

As described in chapter 2, the Lagrangian correlation function is known to have an exponential decay [69], and as explained in section 4.4.3 the correlation function should be well approximated by $e^{-\frac{\tau}{T_L}}$.

The correlation functions for each component (u, v and w), obtained from the simulation with the parameters listed in table 5.1 are plotted in figure 5.1. **A clear exponential decay of the correlation of each component is observed, therefore, the Hyper-viscosity does not affect the correlation statistics.**

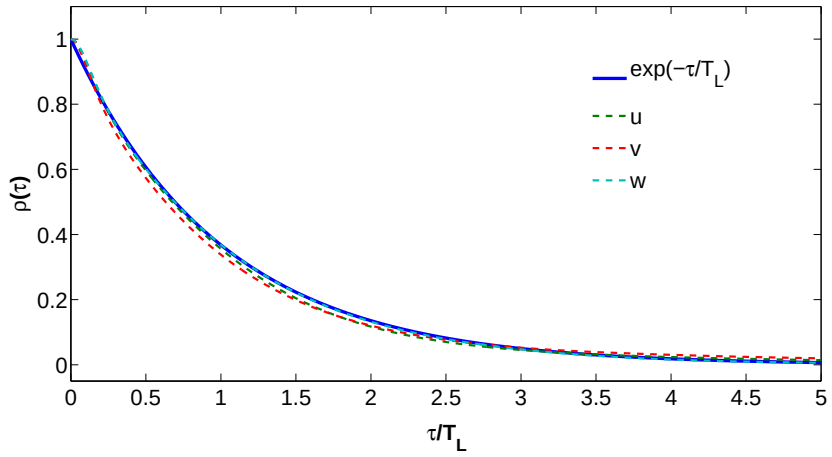

Figure 5.1: Lagrangian correlation function for each velocity component obtained from the simulation with the parameters listed in table 5.1. In addition, $e^{-\frac{\tau}{T_L}}$, for comparison is also plotted.

Another simulation with parameters $N = 256$ and $k_f = 2$ was carried out (the full description of the simulation parameters is indicated in table 5.2) to discuss the effect of anisotropic fluctuations in the statistics.

To estimate the anisotropic statistical degree in each simulations it was used the following parameter (the same definition is used in [38]):

$$S_L^2(\tau) = \frac{\overline{(\delta u^+(\tau))^2}}{\overline{(\delta v^+(\tau))^2}}. \tag{5.1}$$

Note that, with this definition, a flow with purely isotropic fluctuations must verify $S_L^2(\tau) = 1$.

The function $S_L^2(\tau)$ is plotted for both simulations in figure 5.2 and it is possible to see that anisotropic statistical degree in the simulation with $k_f = 2$ is higher, as expected, in almost every instants of time. Knowing this and comparing the correlation functions of both simulations, shown in figures 5.1 and 5.3, it is possible to see that for $k_f = 2$ the differences between correlation functions, at the same time, are higher. Thus, as stated, the anisotropic effects are higher for higher k_f and, due to that, some discrepancies, when comparing to a purely exponential decay, are observed in figure 5.3. However, the mean value of the three components show also a clear exponential decay (not shown in any figure), thus, the mean value of the three components is used to compute statistics such as $D_L^2(\tau)$, and function $S_L^2(\tau)$ is used to compute its uncertainty .

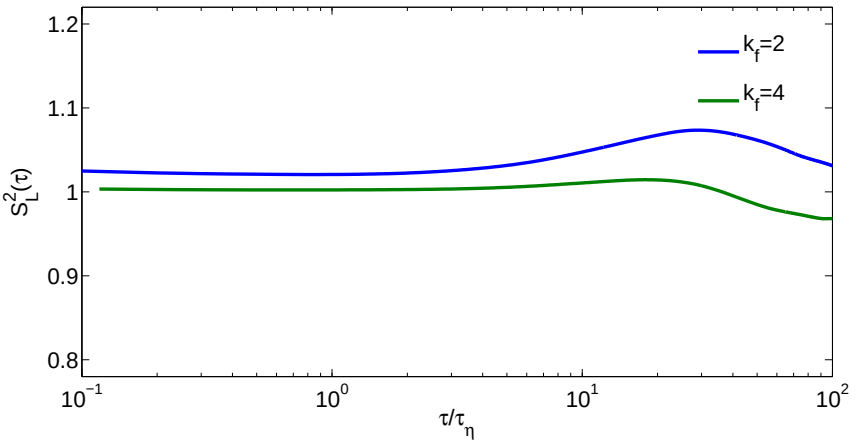

Figure 5.2: Anisotropic statistical degree, as function of time, for two simulations with different forcing peaks.

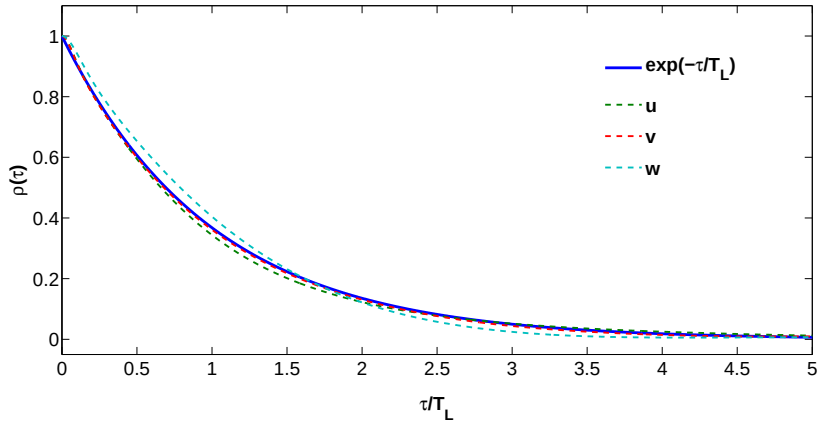

Figure 5.3: Lagrangian correlation function for each velocity component obtained from the Hyper-viscous simulation with $N = 256$, the other parameters are listed in table 5.2. In addition, $e^{-\frac{\tau}{T_L}}$, for comparison is also plotted.

Lagrangian second-order structure function

As stated in section 4.4.3, in the dissipation range, $\tau < \tau_\eta$, the LVSF-2 is proportional to τ^2, and thus, in a log-log plot the slope of that function must be 2, for small time lags. Also, for time scales such that $\tau \gg T_L$, $D_L^2(\tau)$ must be constant.

The Lagrangian second order structure function, computed using the simulation parameters listed in table 5.1, is plotted in figure 5.4. **Note that both zones described in the previous paragraph are visible, thus, this is another evidence that the Hyper-viscosity does not affect the laws observable in a Newtonian flow.**

Note that the scaling law $\frac{D_L^2(\tau)}{v_\eta^2} = a_0(\frac{\tau}{\tau_\eta})^2$ is deduced using the fact that for small time lags the relation $\delta u_i^+(\tau) \approx a_i^+\tau$ holds. Thus, even though it is expected that hyper-viscosity changes the small scale statistics, since the principle used to deduced this law is still valid then, it should be observed

anyway.

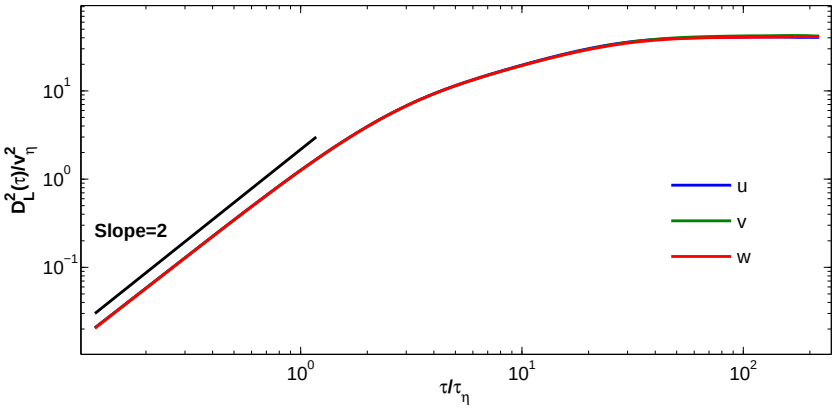

Figure 5.4: Lagrangian velocity structure function for each velocity component obtained from the simulations with the parameters listed in table 5.1.

PDF of the velocity fluctuations

The probability density function of the velocity fluctuations is one of the most important functions regarding turbulence, as explained in chapter 2. For the simulation with the parameters listed in table 5.1, the curves obtained, for different time intervals, are presented in figure 5.5.

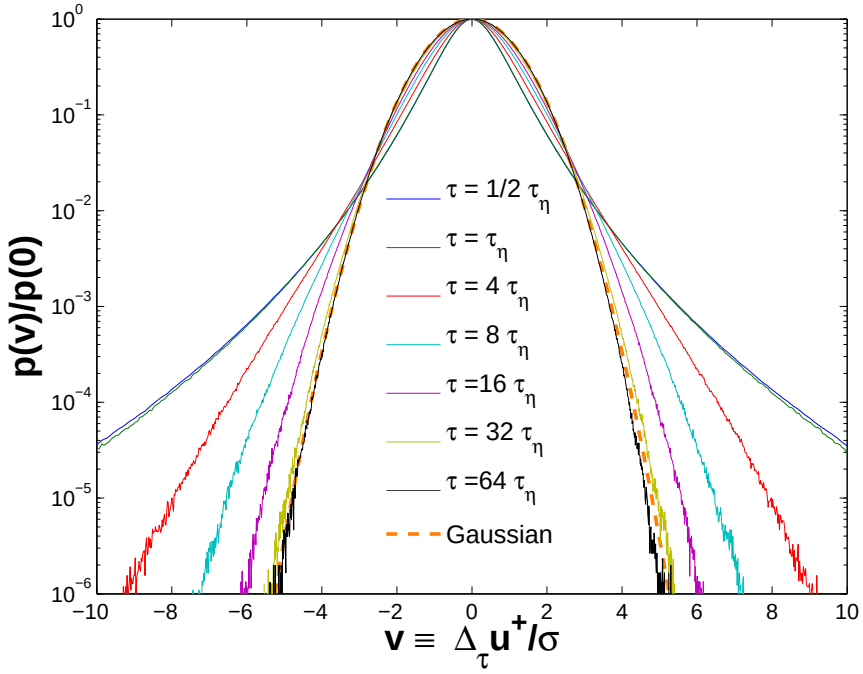

Figure 5.5: Normalized probability density function of the velocity fluctuations for different time-lags for a simulation with the parameters listed in table 5.1.

Comparing the PDFs for Hyper-viscosity shown in figure 5.5 with the ones obtained from a Newtonian

fluid 4.22 three facts are observed:

- In both figures it is possible to observe the shape evolution from stretched exponential to Gaussian, with the time lag increase, as expected (see section 2.4).

- For $\tau < \tau_\eta$, in both figures, the shape of the PDF remains almost unaltered. However, the PDF for small time lags are not equal in both cases, for instance for a time lag $\approx \tau_\eta$, in a Newtonian fluid $p(10)/p(0) \approx 6 \cdot 10^{-5}$, while in an Hyper-viscous one $p(10)/p(0) \approx 3 \cdot 10^{-5}$.

  As explained in section 2.4, for small time lags the PDF of velocity increments is deeply related with the PDF of the acceleration. Since the tails of this PDF are affected by the existence of small scale dissipative structures (due to trapping events in vortex filaments), and hyper-viscosity model changes the way energy is dissipated in those small scales (see section 2.3), thus, one concludes that differences between PDFs, for small time scale statistics, are expected. Therefore, no inconsistency is found.

- Finally it is visible that the time lag for which the PDF became Gaussian is higher for the Hyper-viscous flow. However, this happens only due to the Reynolds number difference, note that the Gaussian PDF is observed only when $\tau \gg T_L$.

In conclusion, observing the PDF evolution is clear that the small scale statistics differ between Newtonian and Hyper-viscous fluids, which was the expected. Also, the shape evolution of the PDF in Hyper-viscous flow is consistent with the description made in [40].

5.1.2 LVSF-2 dependence with Reynolds number

The main advantage of using Hyper-viscosity is that it allows to simulate turbulent flows with higher Reynolds numbers than a simulation, with the same number of grid points, with a Newtonian fluid. Since the Lagrangian inertial range has never been observed due to the limited Reynolds number achievable in Newtonian fluid simulations, one hypothesis arises: 'can Hyper-viscosity be used to compute the LVSF-2 in the inertial range?' .

The use of Hyper-viscosity, as seen before, maintains the principle characteristics of the Lagrangian statistics, except for small scale statistics, thus, no evidence that can refute the hypothesis was found. However, to confirm the hypothesis, one should compare the inertial scaling zones for both fluids, however, since this zone has not yet been observed, it will be analysed the evolution of the LVSF-2 with the Reynolds number and evaluated if it is consistent with the evolution in a Newtonian fluid.

For this purpose, in this work, five different simulations using Hyper-viscosity were carried out. The simulations parameters are listed in table 5.2. However, for comparison with Newtonian Reynolds number dependence only simulations with similar Reynolds number will be used (the three ones with lower Reynolds number).

Table 5.2: List of Hyper-viscous simulation parameters

N	Re_λ	k_f	k_d	$\bar{\epsilon}$	$\frac{T_L}{\tau_\eta}$	$N_{particles}$
128	276	2	24	9.97	13.47	614400
256	450	2	54	10.41	22.09	614400
512	701	2	105	9.73	35.87	614400
1024	1102	2	207	10.32	49.10	614400
2048	1744	2	412	10.04	≈ 77	1228800

The evolution of the LVSF-2 for the three simulations with the lowest Reynolds is shown in figure 5.6. Comparing with figure 4.26 it is possible to see that in both cases, the increase of Reynolds had cause the increase of the peak value (C_0^*), and also an increase of the lag time where the peak occurs (τ_0^*). Thus, for both Newtonian and Hyper-viscous fluids the increase of Reynolds causes qualitatively the same effects in the LVSF-2.

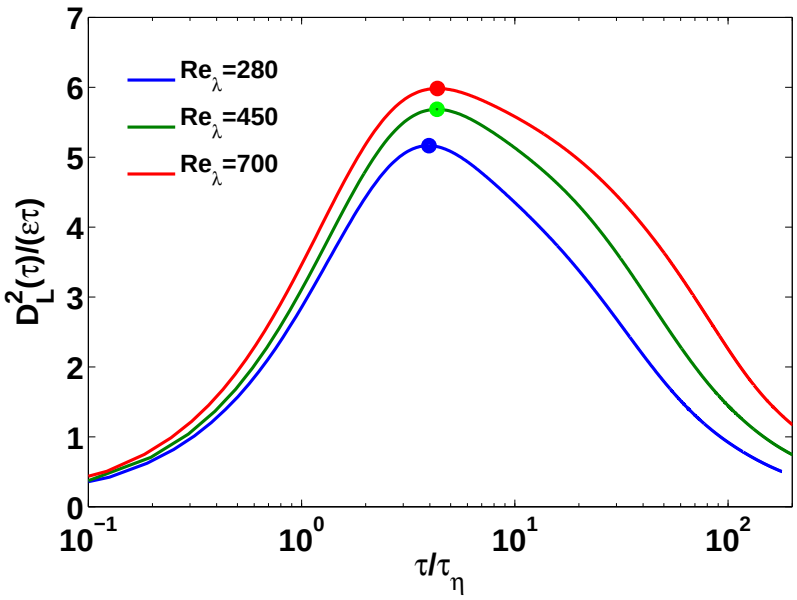

Figure 5.6: LVSF-2 as function of Reynolds number for simulation with parameters listed in table 5.2

To analyse if Reynolds number increase effect has a similar quantitative effect in Hyper-viscous simulations, one evaluates the increase in the peak value (C_0^*) as function of Re_λ in both fluids. As stated before, due to anisotropic fluctuations, there is an uncertainty in the LVSF-2. Since the three components have different peak values ($C_0^i = max(\frac{\overline{(\delta u_i^+(\tau))^2}}{\epsilon\tau})$), the uncertainty of C_0^* is computed as the $max(|C_0^* - C_0^i|)$, with $i \in \{1, 2, 3\}$. The results of C_0^* as function of Re_λ are shown in figure 5.7, in this figure is also plotted a fitting curve, given by $C_0^* = 6.5(1 + \frac{70}{Re_\lambda})^{-1}$, that B. Sawford obtained from his results [56] (the curve is not exact and it is used to compare the trend).

Analysing figure 5.7 one concludes that Hyper-viscosity accurately predicts the evolution of C_0^* as function of Reynolds number.

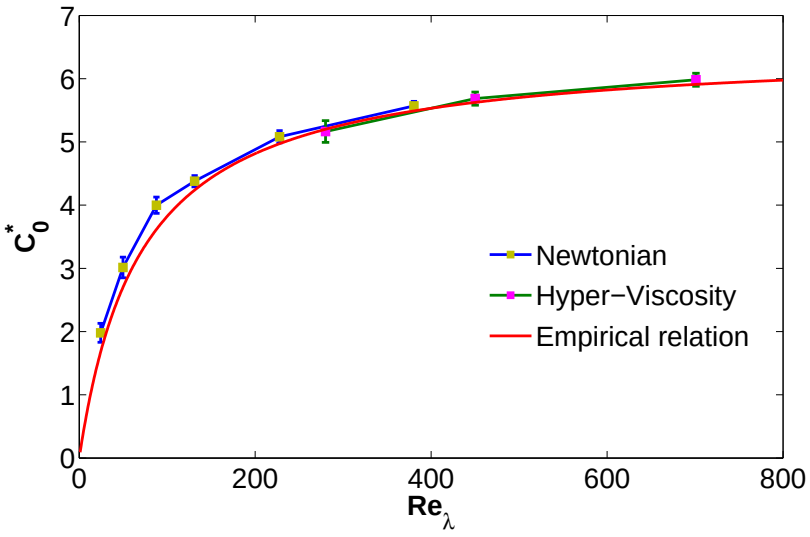

Figure 5.7: Evolution of the peak value C_0^* as function of Reynolds for both Newtonian and Hyper-viscous fluids. An empirical relation obtain in [56] is also plotted for comparison purposes.

Finally, a direct comparison between the shape of LVSF-2 of Hyper-viscosity and Newtonian fluids will be made by analysing figure 5.8. The figure is in a log-log plot to ensure that the adimensionalization does not affect the analysis. It is visible that the peak C_0^*, in the Newtonian simulations, occurs at a time lag τ_0^* higher than for a Hyper-viscous simulations. The reason why this happens is related with the fact that the peak occurs in the transition between dissipative and integral time scales. Since the use of hyper-viscosity results in the decrease of the width of the dissipative length scales (to enhance the width of the inertial range), then, it also causes the diminution of the width of the dissipative time scale, therefore, τ_0^* is smaller in Hyper-viscosity simulations.

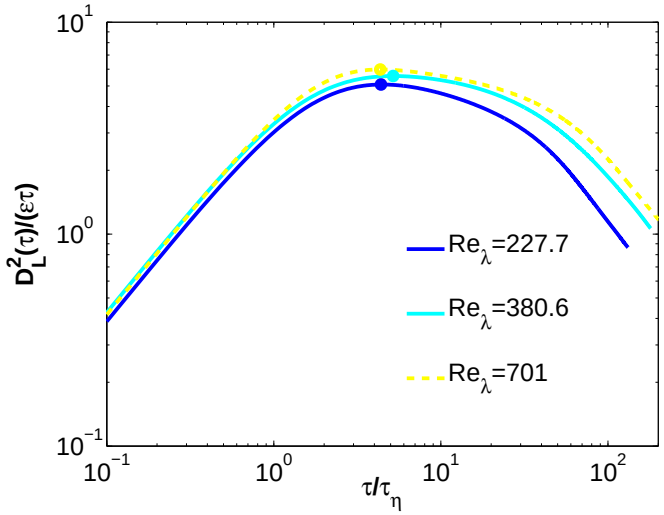

Figure 5.8: Direct comparison of the LVSF-2 for Newtonian and Hyper-viscous fluids. Solid lines are curves obtained with Newtonian simulations while dashed lines are curves obtained using Hyper-viscosity simulations.

However analysing figure 5.8 it is visible that, for $\tau \gg \tau_\eta$, the shape of LVSF-2 for Hyper-viscous is consistent with the shape observed in LVSF-2 for Newtonian fluids.

5.1.3 Scaling coefficient of the LVSF-4 in the inertial-range

Finally a comparison between Hyper-viscous and Newtonian fluids will be made for the scaling coefficient ζ_4. To compute this coefficient it was used the Hyper-viscous simulation with $N = 1024$. As explained in chapter 2, even though there is an absence of the inertia range, for low Reynolds numbers it is possible to compute the inertial scaling coefficients by using self-similarity [25].

According to self-similarity:

$$D_L^4(\tau) = (D_L^2(\tau))^{\frac{\zeta_4}{\zeta_2}}, \tag{5.2}$$

thus, ζ_4 can be computed as:

$$\zeta_4 = \frac{d(log(D_L^4(\tau)))}{d(log(D_L^2(\tau)))}\zeta_2. \tag{5.3}$$

Using the implicit function theorem, one concludes that ζ_4 can be computed as:

$$\zeta_4 = \frac{\frac{d(log(D_L^4(\tau)))}{d\tau}}{\frac{d(log(D_L^2(\tau)))}{d\tau}}\zeta_2. \tag{5.4}$$

The evolution of ζ_4 with time, computed using this formula, is shown in figure 5.9. Note that is assumed that $\zeta_2 = 1$.

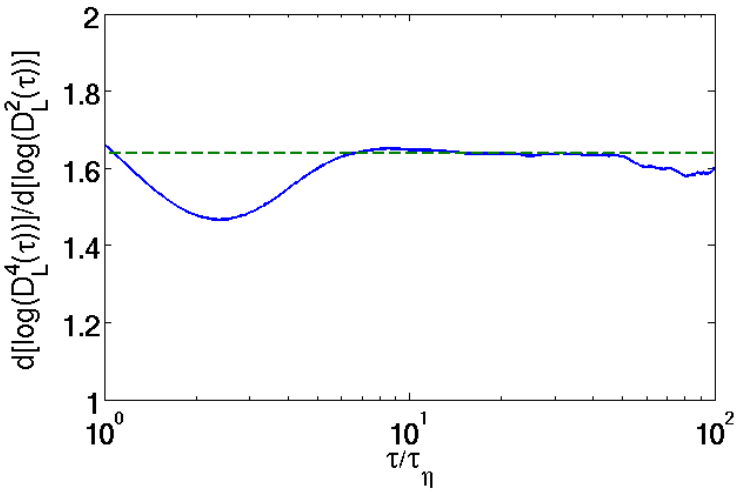

Figure 5.9: Scaling coefficient of the LVSF-4, obtained from an Hyper-viscous simulation with $Re_\lambda = 1102$. The green dashed line has the constant value of 1.64.

From this figure, three relevant facts must be highlighted:

- First, the reason why there are oscillations for $\tau > 60\tau_\eta$ is related with the fact that for $\tau \gg T_L$, $D_L^2(\tau)$ and $D_L^4(\tau)$ are tending to a constant, therefore the computation of ζ_4 using equation (5.4) tends to an indetermination $\frac{0}{0}$, and thus these oscillations are not physical.

- Second, the green dashed line has a constant value of $\zeta_4 = 1.64$. This value was computed by averaging the plotted function in the interval $[10\tau_\eta; 40\tau_\eta]$. To estimate the uncertainty of the scaling coefficient it is used the maximum difference between ζ_4 computed with the mean value of the three velocity components and ζ_4^i computed using only the i-th component.

  Thus, using Hyper-viscosity, it is obtained that the scaling coefficient of the LVSF-4, in the inertial range, is $\zeta_4 = 1.64 \pm 0.03$. In [38] the value estimated for this constant was $\zeta_4 = 1.66 \pm 0.02$, thus, the result obtained using Hyper-viscosity is consistent with the one obtained in DNS simulations using Newtonian fluid. Also, ζ_4 predicted using Hyper-viscosity is in the interval predicted by the multifractal formalism [38] (interval computed using different fractal dimensions for the longitudinal and transverse velocity fluctuations in the Eulerian frame). **Therefore, this is a clear proof that the Hyper-viscosity can be used to obtain the scaling coefficients in the inertial zone.**

- Also, there is a clear dip before the inertial range, that as explained in chapter 2, occurs due to the presence of trapping events. Therefore in Hyper-viscosity there are also trapping events.

In sum, in this section, all the results indicate that the Hyper-viscosity does not affect the inertial range, and thus can be used to study Lagrangian statistics. Due to this situation, if one desires to study the inertial range of the LVSF-n, he can use the Hyper-viscosity. Note that this is an extraordinary result because by using Hyper-viscosity one can obtain, for example, the LVSF-2 for $Re_\lambda \approx 250$ using a grid with only 128^3 point instead of 512^3 (the Newtonian grid required), and so, the decrease in the computational effort is tremendous, in that particular case, using Hyper-viscosity reduced the memory usage up to 1000 times, and thus, also the computational time required! Also at the present time, the simulation with the highest Reynolds number (≈ 1000) is obtained using a grid of 4096^3 points, for that same grid, using Hyper-viscosity, is expected a Reynolds number of 2500, therefore, the use of Hyper-viscosity will allow an increase of the maximum achievable Reynolds number in 150%.

5.2 Analysis of the Lagrangian Second order-structure as function of Reynolds number

We have seen in the previous section that Hyper-viscosity can be used to study the LVSF-2. Until now, the largest Reynolds for which the Lagrangian statistics had been studied was approximately 1000, however, **in the presented work two simulations with higher Reynolds number were carried out, one with $Re_\lambda = 1102$ and another with $Re_\lambda = 1774$, therefore, we are able to study this function like it never had been studied, and in a position that had never been achieved by no one else. Our principal concern is to try verify if $\zeta_2 = 1$, an open problem since 1941.**

In order to prove the theory, two things must be observed:

- The function $D_L^2(\tau)$ when adimensionalyzed by $\epsilon\tau$, must show a clear plateau, i.e., a zone where

the function is constant in the value C_0, an universal constant.

- In the K41 theory, it is assumed isotropy is the small scale, thus, the law is only valid if C_0 a is equal for the three components.

To evaluate if the first requirement is fulfilled let us start by analysing the LVSF-2, plotted for different Reynolds numbers in figure 5.10. First since the LVSF-2 is constant for $\tau \gg T_L$ it is obvious that, for time lags in that interval, the slope of the function $\frac{D_L^2(\tau)}{\epsilon\tau}$ has to be -1. However, in figure 5.10 it is clear that with the Reynolds number increase the right tail of the function $\frac{D_L^2(\tau)}{\epsilon\tau}$ has a higher slope (lower in absolute value) during a larger interval of time (as right it is meant after the peak). The question is, will the slope increase up to zero with the Reynolds number increase and the peak will became a plateau?

To conclude whether or not, in figure 5.10 for the highest Reynolds number, there is already a plateau, it will be evaluated the width of the interval were $\frac{D_L^2(\tau)}{\epsilon\tau} > 0.99C_0^*$. The interval were this condition is valid is approximately: $[3.8\tau_\eta; 7.2\tau_\eta]$, thus, the width of this interval, in a log-log plot, is 28% of a decade. Also, the inertial range must be such that $\tau_\eta \ll \tau \ll T_L$, the width of the interval $[\tau_\eta; 77\tau_\eta]$ is 188% of a decade, therefore, a plateau is observed in about 15% of the overestimated width of the inertial range. Since there are no exact rules that clearly defined what can be considered as a plateau, one cannot state that a plateau is observed, however further evidence that corroborate the theory that $\zeta_2 = 1$ will be shown.

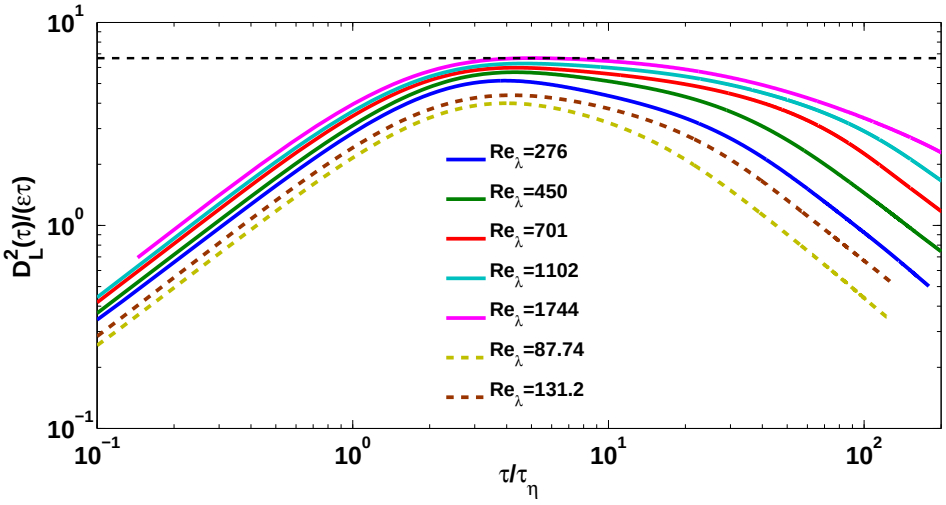

Figure 5.10: LVSF-2 for different Reynolds numbers. Dashed lines are curves obtained with Newtonian simulations while solid lines are curves obtained using Hyper-viscosity simulations.

The second requirement that must be fulfilled, to prove the K41 theory, is that C_0^* must be equal when computed for each velocity component individually, i.e., isotropy must be verified. To evaluate if this situation is verified one could use the definition of anisotropic statistical degree ($S_L^2(\tau)$), however since this parameter does not reflect the differences of C_0^* computed with the velocity component along the z direction, the parameter that will be used instead is $e = \frac{max(|C_0^* - C_0^i|)}{C_0^*}$. This value, for the simulation with the largest Reynolds is $e = 0.002$, thus small relative differences exist between the three components and so, one concludes that indeed the second requirement is fulfilled. Also, another evidence of the

presence of the scaling law, in the simulation with higher Reynolds, is that the value e obtained for that simulation is the lowest of all the simulations carried out using Hyper-viscosity with $k_f = 2$ (for: N=1024 $e = 0.011$; N=512 $e = 0.013$; N=256 $e = 0.019$; N=128; $e = 0.059$). Also, it is the only simulation carried out in this work in which the time lag where the peak occurs (τ_0^*) is equal for the three components.

To conclude, it had been presented clear evidences, for the first time in 75 years of investigation, that corroborate the existence a linear scaling law for the LVSF-2. The predicted value for the universal constant is $C_0 = 6.7$.

5.3 Analysis of the particle dispersion statistics as function of Reynolds number

As stated in chapter 2, another variable of interest is the relative dispersion, which for two particle statistics, is given by:

$$\delta|\vec{r}^{+}(t,\tau)| = |\vec{r}^{+}(t+\tau)| - |\vec{r}^{+}(t)|. \tag{5.5}$$

In turbulence since the analysis is statistic, one must evaluate all the moments of any order of the PDF of $\delta|\vec{r}^{+}(t,\tau)|$. The moment of n-th order is given by:

$$\overline{(\delta|\vec{r}^{+}(t,\tau)| - \overline{\delta|\vec{r}^{+}(t,\tau)|})^n}. \tag{5.6}$$

Notice that in the specific case of the velocity, since we are studying HIT, the mean value of the velocity is zero and thus the n-th moment is written just as $\overline{(\delta\vec{u_i}^{+}(\tau))^n}$.

It is also assumed that, as consequence of the mean velocity field being 0, then $\overline{\delta|\vec{r}^{+}(t,\tau)|} = 0$. Considering this, the second moment of the PDF of the relative dispersion is:

$$\overline{(\delta|\vec{r}^{+}(\tau)| - \overline{\delta|\vec{r}^{+}(\tau)|})^2} = \overline{(\delta|\vec{r}^{+}(\tau)|)^2} = \overline{(|\vec{r}^{+}(t+\tau)| - r_0^{+})^2}. \tag{5.7}$$

However, if $\overline{\delta|\vec{r}^{+}(\tau)|} = 0$, then $\overline{|\vec{r}^{+}(t+\tau)|} = r_0^{+}$, and thus equation (5.7) can be written as:

$$\overline{(|\vec{r}^{+}(t+\tau)| - r_0^{+})^2} = \overline{|\vec{r}^{+}(t+\tau)|^2} - 2\overline{|\vec{r}^{+}(t+\tau)|}r_0^{+} + (r_0^{+})^2 = \overline{|\vec{r}^{+}(t+\tau)|^2} - (r_0^{+})^2. \tag{5.8}$$

Note that, $\overline{|\vec{r}^{+}(t+\tau)|^2} - (r_0^{+})^2$ is the variable analysed in the study of relative dispersion, as can be seen in the plot of figure 4.27. However, the premiss, that $\overline{\delta|\vec{r}^{+}(t,\tau)|} = 0$ is not correct, therefore, in this work, for the first time, second order moment will be computed exactly.

First, in figures 5.11 and 5.12, both the value of $Var(\delta|r^{+}|)$ (second order moment) and $\overline{(|\vec{r}^{+}(t+\tau)| - r_0^{+})^2}$ are plotted as function of time for Newtonian simulations with $Re_\lambda = 87.74$ and $Re_\lambda = 380.6$, respectively. It is visible, in both figures, that indeed there are differences between the two function and thus, the assumption of $\overline{\delta|\vec{r}^{+}(t,\tau)|} = 0$ is not valid (latter the evolution of this quantity will be shown in figure 5.16).

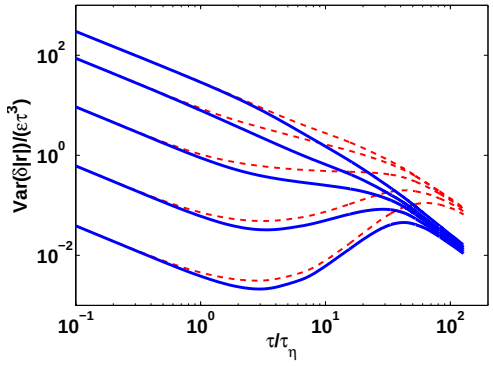

Figure 5.11: Relative dispersion plots, obtained for a simulation with $Re_\lambda = 87.74$ using a Newtonian fluid, for initial separations of, from bottom to top, $\frac{r_0^+}{\eta}$: 0.25; 1; 4; 16; 64. The dashed line is computed considering the hypothesis $\overline{\delta|\vec{r}^+(t,\tau)|} = 0$ and the solid one without it.

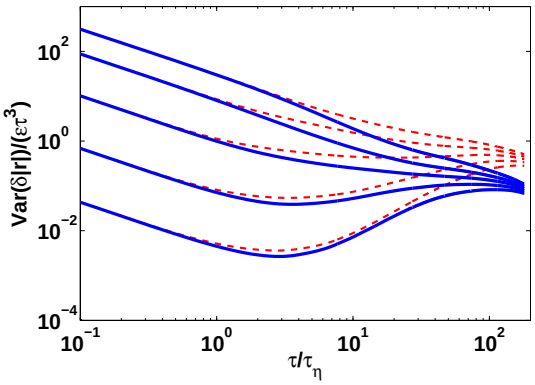

Figure 5.12: Relative dispersion plots, obtained for a simulation with $Re_\lambda = 380.6$ using a Newtonian fluid, for initial separations of, from bottom to top, $\frac{r_0^+}{\eta}$: 0.25; 1; 4; 16; 64. The dashed line is computed considering the hypothesis $\overline{\delta|\vec{r}^+(t,\tau)|} = 0$ and the solid one without it.

Before continuing the analysis of this new variable it is important to state that in order to prove the T3 Richardson law two requirements must be fulfilled:

- The function $\frac{Var(\delta|r^+|)}{\epsilon\tau^3}$, must show a clear plateau in the time inertial range, for separations in the inertial region scale.

- The constant g of the plateau must be universal and independent of the initial distances between particles.

Notice that, the previous results from direct analysis (e.g. 4.27), besides not showing a clear evidence of the existence of a plateau, were inconsistent because the approximation to plateau was believed to exist for initial separation of $r_0^+ = 4\eta$, a scale from the dissipation range, thus if the increment of the mean distance was zero $\overline{|\delta|r||} = 0$, then this scaling zone wouldn't be observe in the inertial scale length range, as stated by Batchelor [55].

To evaluate if $Var(\delta|r^+|)$ really scales with the cube of time lag it is necessary to analyse the dependence of this parameter with the Reynolds number. In figure 5.13 are shown different curves for five initial separations and three Reynolds numbers. It is clear that none of the two requirements to prove the Richardson T3 law are fulfilled.

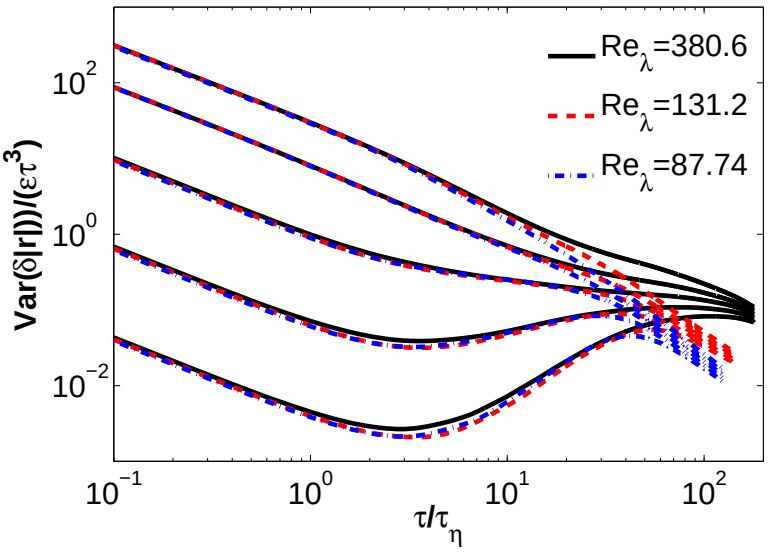

Figure 5.13: Relative dispersion plots dependence with Reynolds number, for initial separations of, from bottom to top, $\frac{r_0^+}{\eta}$: 0.25; 1; 4; 16; 64. This results are regarding Newtonian fluids.

However, as seen before, Hyper-viscosity can be used to compute Lagrangian statistics, therefore, it will also be used here to obtain curves for higher Reynolds numbers. The curves obtained are plotted in figure 5.14, and it is clear there is the tendency to a plateau as the Reynolds number increases. Also, for the simulation with $Re_\lambda = 1744$ that plateau already exist as can be seen in figure 5.15. This is the first time that a clear plateau was observed from direct measurements. Also, even though all the curves in figure 5.15 do not yet show a plateau, analysing figure 5.14 it is clear that, as the Reynolds increases, all the curves are converging. The expected is that they all converge to the constant line with value 0.165.

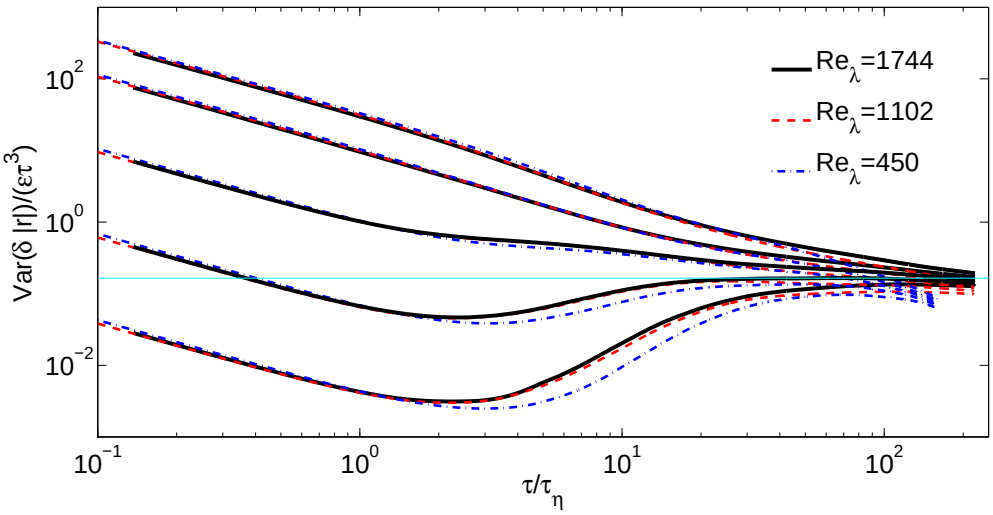

Figure 5.14: Relative dispersion plots dependence with Reynolds number, for initial separations of, from bottom to top, $\frac{r_0^+}{\eta}$: 0.25; 1; 4; 16; 64. This results are for Hyper-viscous fluids. The cyan line has the constant value of 0.165.

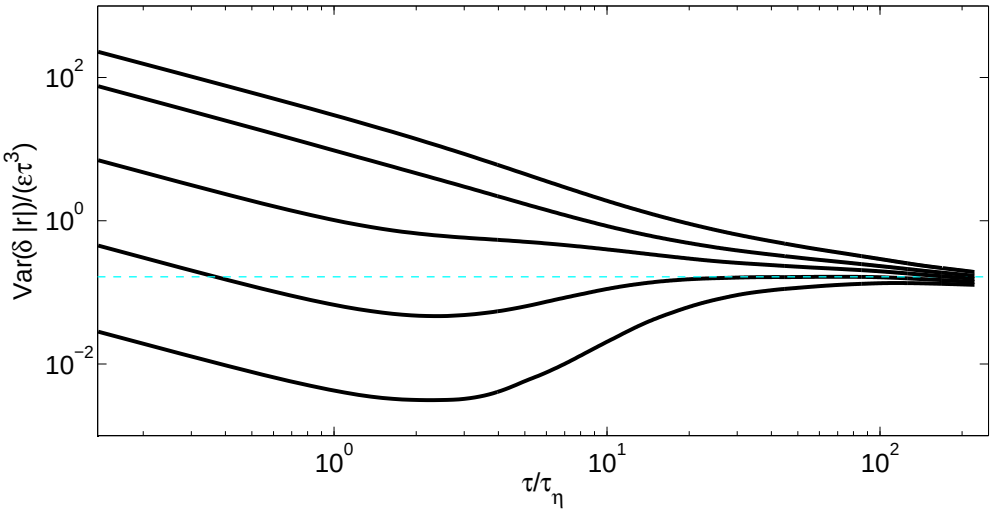

Figure 5.15: Relative dispersion plots dependence with Reynolds number, for initial separations of, from bottom to top, $\frac{r_0^+}{\eta}$: 0.25; 1; 4; 16; 64. These results are from the simulation carried out in this work the highest Reynolds. The cyan line has the constant value of 0.165.

Finally, as stated before, the Richardson law must be observed for time lags in the inertial time range scale and for mean particle distances in the inertial length scale range. To see if this situation is observed it is plotted in figure 5.16 the mean distance between particles as function of time. Analysing this figure it is possible to see that except for $\tau < \tau_\eta$ the assumption that the mean distance is constant is not valid, which could be predicted by analysing figures 5.11 and 5.12 since the quantities $Var(\delta|r|)$ and $\overline{(|\vec{r}^+(t+\tau)| - r_0^+)^2}$ are nearly equal in that same interval.

Notice that, in figure 5.16, there are two cyan lines that define the limits of the inertial range, the lowest one is the dimension of the dissipative scales η and the other one the dimension of the largest eddies l_0. Comparing figures 5.15 and 5.16 it is possible to observe that the region were the scaling law is observed is exactly in the inertial range!

Considering all this, we believe that, after 90 years of discussion, it has been finally proved that the T3 law is valid. Also the universal constant expected is $g = 0.165$.

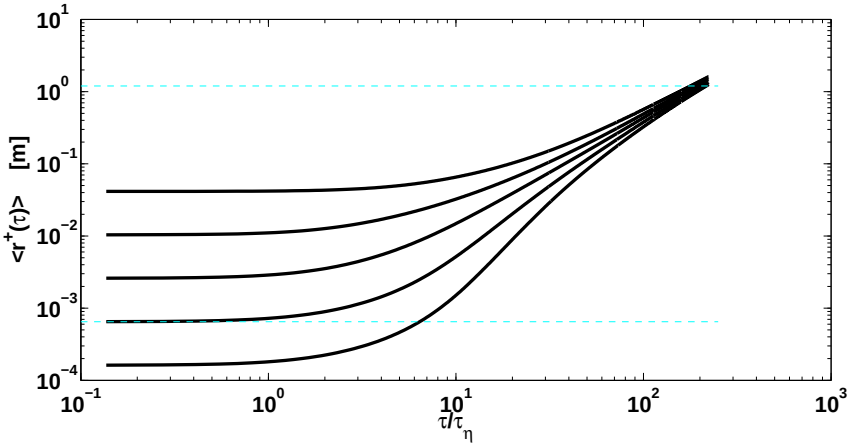

Figure 5.16: Mean distance between particles as function of time, from bottom to top, $\frac{r_0^+}{\eta}$: 0.25; 1; 4; 16; 64. This results the simulation carried out in this work the highest Reynolds. Cyan lines define the limit values of the inertial scale length range.

Chapter 6

Conclusions

6.1 Achievements

The present thesis work, was dedicated to fundamental study of turbulence in a Lagrangian frame, which is a natural approach to understand turbulent transport in contexts as industrial mixing, cloud formation, turbulent combustion or even pollutant dispersion [1] [2] [3] [4]. During this study four major achievements, that will be now summarized, were made:

- A numerical code for DNS based on pseudo-spectral schemes with particle tracking in a parallel architecture was developed. Also, even though particles roam across all the domain, by minimizing the number of synchronous communications the code developed was proven to be highly scalable.

  The code developed make it possible to compute, with high precision, quantities involved in the flow and thus, it was an extremely important tool for the investigation component of this thesis.

- For the first time, the effect of Hyper-viscosity in Lagrangian statistics was evaluated. It was shown that the Hyper-viscosity model can be used to study Lagrangian statistics except for dissipative time lags.

  Thus, if one desires to study the inertial range of the LVSF-n, he can use the Hyper-viscosity. Note that this an extraordinary result because using Hyper-viscosity one can obtain, for example, the LVSF-2 for $Re_\lambda \approx 250$ using a grid with only 128^3 point instead of 512^3 (the Newtonian grid required), and so, the decrease in the computational effort is tremendous, in that particular case, using Hyper-viscosity reduce the memory usage up to 1000 times, and thus, also the computational time required!

  Also at the present time, the simulation with the highest Reynolds number (≈ 1000) is obtained using a grid of 4096^3 points, for that same grid, using Hyper-viscosity, is expected a Reynolds number of 2500, therefore, the use of Hyper-viscosity will allow an increase of the maximum achievable Reynolds number in 150%.

- Using Newtonian fluids the maximum Reynolds number ever achieved is approximately $Re_\lambda =$

1000 and by using this new tool to compute Lagrangian statistics, two simulations with the highest Reynolds numbers ever were carried out! One with $Re_\lambda = 1102$ and other with $Re_\lambda = 1774$.

Even in experimental studies the Reynolds number achievable is lower than this ones, thus, this two simulations, made it possible to study Lagrangian statistics in a way that had never been studied before. Being in this position an attempt was made to answer the question: 'Does the second order Lagrangian velocity structure function scales linearly with time?', a question that had never been answered since 1941 and that is the most important unsolved problem in Lagrangian turbulence. The reason why a solution to this problem is so important it is because it has consequences in both in a fundamental level to understand if the Kolmogorov similarity theory is valid in a Lagrangian framework, if the multifractal theory correctly links the Eulerian and Lagrangian view, and at a practical level, because the knowledge of the universal constant C_0 is crucial to the construction of stochastic models and the measuring of higher order scaling coefficients is made using extended self-similarity [25] in which it is assumed that this law is valid.

From the results obtained, for the first time in 75 years of investigation, it was presented clear evidence that corroborate the existence a linear scaling law for the LVSF-2. Also it was predicted that the universal constant is $C_0 = 6.7$.

- Using the exact mathematical definition of the second order moment of the relative dispersion PDF, without any further hypothesis, it was observed that the curves for that parameter differ from what is observe in literature (e.g. [56]). By evaluating the influence of the Reynolds number in these new statistics (also using Hyper-viscosity), it was possible to see that, indeed there is an integral scaling range, where the Richardson T3 law holds. Also relevant is that, as theoretically expected, in that range the mean distance between the particles is in the inertial length scale range. This was the first study in which from direct measurements (numerical and experimental) an agreement between theory and results is found. Due to this great agreement one can conclude that in this work a problem with over 90 years as been finally solved. Also, as consequence, for the first time the Richardson universal constant was measured, $g = 0.165$.

6.2 Future Work

In a future work it would be interesting to perform a simulation with Hyper-viscosity in a grid with $N = 4096^3$ points, to study, for higher Reynolds numbers, both the LVSF-2 and also dispersion statistics.

Also, it would be interesting, using Hyper-viscosity, to evaluate the dynamics of tetrads and study the scaling laws of the eigenvalues of the inertia tensor (another open problem in Lagrangian turbulence).

Bibliography

[1] S. B. Pope. *Turbulent Flows*. Cambridge University Press, 2000.

[2] S. B. Pope. Lagrangian pdf methods for turbulent flows. *Annual Review of Fluid Mechanics*, 26(1): 23–63, 1994.

[3] P. K. Yeung. Lagrangian investigations of turbulence. *Annual Review of Fluid Mechanics*, 34(1): 115–142, 2002.

[4] K. R. S. Peter A. Davidson, Yukio Kaneda. *Ten Chapters of Turbulence*. Cambridge University Press, 2013.

[5] A. S. Monin and A. M. Yaglom. *Statistical fluid mechanics: mechanics of turbulence, Vol. 1*. M.I.T. Press, Cambridge., 1975.

[6] O. Reynolds. An experimental investigation of the circumstances which determine whether the motion of water shall be direct or sinuous, and of the law of resistance in parallel channels. *Philosophical Transactions of the Royal Society of London*, 1883.

[7] O. Reynolds. On the dynamical theory of incompressible viscous fluids and the determination of the criterion. *Philosophical Transactions of the Royal Society of London*, 1894.

[8] P. A. Davidson. *Turbulence, an introduction for scientists and engineers*. Oxford University Press, 2004.

[9] L. F. Richardson. *Weather prediction by numerical process*. Cambridge University Press, 1922.

[10] U. Frisch. *Turbulence*. Cambridge University Press, 1995.

[11] G. I. Taylor. Statistical theory of turbulence. IV. Diffusion in a turbulent air stream. *Proceedings of the Royal Society of London*, 151:465–478, 1935.

[12] A. N. Kolmogorov. Local structure of turbulence in an incompressible fluid for very large Reynolds numbers. *Dokl. Aka. Nauk SSSR*, 30:301–305, 1941.

[13] V. de Brederode. *Fundamentos de Aerodinâmica incompressivel*. edited by the Author, Lisbon, 1997.

[14] G. I. Taylor. Diffusion by continuous movements. *Proc. London Math Soc.*, pages 196–212, 1922.

[15] N. Mordant, P. Metz, O. Michel, and J.-F. Pinton. Measurement of Lagrangian velocity in fully developed turbulence. *Phys. Rev. Lett.*, 87:214501, Nov 2001.

[16] R. Volk, N. Mordant, G. Verhille, and J.-F. Pinton. Laser doppler measurement of inertial particle and bubble accelerations in turbulence. *EPL (Europhysics Letters)*, 81(3):34002, 2008.

[17] A. Pumir, B. I. Shraiman, and M. Chertkov. The lagrangian view of energy transfer in turbulent flow. *EPL (Europhysics Letters)*, 56(3):379, 2001.

[18] A. N. Kolmogorov. Dissipation of energy in the locally isotropic turbulence. *Proceedings: Mathematical and Physical Sciences*, 434(1890):15–17, 1991.

[19] A. Lanotte, L. Biferale, G. Boffetta, and F. Toschi. A new assessment of the second-order moment of lagrangian velocity increments in turbulence. *Journal of Turbulence*, 14(7):34–48, 2013.

[20] T. von Kàrmàn and L. Howarth. On the statistical theory of isotropic turbulence. *Proceeding of the Royal Society of London A*, 164:192–215, 1938.

[21] A. N. Kolmogorov. A refinement of previous hypotheses concerning the local structure of turbulence in a viscous incompressible fluid at high reynolds number. *Journal of Fluid Mechanics*, 13:82–85, 1962.

[22] U. Frisch, P.-L. Sulem, and M. Nelkin. A simple dynamical model of intermittent fully developed turbulence. *Journal of Fluid Mechanics*, 87(4):719–736, 04 2006.

[23] U. Frisch and G. Parisi. Fully developed turbulence and intermittency. *Turbulence and predictability in geophysical fluid dynamics and climate dynamics*, 88:71–88, 1985.

[24] Z.-S. She and E. Leveque. Universal scaling laws in fully developed turbulence. *Physical review letters*, 72(3):336, 1994.

[25] R. Benzi, S. Ciliberto, R. Tripiccione, C. Baudet, F. Massaioli, and S. Succi. Extended self-similarity in turbulent flows. *Physical review E*, 48(1):R29, 1993.

[26] G. K. Batchelor. *The Theory of Homogeneous Turbulence*. Cambridge University Press, 1953.

[27] V. Borue and S. A. Orszag. Forced three-dimensional homogeneous turbulence with hyperviscosity. *EPL (Europhysics Letters)*, 29(9):687, 1995.

[28] V. Borue and S. A. Orszag. Numerical study of three-dimensional kolmogorov flow at high reynolds numbers. 306:293–323, 2006.

[29] K. Spyksma, M. Magcalas, and N. Campbell. Quantifying effects of hyperviscosity on isotropic turbulence. *Physics of Fluids*, 24(12), 2012.

[30] A. G. Lamorgese, D. A. Caughey, and S. B. Pope. Direct numerical simulation of homogeneous turbulence with hyperviscosity. *Physics of Fluids*, 17(1), 2005.

[31] P. K. Yeung, S. B. Pope, and B. L. Sawford. Reynolds number dependence of lagrangian statistics in large numerical simulations of isotropic turbulence. *Journal of Turbulence*, 7:N58, 2006.

[32] B. L. Sawford and P. Yeung. Kolmogorov similarity scaling for one-particle Lagrangian statistics. *Physics of Fluids (1994-present)*, 23(9):091704, 2011.

[33] L. Biferale and A. Lanotte. About the second order moment of the Lagrangian velocity increments. *University of California Santa Barbara, Kavli Institute Preprint, NSF–ITP–11–103*, 2011.

[34] G. Falkovich, H. Xu, A. Pumir, E. Bodenschatz, L. Biferale, G. Boffetta, A. S. Lanotte, F. Toschi, et al. On Lagrangian single-particle statistics. *Physics of Fluids*, 24(5):055102, 2012.

[35] M. Borgas. The multifractal Lagrangian nature of turbulence. *Philosophical Transactions of the Royal Society of London A: Mathematical, Physical and Engineering Sciences*, 342(1665):379–411, 1993.

[36] F. Toschi and E. Bodenschatz. Lagrangian properties of particles in turbulence. *Annual Review of Fluid Mechanics*, 41:375–404, 2009.

[37] G. Boffetta, F. De Lillo, and S. Musacchio. Lagrangian statistics and temporal intermittency in a shell model of turbulence. *Physical Review E*, 66(6):066307, 2002.

[38] R. Benzi, L. Biferale, R. Fisher, D. Lamb, and F. Toschi. Inertial range Eulerian and Lagrangian statistics from numerical simulations of isotropic turbulence. *Journal of Fluid Mechanics*, 653:221–244, 2010.

[39] N. Mordant, J. Delour, E. Léveque, O. Michel, A. Arnéodo, and J.-F. Pinton. Lagrangian velocity fluctuations in fully developed turbulence: scaling, intermittency, and dynamics. *Journal of Statistical Physics*, 113(5-6):701–717, 2003.

[40] L. Chevillard, S. Roux, E. Lévêque, N. Mordant, J.-F. Pinton, and A. Arnéodo. Lagrangian velocity statistics in turbulent flows: Effects of dissipation. *Physical review letters*, 91(21):214502, 2003.

[41] O. Kamps, R. Friedrich, and R. Grauer. Exact relation between Eulerian and Lagrangian velocity increment statistics. *Physical Review E*, 79(6):066301, 2009.

[42] R. Friedrich, R. Grauer, H. Homann, and O. Kamps. Statistics of a mixed Eulerian-Lagrangian velocity increment in fully developed turbulence. *Physica Scripta*, 79(5):055403, 2009.

[43] L. Biferale, E. Bodenschatz, M. Cencini, A. S. Lanotte, N. T. Ouellette, F. Toschi, and H. Xu. Lagrangian structure functions in turbulence: A quantitative comparison between experiment and direct numerical simulation. *Physics of Fluids (1994-present)*, 20(6):065103, 2008.

[44] A. Arnéodo, R. Benzi, J. Berg, L. Biferale, E. Bodenschatz, A. Busse, E. Calzavarini, B. Castaing, M. Cencini, L. Chevillard, et al. Universal intermittent properties of particle trajectories in highly turbulent flows. *Physical Review Letters*, 100(25):254504, 2008.

[45] L. Biferale, G. Boffetta, A. Celani, A. Lanotte, and F. Toschi. Particle trapping in three-dimensional fully developed turbulence. *Physics of Fluids (1994-present)*, 17(2):021701, 2005.

[46] F. Toschi, L. Biferale, G. Boffetta, A. Celani, B. Devenish, and A. Lanotte. Acceleration and vortex filaments in turbulence. *Journal of Turbulence*, (6):N15, 2005.

[47] A. La Porta, G. A. Voth, A. M. Crawford, J. Alexander, and E. Bodenschatz. Fluid particle accelerations in fully developed turbulence. *Nature*, 409(6823):1017–1019, 2001.

[48] G. A. Voth, A. la Porta, A. M. Crawford, J. Alexander, and E. Bodenschatz. Measurement of particle accelerations in fully developed turbulence. *Journal of Fluid Mechanics*, 469:121–160, 2002.

[49] C. Beck. On the small-scale statistics of lagrangian turbulence. *Physics Letters A*, 287(3):240–244, 2001.

[50] C. Beck. Lagrangian acceleration statistics in turbulent flows. *EPL (Europhysics Letters)*, 64(2): 151, 2003.

[51] C. Beck. Statistics of three-dimensional lagrangian turbulence. *Physical review letters*, 98(6): 064502, 2007.

[52] L. Biferale, G. Boffetta, A. Celani, B. Devenish, A. Lanotte, and F. Toschi. Multifractal statistics of Lagrangian velocity and acceleration in turbulence. *Physical review letters*, 93(6):064502, 2004.

[53] L. F. Richardson. Atmospheric diffusion shown on a distance-neighbour graph. *Proceedings of the Royal Society of London. Series A, Containing Papers of a Mathematical and Physical Character*, 110(756):709–737, 1926.

[54] B. Sawford. Turbulent relative dispersion. *Annual review of fluid mechanics*, 33(1):289–317, 2001.

[55] G. Batchelor. The application of the similarity theory of turbulence to atmospheric diffusion. *Quarterly Journal of the Royal Meteorological Society*, 76(328):133–146, 1950.

[56] B. Sawford, P. Yeung, and J. Hackl. Reynolds number dependence of relative dispersion statistics in isotropic turbulence. *Physics of Fluids*, 20(6):065111–1 – 065111–13, 2008. ISSN 0031-9171.

[57] L. Biferale, G. Boffetta, A. Celani, B. Devenish, A. Lanotte, and F. Toschi. Lagrangian statistics of particle pairs in homogeneous isotropic turbulence. *Physics of Fluids (1994-present)*, 17(11): 115101, 2005.

[58] M. Chertkov, A. Pumir, and B. I. Shraiman. Lagrangian tetrad dynamics and the phenomenology of turbulence. *Physics of Fluids (1994-present)*, 11(8):2394–2410, 1999.

[59] J. F. Wendt. *Computational Fluid Dynamics*. Springer Berlin Heidelberg, 2009.

[60] J. N. Reddy. *An Introduction to Continuum Mechanics*. Cambridge University Press, 2008.

[61] S. A. Orszag and G. Patterson Jr. Numerical simulation of three-dimensional homogeneous isotropic turbulence. *Physical Review Letters*, 28(2):76, 1972.

[62] C. Canuto, M. Y. Hussaini, A. M. Quarteroni, A. Thomas Jr, et al. *Spectral methods in fluid dynamics*. Springer Science & Business Media, 2012.

[63] J. H. Williamson. Low-storage Runge-Kutta schemes. 35:48–56, 1980.

[64] J. H. Ferziger and M. Perich. *Computational Methods for Fluid Dynamics*. Springer, 1996.

[65] K. Alvelius. Random forcing of three-dimensional homogeneous turbulence. *Physics of Fluids*, 11(7):1880–1889, 1999.

[66] N. Li and S. Laizet. 2decomp&fft - a highly scalable 2D decomposition library and fft interface. In *Cray User Group 2010 Proceedings*, Edinburgh, 2010.

[67] M. Frigo and S. G. Johnson. The design and implementation of FFTW3. *Proceedings of the IEEE*, 93(2):216–231, 2005.

[68] H. Homann, J. Dreher, and R. Grauer. Impact of the floating-point precision and interpolation scheme on the results of DNS of turbulence by pseudo-spectral codes. *Computer Physics Communications*, 177(7):560 – 565, 2007.

[69] P. Yeung and S. Pope. An algorithm for tracking fluid particles in numerical simulations of homogeneous turbulence. *Journal of Computational Physics*, 79(2):373 – 416, 1988.

[70] J.-C. Chen, G.-D. Jin, and J. Zhang. Lagrangian statistics in isotropic turbulent flows with deterministic and stochastic forcing schemes. *Acta Mechanica Sinica*, 31(1):25–31, 2015.